TOWARDS PERFECT LIGHT COUPLING AND ABSORPTION IN NANOMEMBRANES

WITH OMNI-DIRECTIONAL ANTI-REFELCTION AND PHOTONIC CRYSTAL

STRUCTURES

by

ARVINDER SINGH CHADHA

Presented to the Faculty of the Graduate School of

The University of Texas at Arlington in Partial Fulfillment

of the Requirements

for the Degree of

DOCTOR OF PHILOSOPHY

THE UNIVERSITY OF TEXAS AT ARLINGTON

May 2014

Acknowledgements

I am incredibly fortunate to work with and have active discussions with talented people including professors, post doctorates and colleagues during my time at University of Texas at Arlington. First and foremost, I would like to thank my advisor Professor Weidong Zhou. His knowledge, scientific curiosity and creativity have being my source of inspiration along my journey towards finishing my dissertation. I not only appreciate his efforts giving me the chance to work on cutting edge research but also the opportunity to present my research at pioneering scientific conferences across the nation. I cannot thank him enough for his patience and generous time guiding me through my research.

I would also like to thank Professor Robert Magnusson, Professor Michael Vasilyev, and Professor Donald Butler. I have learned a great deal of nanophotonics, optics, semiconductor device physics and modeling under their tutelage. Active discussions with them have been my source of knowledge, thorough understanding and vision on efficient scientific problem solving. I also appreciate Dr. Yuze Sun for being in my committee. I gratefully acknowledge our collaborators as well. Professor Zhenqiang Ma at University of Wisconsin – Madison on research related to silicon nanomembrane transfer. Professor Adrienne Stiff-Roberts and her student Ryan McCormick at Duke University on research related to anti-reflection coatings. I would also like to thank Dr. Eric Cline for providing uv- curable resin for large area imprinted surface textures for omnidirectional conformal antireflection coatings on flexible amorphous silicon solar cells. Professor Julia Hsu and her student Jian Wang at the University of Texas at Dallas on research related to plasmonic solar cell.

I would like to express my special thanks to Dr. Deyin Zhao and Dr. Jae Woong Yoon for active technical discussions. I also acknowledge Dr. Kyu Lee for training me on ellipsometer. I would like to thank my lab mates (Dr. Hongjun Yang, Laxmy Memon and

I would like to thank my family for having a strong heart and faith in me to pursue my higher education at University of Texas at Arlington. I would have not made it so far without your support and blessings. Lastly, I would like to thank all my friends who made my time here at the university extremely fun and memorable, from doing homework at late nights, seeking free food on campus to participating in festivities and barbeques.

I could have not done my dissertation without each and all of you.

April 15, 2014

Abstract

TOWARDS PERFECT LIGHT COUPLING AND ABSORPTION IN NANOMEMBRANES

WITH OMNI-DIRECTIONAL ANTI-REFELCTION AND PHOTONIC CRYSTAL

STRUCTURES

Arvinder Singh Chadha, PhD

The University of Texas at Arlington, 2014

Supervising Professor: WEIDONG ZHOU

Silicon photonics is realized as a promising platform to meet the requirements of higher bandwidth and low cost high density monolithic integration. More recent demonstrations of a variety of stretchable, foldable and transfer printed ultra-thin silicon integrated circuits have instigated the use of flexible silicon nanomembrane for practical applications. Equally impressive innovations are demonstrated in the area of flat screen displays, smart cards, eyeglasses, and wearable displays. However, the overall efficiency of a variety of optical device is limited by poor light management resulting from difficulty of light coupling, small absorption volume in thin-film nanomembrane, and glare at oblique incidence to name a few. The aim of this thesis is to present the work of micro- and nano-scale structures for out-of-plane light coupling and absorption for integrated silicon photonics and high performance solar cells and photodetectors, with maximum absorption in the functional layer and minimal front-surface reflection and minimal rear-surface transmission.

Perfect absorption in a variety of semiconductor nanomembranes (NM) and atomic layers of two dimensional (2D) materials over different wavelength spectrum is realized due to local field intensity enhancement at critical coupling to the guided

resonances of a photonic crystal (PC). A judicious choice of grating parameters tailors the power diffracted in the zeroth order and higher order modes making the device work as a broadband reflector, an in-plane coupler or a combination of both reflector and an in-plane coupler. At surface normal incidence, the polarization dependence of the grating based reflector is eliminated by the use of 2D photonic crystals. The incorporation of such a reflector after the functional nanomembrane layer reduces the back-surface transmission. Effect of incident angle, polarization and incident plane misalignment dependence on the reflection of a silicon NM based reflector are investigated in detail. The front-surface Fresnel reflection is reduced with the incorporation of an omni-directional anti-reflection coating (Omni-ARC) based on nanostructures or by deposition of graded refractive index (GRIN) films. A design methodology based on the comparison of the rate of change of the refractive index profile of nanostructures of different shapes and thickness as an equivalent GRIN film suggests the minimum feature size needed to give near perfect ARC. Numerical models were built to account for the non – uniform GRIN film deposition on both rigid and flexible, flat and curved surfaces resulting from the variation in the resonant infrared matrix-assisted pulsed laser evaporation (RIR-MAPLE) process technology.

With the miniaturization of the devices, the effect of finite beam size and finite active area of the photonic components on the optical properties like transmission, reflection and scattering loss was studied as well. All the numerical studies presented in the thesis are validated by experimental results.

Table of Contents

List of Illustrations

List of Tables

Chapter 1

Introduction

1.1 Motivation

While silicon has ruled monolithic integrated electronics, a variety of other materials are being explored to expand the wavelength range of operation with better performance. Attention of the scientific community is geared towards nanomaterials [1-5]. Nanomaterials are a material in which at least one of the dimensions is of the order of nanometers. This results in confinement of the carriers and modified density of states within the material resulting in both electrical and optical properties quite different from their characteristic bulk. High mobility, optical transparency, low power consumption, relatively higher operating temperatures and mechanical flexibility make them attractive for a variety of optoelectronic devices like photodetectors, solar cells,   light emitting diodes, touch screen, optical limiters, frequency converters, terahertz devices, saturable absorbers and lasers [6-15]. However to the reduced absorption volume from the nanomaterials leads to much lower absorption [16]. Thus, for a high efficiency practical device there lays a need for a near perfect absorption from these nanomaterials to explore their true potentials in the area of photonics and optoelectronics.

To meet the needs for the ever growing data rates, the traditional copper interconnect will be replaced by optics all the way to chip-to-chip interconnect.[17] CMOS compatible, silicon photonics on a rigid silicon-on-insulator substrate is investigated extensively to achieve light generation, modulation, transmission, amplification and detection all from one chip package [18]. Heterogeneous integration is also realized as a promising approach to build high performance photonic devices [19, 20]. However, coupling light from an external fibre to an integrated photonic chip is a daunting task.

1

Another motivation is thin film electronics and more recently, nanomembranes for integrated and flexible silicon photonics. Remarkable progress has been made in the field of thin film electronics starting from thin film silicon solar cells in 1960s to the mode sophisticated large area thin film displays [21-25]. More recent demonstrations of a variety of stretchable, foldable and transfer printed ultra-thin silicon integrated circuits have instigated the use of flexible silicon nanomembrane for practical applications [26-30].

In both the thin film flexible photonic and the rigid bulk photonic systems, the efficiency of an optoelectronic module is dependent on the absorptance in the absorber layer. Following the energy conservation law we can write,

$$R_{front}(\lambda) + \sum_{m=1}^{n} A_m(\lambda) + T_{back}(\lambda) = 1 \qquad (1.1)$$

where $R_{front}(\lambda)$ is the front-surface reflection, measured at the first interface of the device, $A_m(\lambda)$ is the $m{-}th$ layer absorptance constituting the device, and $T_{back}(\lambda)$ is the transmitted light at the rear-surface transmission, measured at the last interface of the device. A judicious light management in any front side, rear side, and/or intermediate layers will influence the absorptance in the absorber layer. In what follows are schemes to demonstrated enhanced absorption from atomic monolayers to nanomembranes, surface normal vertical to in-plane coupling, near perfect anti-reflection coatings and high performance membrane reflectors with the incorporation of the micro- and nano-scale structures for out-of-plane light coupling and absorption for high performance solar cells and photodetectors, with maximum absorption in the functional layer and minimal front-surface reflection and minimal rear-surface transmission. Numerical studies presented in the dissertation are validated by experimental results.

1.2 Overview of Dissertation

Chapter 2 discusses the principle of Fano resonance and local field enhancement from the two dimensional photonic crystals. Rigorous coupled-wave analysis (RCWA) theory is utilized to design a Fano filter. Absorption enhancement in an ultra-thin InGaAs nanomembrane is demonstrated. Consequently, a spectrally-selective absorption enhanced stacked InGaAs/Si photonic crystal infrared photodetector is demonstrated.

Chapter 3 is centered on the analysis, design, fabrication and testing of higher order grating coupler for high efficiency surface normal vertical to in-plane coupling for optical interconnect applications. A fabrication tolerant high efficiency broadband fourth order grating coupler is designed using finite-difference time-domain technique.

Chapter 4 begins by discussing the background of anti-reflection (AR) coatings. Trade-offs between the bottom-up and up-down anti-reflection coatings are presented. Large area imprinted inverted pyramid textures are demonstrated on commercially available a-Si solar cells with increased cell efficiency. Optical designs for the graded index anti-reflection coatings (GRIN ARC) are presented. We then propose a design methodology to relate nanostructures as an effective GRIN film to design a near perfect anti-reflection coating. Optical designs for the omni-directional ARC on rigid and flexible surfaces accounting for the process variation from commercially viable resonant infrared matrix-assisted pulsed laser evaporation (RIR-MAPLE) technology are investigated. Both the ARC based on nanostructures and RIR-MAPLE technology are designed to allow near perfect transmission for a broadband spectrum over a wide range of incident angles (120^0 cone angle).

Chapter 5 presents an angular and the polarization properties of a two dimensional silicon photonic crystal membrane reflector. Detailed analysis of Fano resonant mode dispersion properties is presented to further aid the understanding of the mode splitting at oblique incidences. Simulated and measured results are in good agreement.

Chapter 6 investigates a novel grating design that can serve dual purpose of high efficiency reflector and in-plane coupler. Different design configurations are analyzed and the respective reflection and in-plane coupling efficiencies are compared. Preliminary experimental results are also presented in this section.

Chapter 7 summarizers the work presented in the dissertation. Suggestions for future work on perfect absorption from atomic monolayers and higher order gratings for dual direction emission from vertical cavity surface emitting lasers (VCSEL).

Chapter 2

Enhanced Absorption

2.1 Background

Dating back to the 1980s, photonic crystals were realized as a promise for meeting the photonics industry needs. Photonic crystals (PCs) are periodic arrangement of materials with different dielectric constants. Such a configuration alters the light matter interaction allowing strong photon localization and inhibition of spontaneous light emission [31, 32]. The ease of fabrication and device integration allows the use of two-dimensional photonic crystal slabs (2D - PCs) for practical device applications. The unconventional dispersion properties make photonic crystals allows them to realize a variety of optical devices like wavelength selective compact filters [33]. Spectrally selective Infrared photodetectors finds its various applications in military target detection/identification, foliage and camouflage detection, multi-spectral classification of dissimilar materials, IR gas sensing and absorption spectroscopy. The photonic structure alters the photonic density of states (DOS) thereby altering the absorption property of the medium. Enhanced absorption through local electromagnetic field location is investigated in defect cavity, metallic surface plasmon-polarization and dielectric photonic crystals.[34, 35] Most of the work so far has been focused on the absorption change in one-dimensional distributed Bragg reflector (1D DBR) based cavities, metallic photonic crystal cavities or epitaxial quantum dot system [34, 36-39]. Not much work in absorption enhancement from all dielectric photonic crystal is reported in literature.

We report spectrally-enhanced metal-semiconductor-metal photodetectors (MSM-PD's) with interdigitated Au Schottky contacts have been fabricated on stacked ultra-thin InGaAs/Si Fano resonance membranes. The study will lead to a new class of photodetectors with desired angular-, spectral-, and polarization dependent properties

and such devices can be widely used in optical communications, hyper-spectral imaging systems and flexible photonics.

.

<div align="center">2.2 Fano Resonance in Photonic Crystal Structure</div>

A photonic crystal (PCs) with periodic modulation of the refractive index provides phase matching for the out of plane continuum radiation modes coupling with the discrete in plane modes, which is not possible with a bulk material. This coupling of the out of the plane radiation mode to the in plane discrete mode is a resonant phenomenon called Fano resonance [40, 41]. Therefore, Fano resonances provide an efficient way to channel light from within the slab to the external environment, and vice versa. A Fano resonance is accompanied by a rapid variation in phase which results in a change of transmission intensity from 0% to 100%. The resonance frequency and line width can be tuned by adjusting the geometric parameters of the photonic crystal. At resonant coupling there is strong localization of the fields and hence the energy inside or on the surface of a layer is of great interest for applications like bio sensing, light sources, frequency converters, optical traps, detectors, etc.

<div align="center">2.3 Fano Resonance Enhanced Spectrally Selective Metal Semiconductor Metal Infrared Photodetector</div>

The Fano filter is designed was designed using Rigorous coupled-wave analysis (RCWA) -numerical computational method [42, 43].

2.3.1 Device Fabrication

(a) SOI (b) Pattern release (c) Pattern transfer on glass

(E) InGaAs NM transferred on filter on glass with wax dissolution

(D) InGaAs NM with wax transferred on filter on glass

(A) InGaAs on InP (B) Front wax on InGaAs NM (C) InP substrate etching

(F) Metal deposition and lift-off
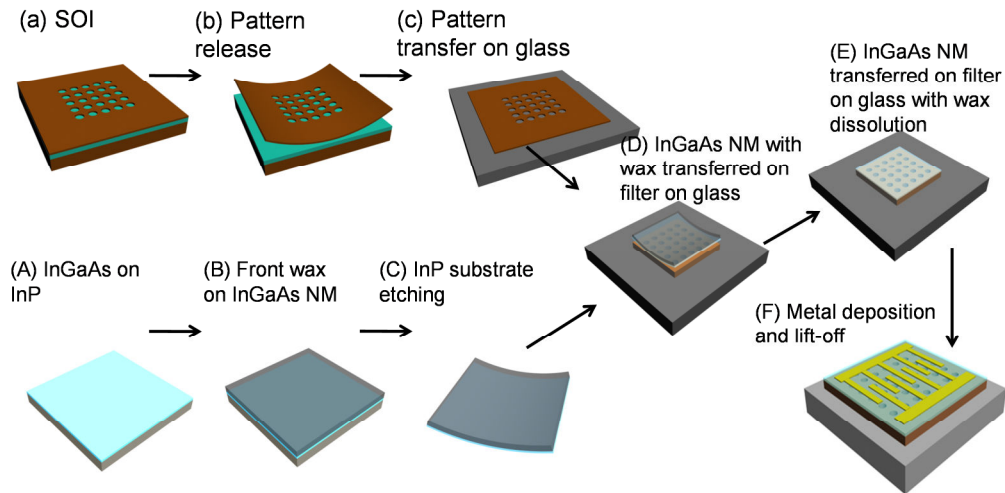
Figure 2-1: Schematic of the Fano Resonance enhanced photonic crystal Infrared Photodetectors based on transfer-printed InGaAs/Si nanomembranes

Figure 2-1 shows the schematic of the stacked ultra-thin InGaAs nanomembrane on silicon Fano filter transferred on glass substrate. The Fano filter is first fabricated on the silicon -on- insulator (SOI) wafer using a standard ZEP520A e-beam lithography technique. The silicon device layer is 340nm thick with a 2 µm thick buried oxide layer on silicon substrate. After the pattering of the resist, an HBr/Cl$_2$ chemistry based reactive-ion etching (RIE) process is used to etch holes in the device layer of the SOI wafer. In order to transfer the pattern of the device layer, the patterned SOI wafer is immersed in diluted HF (49% HF:DI water :: 1:4) for a few hours when the buried oxide layer is completely etched away. The patterned area is then picked and placed on the glass substrate by PDMS stamp. The bond strength of the patterned device silicon layer to glass substrate is greater than the patterned device silicon layer to PDMS stamp resulting in the transfer of the Fano filter on the glass substrate. The 750nm thick InGaAs NM is released from an InP substrate. Wax was used to protect the front side InGaAs from H$_3$PO$_4$/HCl (1/1) solution. After etching the InP substrate the InGaAs NM was transferred onto the

transferred Fano filter on glass. Finally, TCE was used to dissolve the wax and we get the desired device. The transferred InGaAs NM was thinned down to 100 nm using BCl_3/Cl_2 plasma reactive-ion etching for optimal absorption enhancement [44]. The metal contacts were made by standard metal deposition and lift-off technique. Shown in Figure 2-2(a) and (b) are the schematic of the Fano Resonance enhanced Infrared Photodetector and the cross section view of the device showing the Fano filter lattice constant (a), air hole radius (r) and the thicknesses of silicon nanomembrane SiNM (t), InGaAs NM (h) and gold electrodes (g). With the target Fano resonance wavelength of 1550 nm, the thickness of the SiNM Fano filter (h) was 340 nm. The square lattice air-hole PC structure has a period (a) of 900 nm, and the air hole radius (r) of 280 nm. 750 nm thick InGaAs nanomembrane (NM) was then transfer-printed on top of the transferred Si Fano filter on glass. Shown in Figure 2-2(c) is a top view scanning electron micrograph (SEM) of 100nm thick InGaAs NM on top of Si Fano filters on glass substrate. The Schottky metal contacts were made by thermal evaporation of 10 nm Au. The active area of the photodetector is 100 x 100 μm^2. The anode and cathode are formed by interdigitated finger contacts with spacing of 6 μm, as shown in Figure 2-2(d).
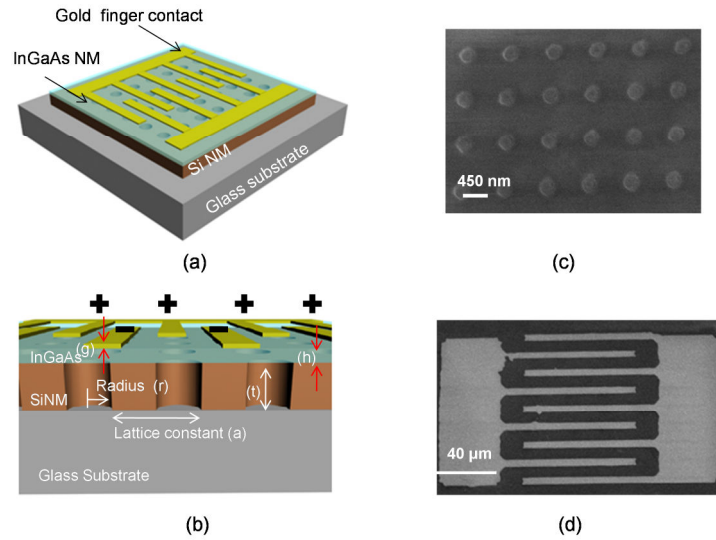
Figure 2-2 : Schematic of (a) SiNM Fano photodetector and; (b) cross section schematic of Fano PD showing air hole radius (r), lattice constant (a), thickness (t) of SiNM, and thickness (h) of InGaAs layer. (c) Top view scanning electron micrograph of the 100 nm thin InGaAs NM on Si resonant filter and; (d) the 10nm thick interdigitated Au finger contact on InGaAs NM.

2.3.2 Optical Characterization

A broadband white light source is generated from a quartz tungsten halogen lamp that is collimated by a collimator. A 50/50 beam splitter is used for transmission and reflection measurement. The transmission and reflection measurements were done on InGaAs nano membrane on and off the SiNM Fano resonance filter, without metal electrodes. Shown in Figure 2-3(a) is the measured percentage absorption in the 100 nm InGaAs NM on and off the SiNM Fano resonance filter. In all the cases, the absolute absorption is calculated by subtracting the transmission and reflection spectrum from unity.

9
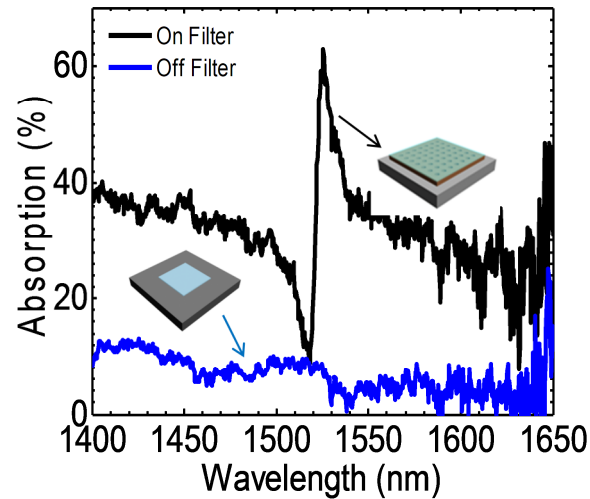
Figure 2-3: Measured absolute absorption in percentage in the 100nm thin InGaAs MSM PD on and off the SiNM Fano resonance filter. The inset shows the schematic of the InGaAs nanomembrane on and off the filter.

2.3.3 Field Distribution

When the light couples into the discrete modes of the photonic crystal, the resonant field decays away from the interface of the filter and strong field region penetrates in the InGaAs NM. Thus there is an increased light matter interaction. The resonant coupling of the Fano filter increases the 100 nm InGaAs NM absorption from 7% to 64% (Figure 2-3). This is primarily from the overlapping of the spatial mode of the Fano filter onto the 100nm thick InGaAs NM. The amount of the absorption enhancement depends on the filter's modal property. In Figure 2-4, we show the electric field profile obtained at Fano resonance wavelength by a finite-difference time domain (FDTD) method. This increased light matter interaction increases the photo generated carriers for the same amount of incident power and hence would increase the responsivity of the photoconductive devices.
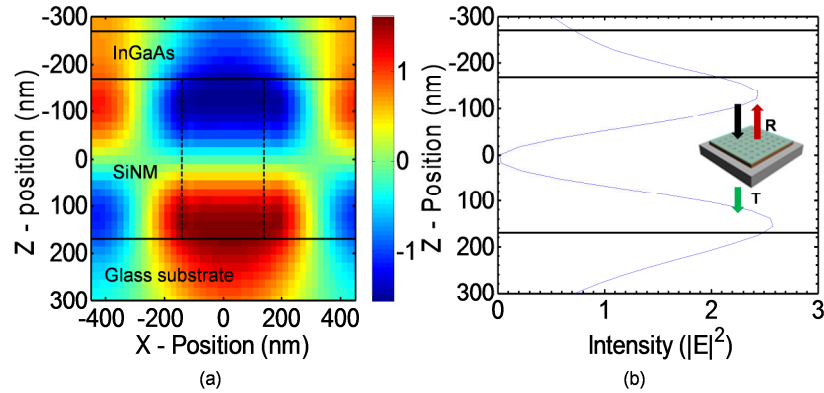
Figure 2-4: (a) A cross-sectional view of the FDTD calculation of the electric field in the vicinity of the Fano resonance membrane at resonance. (b) The intensity distribution through the center of the unit cell. The inset shows the orientation of the Fano resonance enhanced MSM PD.

2.3.4 Electrical Characterization
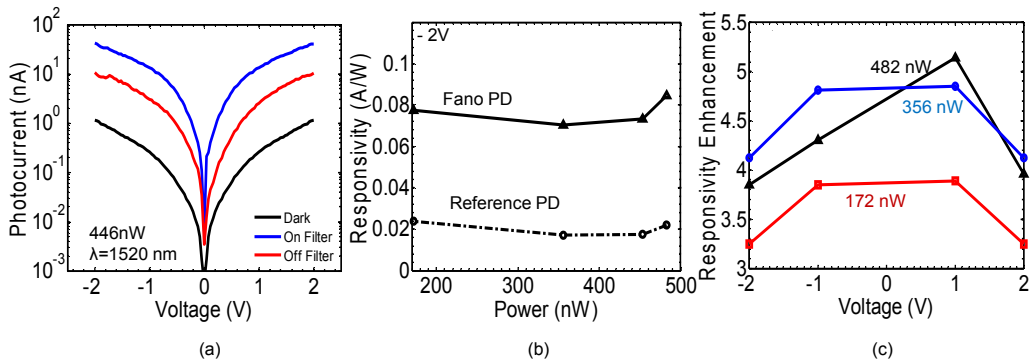
Figure 2-5: (a) Measured photocurrent in the 100nm thin InGaAs MSM PD on and off the SiNM Fano resonance filter. (b) Measured responsivity of the InGaAs Fano Photodetector (solid) and reference PD (dash) at -2V. (c) The measured responsivity enhancement at 1523 nm for various power levels.

An optical band pass filter with center wavelength 1,520 nm with FWHM of 10 nm was used for the photocurrent characteristics. Photodetector performance was characterized after the incorporation of finger contacts. Shown in Figure 2-5(a) is the measured photocurrent at the resonant nanomembrane wavelength. All the

11

measurements were performed for normal incidence of light. An optical attenuator was used to measure the photocurrents at various incident power levels. Shown in Figure 2-5 is also the responsivity and responsivity enhancement of the InGaAs MSM PD on and off the Si Fano resonance membrane. The responsivity enhancement is defined as the ratio of the responsivity of the MSM PD on the Si Fano resonance membrane to the responsivity of the MSM PD off the Si Fano resonance membrane. The leaky modes from the Si Fano resonance membrane significantly increases the amount of time light spend within the detector active region, and therefore enhances the probability of detection. The devices exhibit a dark current of 1.15 nA at -2 V. The responsivity measured at 1,523 nm wavelength is enhanced from 0.022 A/W to 0.084 A/W. A responsivity enhancement of 3.8 over the conventional MSM-PD's without the presence of Si Fano resonance membrane is also demonstrated. It is also worth noting that the quality factors of Fano resonance in our experiments were far from optimal.

According to earlier theoretical work, it is possible to design an extremely high Q filter. [40, 45] With optimized quality factors it is possible to achieve one or two orders of absorption enhancements. The bandwidth of the MSM detectors is limited by the transit time which can be overcome by reducing the finger spacing. Although we demonstrate the detector at the IR region, the spectral resolution and tunability can be accomplished by controlling the cavity Q and resonant peak location by changing the r/a ratio of the photonic crystal. The Fano resonant membranes can potentially be transferred on a range of foreign substrates including plastics thereby attracting potentials for flexible nano photonics for spectral imaging and detectors applications.

2.4 Perfect Absorption via Critical Coupling

Atomic monolayers of two dimensional materials like graphene and molybdenum disulphide are extensively studied due to their unique optical and electronic properties.[46, 47] Atomically thin layers are almost transparent with little absorption. Practical optoelectronic devices with high efficiencies from these monolayers demands near perfect absorption [48]. While absorption can be increased by placing the absorbing layer in a resonant cavity, however, fabrication of the top mirror forming the cavity is quite challenging [49, 50]. Metallic surface plasmon-polariton (SPP) tend to increase the absorption due to local field enhancement near the metal dielectric interface, but it involves the use of lossy metal and often requires polarization dependent coupling schemes [51-53]. On the other hand, dielectric photonic crystals are lossless and provide dispersion properties that facilitate enhanced photonic density of states and penetration of Bloch waves throughout the structure. Fano resonance principle provides the local field enhancement in a defect-free photonic crystal. We investigate the perfect absorption in atomic monolayers by critical coupling to Fano resonance of nanomembrane photonic crystal structures to achieve perfect absorption [54, 55].

2.4.1 Theory of Critical Coupling and Perfect Absorption

A proper choice of geometric parameters of the photonic crystal allows the coupling of the incident light into the in – plane guided modes of the photonic crystal (PhC) slab [40, 56]. These guided modes have a finite lifetime and eventually leak out of the photonic crystal. The rate at which these mode leak out can be explained in details by the coupled mode theory [57, 58]. An atomic monolayer is featured by almost zero absorption and near unity transmission. Thus their incorporation on the photonic crystal slab does not perturb the field distribution at resonance or elsewise. Only the amount of

field enhancement is altered. The external leakage rate of the photonic crystal is tuned by changing the ratio of the radius to the lattice period or the thickness of PhC slab. The external leakage rate is determined from the half max at half width of the resonance for the slabs in the absence of the graphene monolayer. Likewise the half max at half width of the resonance for the slabs in the presence of the graphene monolayer give the sum of the external leakage rate and the intrinsic absorption rate within the graphene monolayer. A system is said to be critically coupled when the leakage rate of the optical mode out of the photonic crystal is equal to the absorption rate of the mode in the active absorbing layer. At critical coupling all the energy is transferred into the absorbing layer and perfect absorption is possible. In what follows is an example of near perfect absorption from atomic monolayers of graphene and molybdenum disulphide at infra-red and visible wavelengths.

Figure 2-6 demonstrates the concept of perfect absorption from graphene monolayer at 1550 nm at surface normal incidence. Graphene monolayer is modeled as cited in reference [59]. The two dimensional photonic crystal is realized from a periodic arrangement of circular holes in a square lattice. The lattice period (Λ) and radius (r) of the holes are 900 nm and 189 nm (= 0.21Λ) respectively. The thickness of the slab is 90 nm. A monolayer of graphene has only 2.3% with the remainder of the light being transmitted [60]. Whereas placing the same monolayer on top of a photonic crystal backed by a mirror (Figure 2-6 (a)) increases its absorption to almost 98% as shown in Figure 2-6 (b). 5 Bragg pairs are assumed in the simulation to ensure zero transmission as any non-zero transmission correspond to energy loss out of the system and cannot be absorbed thus, limiting perfect absorption. Since the absorption from graphene is relatively wavelength independent, multiple wavelengths are critically coupled simultaneously.
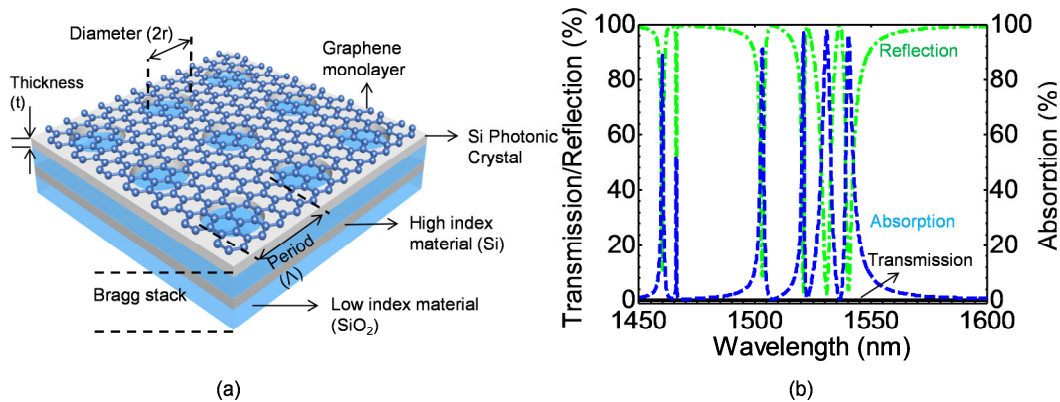
Figure 2-6: (a) Schematic of absorption enhancement from a monolayer of graphene. A photonic crystal with lattice period (Λ), radius (r) and thickness (t) is back by a Bragg stack (1.5 pair as shown) of silicon dioxide and silicon. (b) Simulated transmission reflection and absorption from the corresponding absorption enhancement scheme.

This allows the use of this configuration particularly attractive for telecommunication applications. Keeping the ratio of the radius to the lattice period fixed, the resonance frequency can be tuned by altering the lattice period or the thickness of the PhC slab.

While we have focused our discussion on telecommunication wavelength near 1550 nm. The critical coupling concept is equally applicable to visible wavelength or any wavelength range for that matter and any other two dimensional material. Figure 2-7 gives an example of total absorption at a visible wavelength of 680 nm from molybdenum disulphide material at surface normal incidence. The molybdenum disulphide thickness is taken as 0.7nm and the refractive index is modeled as cited in reference [61]. Silicon nitride and silicon dioxide are chosen as the materials for the Bragg stack. In the visible wavelength, silicon is highly absorbing therefore; we used silicon nitride as a choice of the dielectric for the photonic crystal. The refractive index of silicon nitride is modeled as cited in reference [62]. In theory, any other lossless dielectric with high refractive index could be used as a photonic crystal (eg. tantalum pentoxide (Ta_2O_5 with refractive index

of 2.12). With the lattice period (Λ) of 450 nm, radius (r) of 117 nm (= 0.26Λ) an absolute

absorption of 98% is easily attainable.

(a)

(b)
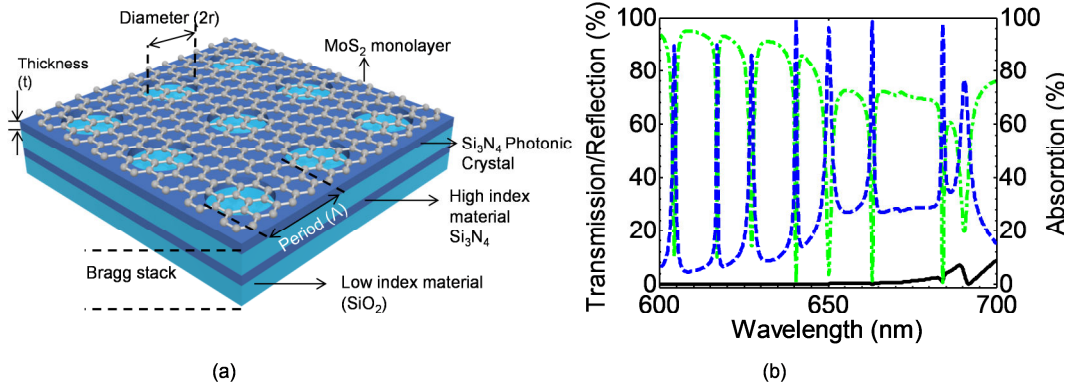
Figure 2-7: (a) Schematic of absorption enhancement from a monolayer of molybdenum disulphide at visible wavelength. A photonic crystal with lattice period (Λ), radius (r) and thickness (t) is back by a Bragg stack (1.5 pair as shown) of silicon dioxide and silicon nitride. (b) Simulated transmission reflection and absorption from the corresponding absorption enhancement scheme.

A simple cost effective mechanical exfoliation technique shows the potential of integrating the novel two dimensional materials [63, 64]. While we have focused our work on the numerically modeling the near perfect absorption at surface normal incidence, the impact of oblique incidence needs to be investigated. Additionally, by further optimization, it might be possible to design a relatively broad band near perfect absorber. Corresponding experimental demonstration will further support the feasibility of the critically coupled enhanced absorption scheme for communication, imaging and energy harvesting applications.

Chapter 3

Vertical to In-Plane Coupling

<u>3.1 Background</u>

Optical interconnects provide an attractive way to meet the increasing bandwidth and computation demands. However, coupling of the light to on-chip waveguides is a big challenge. Horizontal edge coupling of the single mode fiber to the on-chip waveguide is extremely poor due to the mode mismatch or it requires difficult and accurate alignment. [65, 66] Vertical to in-plane couplers (VICs) can couple light through any point on the planar on chip and can be positioned anywhere across the wafer relaxing the need for the coupling along the edges. Several vertical to in-plane couplers have been demonstrated to couple light out of or into the waveguide. As reported in the literature, most the couplers use the fiber at near normal incidence to couple the light into the waveguide. [67-72] Slanted grating and chirped grating couplers have been demonstrated to couple light using normal incidence. [73, 74] However, the angled fiber is not desirable for low cost packing and is mechanically unstable. The slated grating uses non-standard fabrication methods.

More recently, a novel design of a surface normal second order grating coupler with high coupling efficiency is proposed, based on high contrast gratings (HCGs). [75] However, no experimental results are reported. We present a design of a robust broadband high efficiency vertical to in-plane optical coupler using fourth order gratings. The coupler is designed for TE mode with coupling efficiency of 88.5% at 1,535 nm with a 3 dB bandwidth of 42 nm. The fabrication tolerance of both the second order and fourth order grating couplers with surface normal coupling is also assessed.

.

3.2 Grating Theory

A short overview of the gratings and grating based directional couplers are presented in this section. Only dielectric gratings are considered. Gratings are one dimensional period structure where the refractive index is modulated by a high index and low index refractive material. Shown is a Figure 3-1(a) is a schematic of the grating placed on an infinite substrate with light incident from air. When the structures have a period on the order of the wavelength of incident light, the grating diffracts lights. The diffracted light travels in different directions. In addition to the incident light wavelength, the period (Λ), width (w) and the thickness (t_g) of the grating determines the direction of the diffracted waves. The exact angles at which the reflected and diffracted beams propagate are determined by the grating equation (3.1).
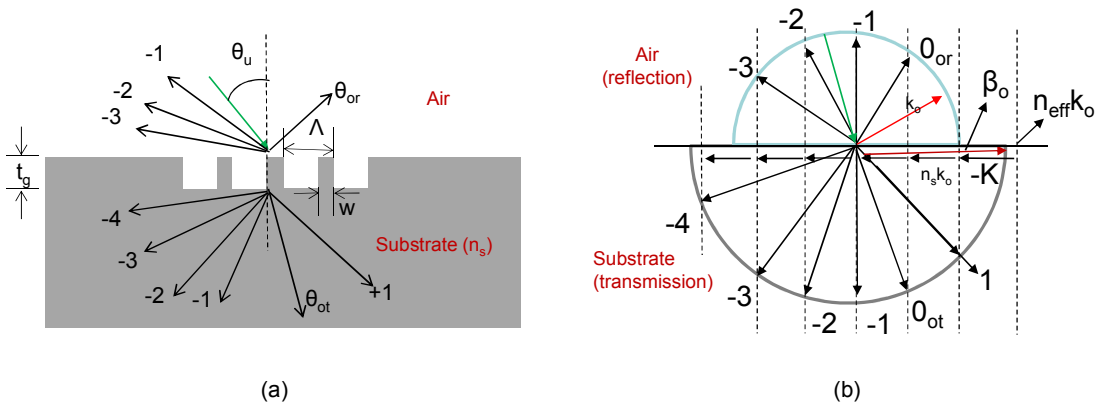
Figure 3-1: (a) Schematic of a grating with oblique incidence showing different diffracted order and relevant grating parameters. The grating period, thickness and width are denoted as Λ, t_g and w respectively. (b) Vector diagram of the corresponding grating. The direction of the arrow indicates the diffracted order waves.

$$n_{eff}\, sin(\theta_q) = \; n_i\, sin(\theta_u) - \frac{q\lambda_o}{\Lambda} \tag{3.1}$$

where, n_{eff} and n_i are the effective refractive index of the grating and the refractive index of the material to/from which the mode is coupled. θ_q and θ_u are the coupling angle of the qth diffracted order. The working principle of the diffraction grating is explained with the aid of the vector diagram as illustrated in Figure 3-1(b). The radii of the blue and gray circles are k_o (= $2\pi/\lambda$), and $n_{eff}\, k_o$ indicating the wave numbers in air and substrate respectively. Furthermore the Bragg condition tells us which diffraction orders exist. In the presence of the grating, guided modes propagates along the grating with the grating vector denoted by K (= $|2\pi|/\Lambda$). The *x* component of the wave vector of the harmonic wave by q^{th} order diffracted order is given by

$$\beta_q = \; k_o n_i\, sin(\theta_{q,i}) = \; \beta_o - qK \tag{3.2}$$

where *na is* air incident medium (= 1) and θ_q is the radiation angle. The script *i =* *(a)*, (*s)* denote superstrate (air) radiation and substrate radiation, respectively. For surface normal incidence, the maximum allowed diffraction order (q) for a grating with order (m) is q ≤ m/2. Consider the grating parameters based on the second order and the fourth order gratings. The second order grating parameters are based on partially etched and high contrast grating structures as reported references [76] and [75] respectively.

Table 3.1 summarizes the grating geometric parameters and corresponding diffraction efficiencies
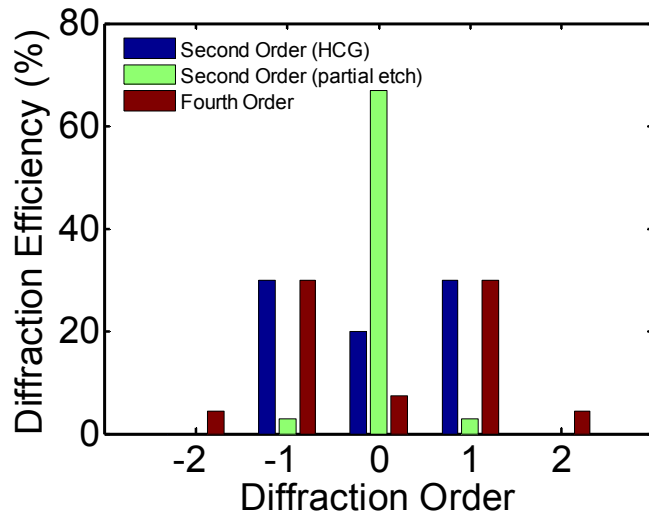
Figure 3-2 :Histogram of different diffracted orders from second order and fourth order gratings with surface normal illumination. The second order grating design parameters are partially etched and high contrast grating structures as reported references [76] and [75] respectively

Table 3.1: Diffraction efficiency of different diffracted order for second and fourth order gratings with surface normal ilumination. Second order grating parameters (*) and (**) are based on design parameters as stated in reference [76] and reference [75] respectively.

Grating Parameters	Grating Order		
	(*)Second Order	(**)Second Order	Fourth Order
Period (Λ)	630 nm	724 nm	1045 nm
Fill Factor (FF)	0.5	0.61	0.2
Grating thickness (t_g)	70 nm	960 nm	250 nm
Diffraction Efficiency			
q = -2	–	–	4.3%
q = -1	2.80%	30%	30%
q = 0	66.90%	19.7%	7.50%
q = 1	2.80%	30%	30%
q = 2	–	–	4.3%

The higher order diffracted modes (+2 and -2) do not exist for the second order grating as governed by the Bragg condition. The power distributed for all the orders is

20

symmetric due to surface normal illumination. A large amount of power (~ 67%) is observed in the 0th order for the second order grating based on the partial etched structure. For the same second order grating, by adjusting the grating geometric parameters, the power can be redistributed into the higher order modes. The power in the 0th order drops to 20% and as high as 30% is coupled in the +1 and -1 diffracted order. For a grating coupler, the power in the 0th order mode represents loss mechanism whereas the higher order mode results in the in-plane coupling. Usually, higher order diffraction grating has low higher order diffraction efficiency. However, a judicious choice of grating parameters allows a large grating period with improved higher order diffractive efficiency. As shown in Figure 3-2 when the grating order is changed to four, by increasing the grating period, power in the 0th order is further reduced to as low as 7.5%. This suggests that higher in – plane coupling is possible with an incorporation of a higher order grating.

3.3 Analysis of High Efficiency Surface Normal Vertical to In-Plane Couplers

Coupling light from an optical fibre into a photonic chip involves the use of an optical waveguide. Thus we consider an optical waveguide made from silicon from the silicon – on- insulator substrate. We investigate the use of the second order and fourth order grating to couple the surface normal incident light in to an in – plane waveguide. The light from the fibre is approximated by a Gaussian profile. The schematic of the surface normal vertical to in-plane couplers (VICs) are show in Figure 3-3. The 1D grating lies on top of the device silicon waveguide of the silicon-on-insulator substrate. The grating period (Λ), thickness (t_{gt}), waveguide thickness (t_{wg}), fill factor (FF) and the number of grating elements (N) control the coupling efficiency of the light. The proposed first order coupler consists of a subwavelength HCG grating located upon an in-plane waveguide with a certain low index gap. The fill factor is the ratio of the semiconductor

grating width to the period. The incoming light propagates in the z- direction. The coupled light propagates perpendicular to the incoming light in both the +x and –x direction as shown in the schematic.
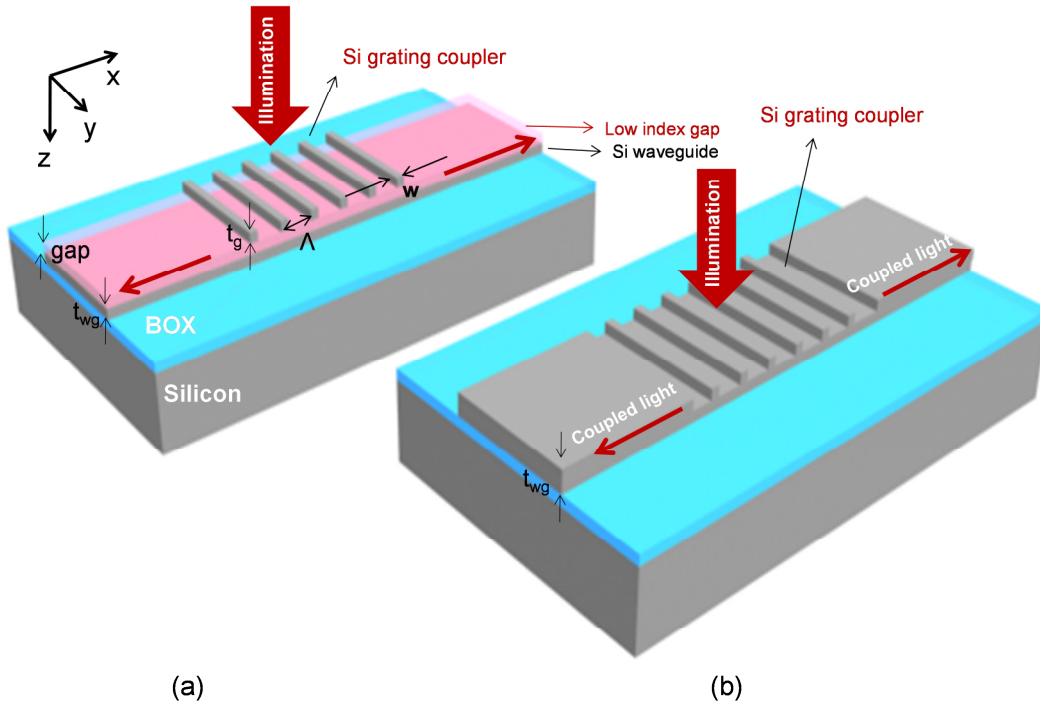
Figure 3-3: Schematic of the surface normal vertical to in-plane coupler (VIC) based on (a) high contrast grating and (b) partially etched gratings on silicon-on-insulator substrate, where Λ, w, t_g and gap are grating period, width, height and the separation between the grating and the waveguide respectively. The waveguide thickness is denoted by t_{wg}. Notice the absence of the low index gap in the partially etched surface normal VIC.

We begin the analysis by considering normal plane wave incidence. In order to obtain the electromagnetic response of the structure, finite-difference time-domain (FDTD) simulation was carried out. [77] Perfectly matched layers (PMLs) were incorporated at the boundaries of the computational domain to avoid unnecessary reflections of light at the boundaries. The simulations presented below are designed for a

22

TE mode surface normal vertical to in-plane coupler. The electric field is aligned along the gratings.

3.3.1High Contrast Surface Normal Vertical to In-plane Coupler
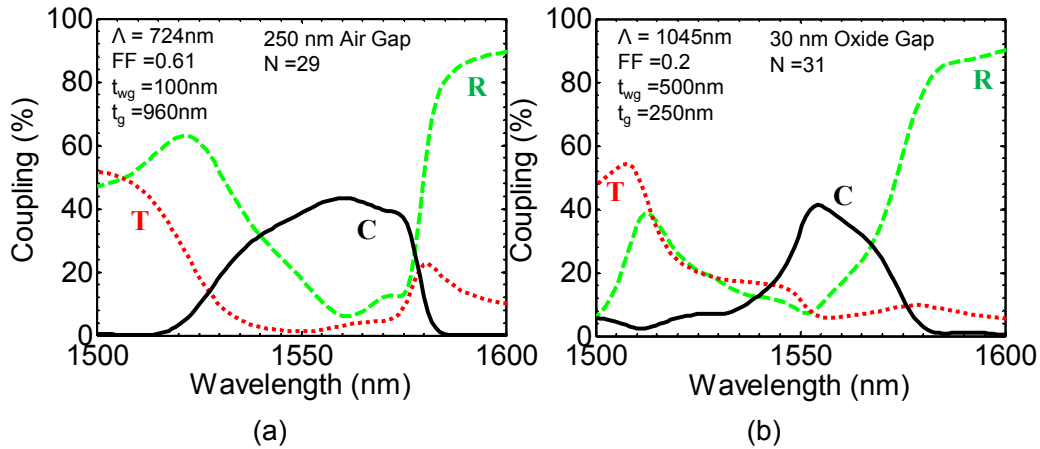
Figure 3-4: Simulated single side coupling efficiency (black), reflection (green) and transmission (red) from the (a) second order and (b) fourth order surface normal vertical to in-plane grating coupler.

Figure 3-3(a) shows the schematic of the surface normal vertical to in-plane grating coupler. The high index contrast is provided by the low index gap surrounding the grating as shown in the schematic. Such a high contrast grating supports two modes with index 1 and 2 [78]. When these modes reach either the input or exit interfaces of the grating, they are reflection back or coupled to each other. The resulting supermodes are characterized with a unique propagation constant. The finite thickness of the grating establishes a Fabry-Perot resonance condition. Tuning the thickness of the grating allows the tuning of the resonance wavelength. The reflector acts as a guided mode element. [56, 79] The in-plane guided modes are generated in the waveguide due the presence of the grating on top of the waveguide. The grating provides the desired phase matching to

couple the surface normal light to the second order in-plane waveguide mode. At this resonance condition, there is a large buildup of electromagnetic field. The grating coupler provides the phase matching between the input and output light. When the waveguide is brought close to the grating, there is non-zero overlap integral of the field within the waveguide and the grating. When the Fabry-Perot resonance and the grating phase matching have same wavelength, the field overlap enlarges and there is strong coupling between the high contrast grating and the propagating waveguide mode.

The second order grating coupler consists of a thin 100 nm silicon waveguide with 4 μm buried oxide layer. The grating height is 960 nm with period of 724 nm and fill factor of 0.61. An air gap of 250 nm is required between the HCG and the waveguide for surface normal coupling for the second order coupler. The fourth order grating coupler is designed with 260 nm silicon device layer with 2 μm buried oxide layer. The grating height is 260 nm with period of 1,045 nm and fill factor of 0.2. An oxide gap of 30 nm is present between the HCG and the silicon waveguide. Shown in Figure 3-4 are the simulated single side coupling efficiency, reflection and transmission from the second order and fourth order surface normal vertical to in-plane grating coupler based on HCG gratings. For maximum coupling occurs for when both the transmission to the substrate and the reflection back to the air is minimum. High contrast grating couplers based on the second order and the fourth order gratings both provide high in-plane coupling efficiency. The grating coupler based on second order grating, has 44% single side coupling efficiency with 3 dB bandwidth of 50 nm as compared to 41.3% single side coupling efficiency with 3 dB bandwidth of 26 nm.
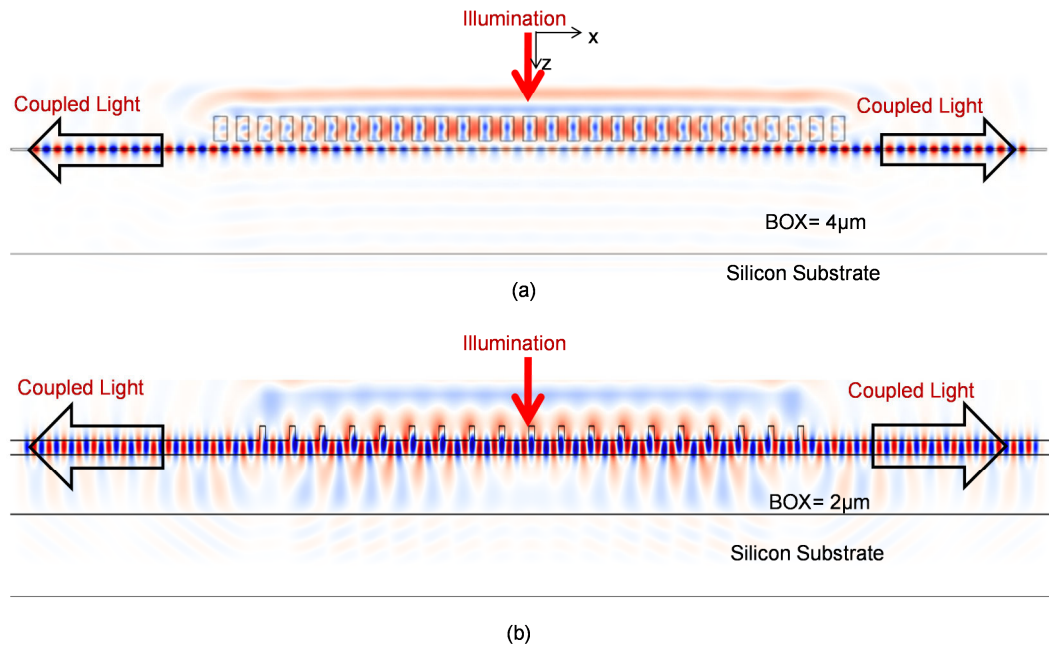
Figure 3-5: Field profile of the surface normal (a) first order vertical to in-plane coupler at 1,557 nm and (b) second order vertical to in-plane coupler at 1,552 nm.
.

Figure 2-5 shows the field plots for the high contrast grating couplers. For both the couplers, equal amount of light is coupled into both the –x and +x direction of the waveguide due to the symmetric nature of the light. The second order HCG coupler couples 44% light in each direction of the waveguide at resonance wavelength of 1,552 nm. The 3 dB bandwidth is 50 nm and 1 dB bandwidth is 34 nm for this second order grating coupler. Figure 3-5(a) clearly shows a considerable amount of light leaks out of the 100 nm waveguide and is confined strongly around it. Most of the light is confined within the waveguide for the fourth order HCG coupler. However, only 41.2% light couples in each direction of the waveguide at resonance wavelength at 1,557 nm. The 3 dB bandwidth is 26 nm and 1 dB bandwidth is 14 nm for the fourth order HCG coupler. In

both the couplers, the grating produces an upwards and a downwards propagating waves.

An obvious question arises: what is the effect of fabrication tolerance for these two types of HCG couplers based on second-order and fourth-order gratings? To answer this question we investigated the effect of the single side coupling efficiency by changing the design parameters like the number of grating, grating, period, grating height, grating fill factor, and the waveguide thickness. Only one design parameter was changed at a time while all the other parameters were kept constant. It is obvious from the grating equation that for a given period, the effective index decreases with larger wavelength while the ratio of wavelength to period increases, there is only one possible wavelength to match the phase of the grating and the waveguide. Hence, the change in grating period makes the 3 dB band shift without affecting the coupling efficiency for both the second order (Figure 3-6(a)) and fourth order (Figure 3-6(e)) HCG couplers. The reflection band shifts to the longer wavelengths due to the increase in the effective thickness of the waveguide with the increase in the thickness of the waveguide. This explains the red shift in the coupling efficiency with the increase in the waveguide thickness for the second order and fourth order HCG couplers as shown in Figure 3-6(b) and Figure 3-6(f) respectively. It is worth noticing a large spectral shift with a slight degradation in the efficiency of the coupling band for only 5 nm variation in the waveguide thickness of second-order grating VICs. Almost the same spectral shift with negligible degradation is observed in the second order grating coupler when the waveguide thickness changes by 10 nm. The fourth order coupler is more tolerant to the variation in the waveguide thickness. The grating height determines the perturbation to the propagating field [80] and can be characterized by an effective index. With the increase in the grating thickness, the effective index increases. This is analogous to a

26

ridge waveguide, where the single mode operation depends on the thickness of the waveguide.[81]
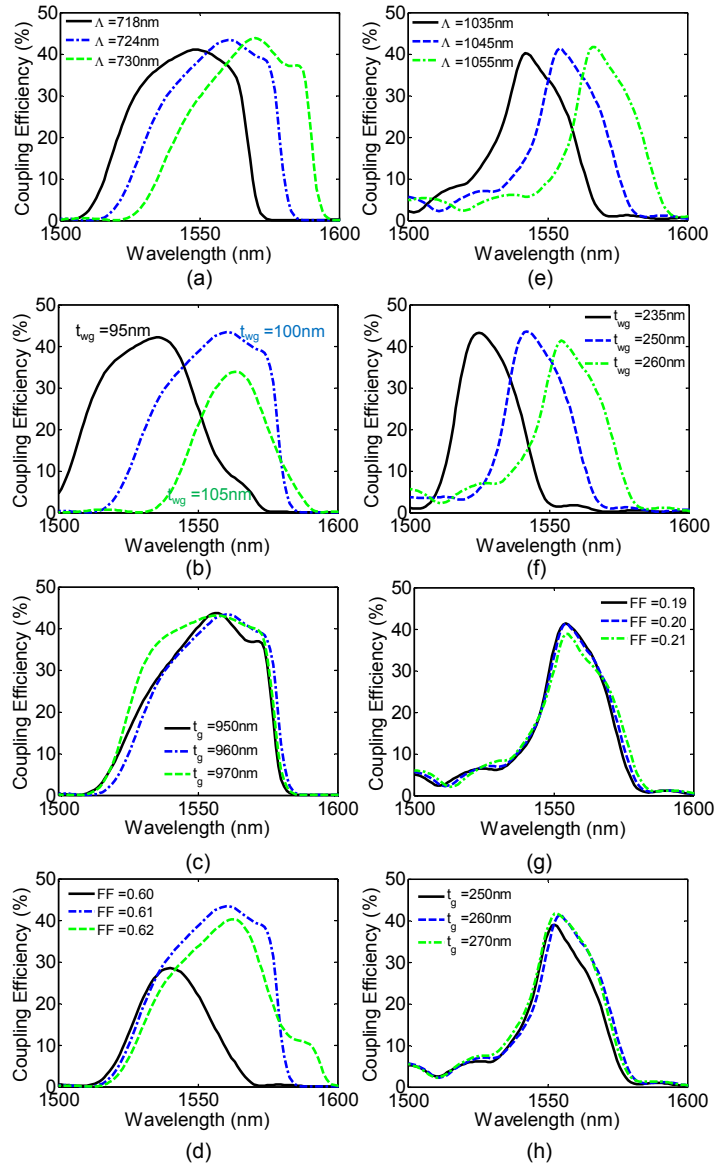
Figure 3-6: Numerically simulated single side coupling efficiency for (a – d) the second order and (e – f) the fourth order surface normal vertical to in-plane coupler. Left panel shows the variation in the coupling efficiency due to the changes in the grating period (Λ), waveguide thickness (t_{wg}), grating height (t_g) or fill factor (FF).

Also, as can be seen in Figure 3-6(c) and Figure 3-6 (g), a change in 10 nm in the grating thickness gives a slight shift in the coupling band. The fill factor affects the reflectivity of the grating seriously.[82] A 7 nm variation in grating width changes efficiency of the second order grating coupler significantly (Figure 3-6(d)) as compared to 10 nm variation in grating width resulting in negligible change in the coupling efficiency of the fourth order grating coupler (Figure 3-6(h)). In summary, the HCG coupler based on the second order and fourth order gratings both provide high coupling efficiency. While the 3 dB bandwidth of the second order HCG coupler is higher than the fourth order HCG coupler, the second HCG coupler is very prone to fabrication errors and demands very stringent fabrication technology.

So far we have considered coupling from air in to the waveguide. Using the same fourth order grating coupler it is possible to couple light from the waveguide to air as shown in Figure 3-7(a). When the light is illuminated from within the waveguide, the coupled light can leak out of the device to the air or can be lost to the substrate. The reflection and the transmission within the waveguide are also the means of loss. The electric field is along the length of the grating (i.e. TE mode illumination) within the waveguide. A peak efficiency of 90% is easily achievable with this configuration as shown in in Figure 3-7(b). The 1 dB coupling to air extends from 1408 nm to 1459 nm and 1467nm – 1498 nm.

The coupling to the substrate, a loss mechanism, can be further reduced by optimizing the thickness of the buried oxide or by an addition of a bottom Bragg reflector. The transmission through the waveguide can be reduced by either chirping the grating elements or by adding distributed Bragg reflector. The placement of an anti-reflection coating on top of the gratings will also increase the coupling to the air. Thus by optimization it is possible to achieve near perfect coupling from waveguide to air as well.

(a)   (b)
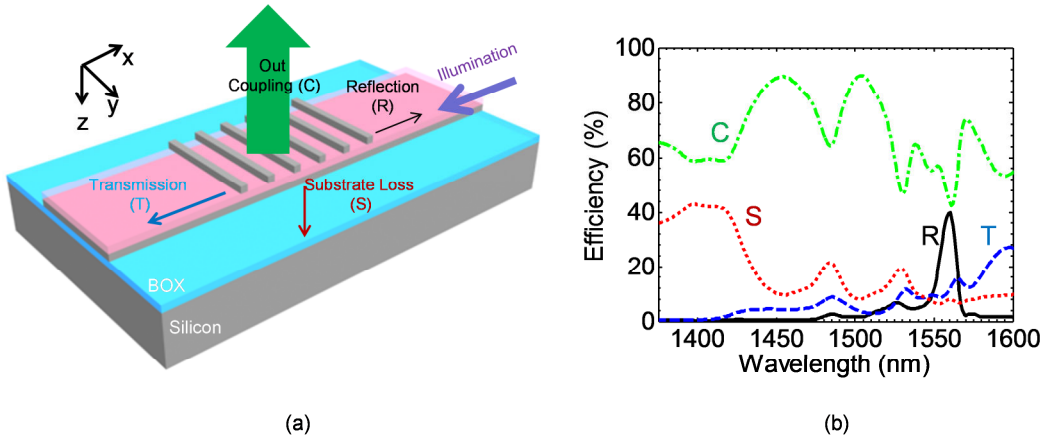
Figure 3-7: (a) Schematic of the waveguide to air grating coupler showing illumination direction, coupling to air and transmission (T) and reflection (R) within the waveguide and loss in the substrate (S). (b) Simulated coupling efficiency into the air,   the transmission and reflection loss within the waveguide and unwanted coupling to the substrate.

3.3.2 Partially Etched Surface Normal Vertical to In-plane Grating Coupler

The high contrast gratings involve the use of a low contrast material surrounding the grating. The use of the low contrast medium between the grating and the waveguide in the HCG based grating coupler adds additional fabrication complexity. In this section, we explore the performance of a grating coupler based on partially etched gratings as shown in in Figure 3-3 (b). The parameters for the second order gratings are based on design as reported in reference [76]. Shown in Figure 3-8 are the simulated single side coupling efficiency, reflection and transmission from the second order and fourth order surface normal vertical to in-plane grating coupler based on partially etched gratings.

29
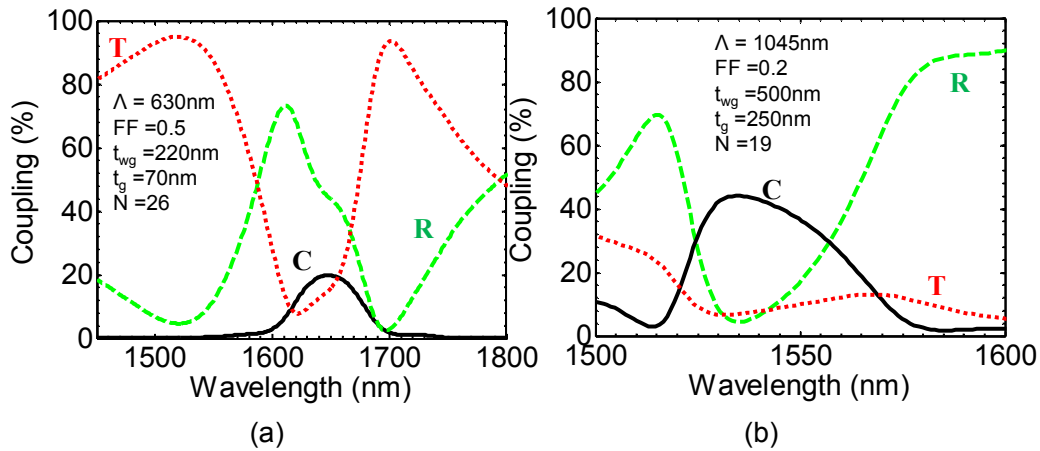
Figure 3-8: Simulated single side coupling efficiency (black), reflection (green) and transmission (red) from the (a) second order and (b) fourth order surface normal vertical to in-plane grating coupler.

.

Based on the discussion from section 3.2 as expected the high transmission from the 0th order diffracted mode from the second order grating limits the in-plane coupling to around 25%. The dimensions of the fourth order partially etched grating coupler are such that both the first and second order diffracted waves are coupled into the waveguide. The first diffracted order guided within the silicon waveguide due to total internal reflection at the oxide-silicon interface and the silicon-air interface. The second diffracted order couples to in-plane waveguide due to k-vector matching. At surface normal incidence, some leakage to the substrate is present which limits the in-plane coupling efficiency of the fourth order grating coupler to near perfect. Numerically 44% single side in-plane coupling efficiency with 3 dB bandwidth of 42 nm is demonstrated. Fabrication tolerances of the partially etched fourth order surface normal vertical to in –plane grating coupler is presented in Figure 3-9. As before only one grating parameter was changed at a time. A relatively high single side coupling efficiency of ~ 44% is observed numerically

irrespective of the variation to any of the grating parameter.   The bandwidth is also

relatively independent of the grating parameter variation.
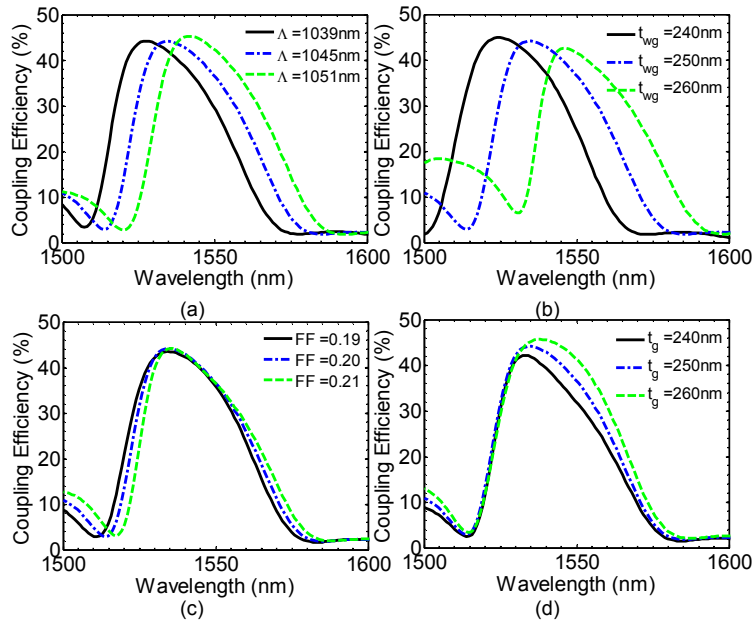
Figure 3-9: Numerically simulated fourth-order grating coupler single side coupling efficiency due to variations in (a) grating period Λ; (b) waveguide thickness t_{wg}; (c) fill factor FF; and (d) grating thickness t_g.

So far we have analyzed the coupling of the light from air in to the waveguide.

Specifically, the light couples evenly into the waveguide in the + x direction and – x

direction (Figure 3-3).   The symmetric coupling is a manifestation due to the inherent

symmetric of the grating coupler. This symmetry can be broken by the addition of a

distributed Bragg reflector in one of the arm of the grating coupler, resulting in

unidirectional coupling. Shown in Figure 3-10 (a) is the schematic of the unidirectional

surface normal vertical to in-plane grating coupler. The incident light has electric field

oriented along the length of the gratings. Three pairs of quarter wave reflectors centered

on 1550 nm are assumed in the simulation. Upon surface normal illumination, the coupled light into the backward direction (i.e. – x direction) is suppressed as shown in Figure 3-10(b). The coupling in the forward direction (i.e. + x direction) is increased. The in-plane coupling increases from 44% (Figure 3-8(b)) to 70% (Figure 3-10(c)) due to the presence of the quarter wave reflector (QWR). The spacing (s) between the QWR and the grating coupler section determines the coupling in the forward direction. This distance (s) affects the reflectivity of the in-plane of the guided mode from QWR facet resulting in interference either constructive or destructive. Consequently, we see enhanced coupling in the forward direction. With further optimization of the grating parameters, in-corporation of anti-reflection coatings and bottom Bragg reflectors, perfect surface normal unidirectional vertical to in-plane coupling in possible.
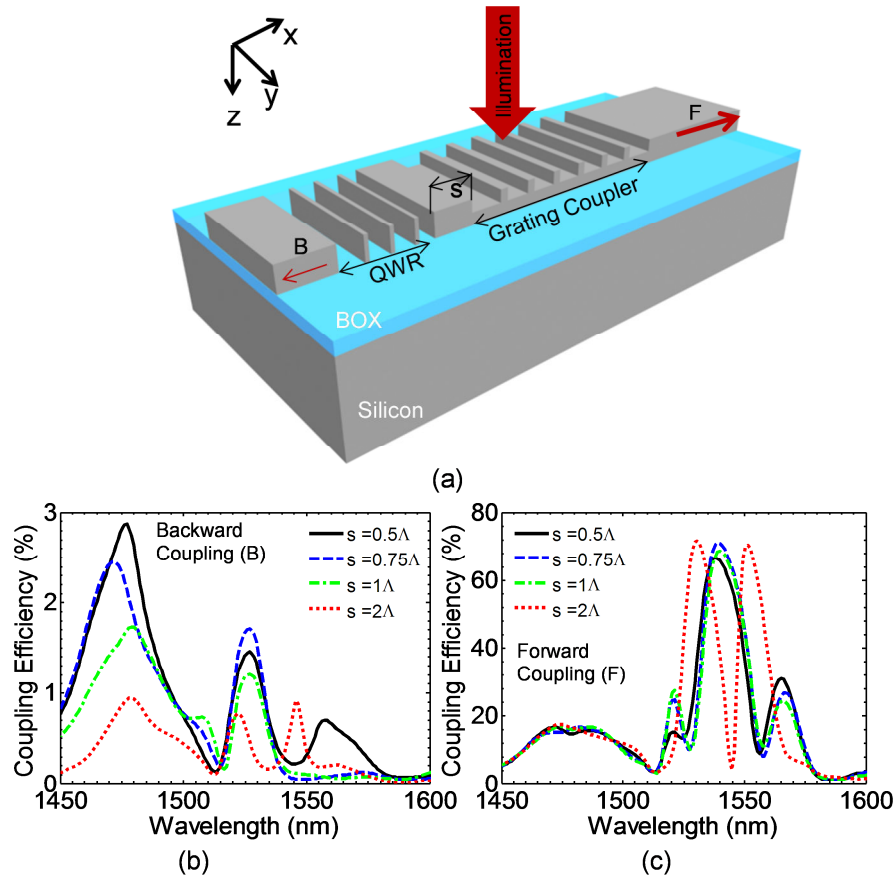
Figure 3-10: (a) Schematic of a unidirectional surface normal vertical to in-plane grating coupler. Simulated single side coupling efficiency in (b) the backward and (c) the forward direction.

Table 3.2 summarizes the surface normal to vertical in – plane grating coupler performance based on the partially etched and high contrast second order and fourth order gratings. The fourth order grating parameters were designed such that the diffracted power in the higher order modes is increased. In all the grating couplers, the buried oxide-silicon interface reflects the downward propagating wave and interferes directly with the upwards propagating wave. Thus, properly choosing the buried oxide thickness the coupling efficiency can be improved [83, 84]. The buried oxide layer acts as the lower cladding layer preventing the guided mode field from penetrating the substrate

below. The coupling will be satisfactory as long as the oxide is thicker than the evanescent fields of the guided mode. The fourth order grating coupler couples 88% of the surface normal incident light at 1,535 nm from surface normal to in-plane waveguide with 3 dB bandwidth of 42 nm. Overall, the fourth-order grating coupler has high coupling efficiency with large fabrication tolerances. The compact 20 µm size, fabrication error tolerant robust design, and bigger grating periods with high efficiency and bandwidth makes the proposed fourth-order grating coupler promising candidate for integrated silicon photonics.

Table 3.2: Summary of the grating parameters, coupling efficiency and 3 dB bandwidth of the surface normal grating coupler based on partially etched and high contract grating coupler. Second order grating parameters (*) and (**) are based on design parameters as stated in reference [12] and reference [11] respectively.

Grating Parameters	(*) Second order partially etched grating coupler	Fourth order partially etched grating coupler	(**) Second order high contrast grating coupler	Fourth order high contrast grating coupler
Period (Λ)	630 nm	1045 nm	724 nm	1045 nm
Fill Factor (FF)	0.5	0.2	0.61	0.2
Grating thickness (t_g)	70 nm	250 nm	960 nm	260 nm
Waveguide thickness (t_{wg})	220 nm	250 nm		260 nm
Gap Material	–	–	Air	Oxide
Gap thickness	–	–	250 nm	30 nm
Number of Grating elements (N)	26	19	29	31
BOX	2 µm	2 µm	4 µm	2 µm
Single side coupling efficiency	25%	44%	44%	41.25%
Total coupling efficiency	50%	88%	88%	82.5%
3 dB bandwidth	60 nm	42 nm	50 nm	26 nm
1 dB bandwidth	40 nm	28 nm	34 nm	14 nm

3.4 Fabrication and Optical Characterization of the High Efficiency Fourth Order Surface Normal Vertical to In-Plane Grating Coupler

1. EBL to define Alignment mark on SOI wafer
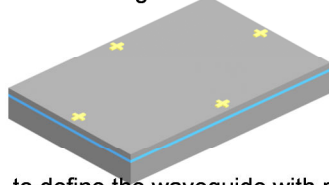
2. EBL to define the waveguide with reference to the alignment mark

3. Dry etching of Si waveguide

EAV3

8 µm

200 µm

4. EBL alignment of the gratings with reference to the etched waveguide
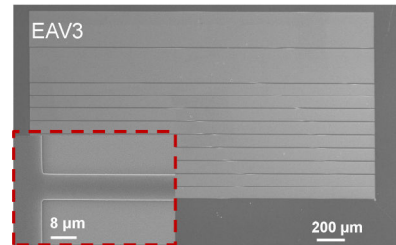
5. Dry etching of Si gratings

200 nm

2 µm
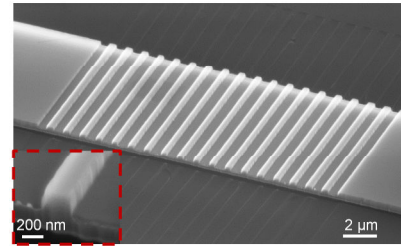
Figure 3-11: Process flow the fabrication of the high efficiency second order surface normal vertical to in-plane coupler.

The process flow for fabricating the fourth order grating coupler is summarized in Figure 3-11. Global Alignment marks are made on the starting silicon-on-insulator (SOI) substrate using electron beam lithography (EBL). The thickness of the silicon device layer is 500 nm and the buried oxide is 1 µm. Using second electron beam lithography and standard reactive ion etching (RIE) dry etch technique, an array of waveguides were fabricated. The waveguides are 10 µm and are separated by a distance of 100 µm (Figure 3-11(c)). Using third EBL, the grating patterns were aligned to the waveguides via the global alignment marks. Shown in Figure 3-11 (e) is a scanning electron micrograph zoomed in to the grating region.

The coupling efficiency was measured using the cut back method. The light was incident on the grating from top and the coupled power was measured at the cleaved facet. The grating couplers were characterized by measuring the in-coupled light spectra with an Agilent tunable laser system with 1pm resolution. The incident beam goes through an optical circulator, a laser beam collimator, an optical lens, a linear polarizer and an objective lens. The x50 objective lens with numerical aperture (NA) of 0.42 was used to reduce the spot size to 7 µm. The circular was used to ensure surface normal incidence. An infrared camera was used for initial alignment. The light coming from the cleaved is then focused onto the power detector. We measured the Fabry-Perot resonances caused by a cavity formation between the grating coupler and the cleaved facet. Shown in Figure 3-12 is the measured coupling efficiency versus wavelength. This is the optical power at the detector divided by the input power incident on the grating. The power incident on the grating is 0.5 mW. The spacing between the peaks depends on the cavity length. We measured a free spectral range (FSR) of 0.4 nm and compared it with the calculated FSR of 0.41 nm. The actual coupling efficiency from fibre to waveguide is estimated by taking into the cavity effects. Neglecting the propagation losses of the waveguide, facet reflection and the grating reflection determine the quality of the cavity. We calculate the normalized transmission for a facet reflection of 0.32 and different grating reflections. Without any grating reflection, there is no cavity and 68% of the in coupled power reaches the detector. In our measured the ratio of the peak power to the minimum power is around 1.5 and the Fabry-Perot peaks correspond to 74% of the power that is actually coupled into the waveguide. Thus, we estimate the coupling efficiency to be 20%.
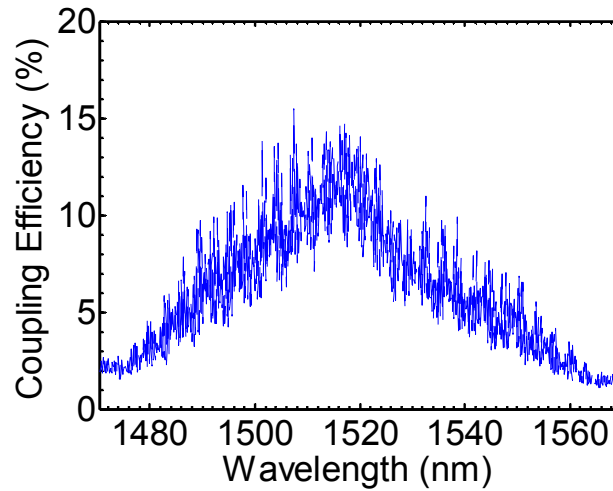
Figure 3-12: Measured coupling efficiency versus wavelength. This is the optical power at the detector divided by the input power from the fiber.

Shown in Figure 3-13 are the measured and simulated single side coupling efficiency for grating coupler with 250 nm waveguide thickness (t_{wg}), 250 nm grating thickness (t_{grat}) and 19 grating elements. The periods were varied and the fill factor (FF) of these devices was fixed to 0.3. A maximum of 20% coupling efficiency is measured experimentally. The measured 3 dB and 2 dB bandwidth are 52 and 26 nm respectively. The peak reflection occurs at the wavelength of second order Bragg back reflection. For surface normal incidence, the wavelength of peak reflection is determined by the simple phase matching condition $\lambda_p = \Lambda \, n_{eff}$, where λ_p is resonant wavelength, is the period of the grating and n_{eff} is the effective refractive index. As the period (Λ) changes, the n_{eff} changes, hence we see a linear dependence of the center wavelength as the period changes. Good agreement between simulations and measurements are observed.

(a)

(b)

(c)
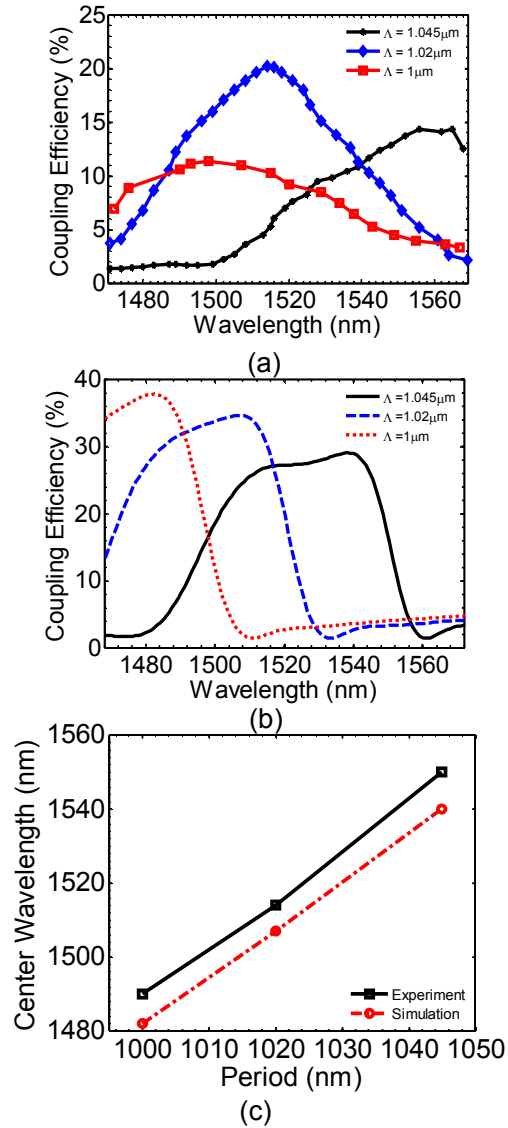
Figure 3-13: (a) Measured and (b) simulated single side coupling efficiency of the second order surface normal vertical to in-plane coupler efficiency. (c) Comparison of the experimentally measured and FDTD simulated center wavelength of the grating coupler.

Both the second and the fourth order grating couplers couple surface normal incident light with high efficiency. However, the second order coupler based on the

partially etch gratings is limited to ~ 20% single side coupling efficiency due to strong Bragg reflection. While the second order grating coupler based on the high contrast grating coupler provides high coupling efficiency and large band width of operation. The coupling efficiency drops significantly with the change in fill factor by few nanometers which make the first order grating coupler design very prone to fabrication imperfections. A large spectral shift is found with slight degradation in coupling efficiency when the waveguide thickness of the first order coupler is changed only by few nanometers as compared to insignificant change in the efficiency or the spectral shift of the coupling band of the second order coupler. The fourth order coupler can be easily implemented on a standard SOI wafer as compared to more demanding second order grating coupler design parameters. The larger periods of the fourth order grating also facilitates the use of deep UV lithography as compared to more expensive and time consuming electron beam lithography for the smaller design parameters of the first order grating coupler. Overall, the second order grating coupler gives high coupling efficiency despite the fabrication imperfections. The compact 20 μm size, fabrication error tolerant robust design, and bigger grating periods with high efficiency and bandwidth makes the proposed fourth-order grating coupler promising candidate for integrated silicon photonics. We have numerically demonstrated a fourth order vertical to in-plane optical coupler based on a 1-D grating in a SOI waveguide. The fourth order grating coupler couples 88% of the surface normal incident light at 1,535 nm from surface normal to in-plane waveguide with 3 dB bandwidth of 42 nm. We experimentally demonstrated 20% single side coupling efficiency with 3 dB bandwidth of 52 nm. The device is very compact and couples light only to TE-modes of the planar waveguides. Therefore, it may be used in a polarization diversity configuration to implement a polarization insensitive photonic integrated circuit based on photonic crystal waveguides.

Chapter 4

Anti-Reflection Coatings

4.1 Background of Anti-Reflection Coatings

The overall efficiency of optical devices, e.g., solar cells, detectors, scope optics, or remote imaging cameras, can be improved by reducing the reflection of the light from the surface. A perfect anti-reflection coating (ARC) eliminates the reflection from an interface between two media for all wavelengths, polarizations and angles of incidence (AOI). The graded index (GRIN) ARC, where the refractive index (RI) is gradually transitioned between the two media using porosity or tapered nanostructures, gives extremely low reflection over a broad spectral range for a wide range of incident angles (i.e. omni-directional ARC, or Omni-AR) [85, 86]. Single- or multi-layer quarter-wavelength stack and graded index layers are two prevalent anti-reflection schemes.

The multilayer coating structure gives low reflection but is relatively narrow band and the reflection increases across the spectrum as the AOI increases [87]. The design of the multi-layer ARC is further complicated by the availability of the material with the correct refractive index and the optical transparency. Graded index layer scheme is more widely used to suppress reflection over a broad band. Reduced reflection results in improved light coupling. Porous structures can be fabricated easily using electrochemical etching or glancing angle deposition (GLAD) [88-92]. The GLAD process is not material specific and can be deposited on any flat surface. Reflection less than 3% is observed for AOI up to 30^0 using GLAD process. The porous structures are fragile and easy to break. It is also difficult to control the effective refractive index and the charge transport is hindered significantly due to porosity. The porous structures formed by wet etching are limited to crystalline substrates and the GLAD process involves complex and costly fabrication. A recent review on modern techniques shows the use of nanostructures to

generate anti-reflection properties [93-95]. The following section discusses the potential of graded index film for improving the light coupling into conventional solar cells. A design methodology is developed to relate nanostructures as an effective GRIN film to design a near perfect anti-reflection coating. Finally, optical designs for the omni-directional ARC on rigid and flexible surfaces accounting for the process variation from commercially viable resonant infrared matrix-assisted pulsed laser evaporation (RIR-MAPLE) technology are investigated.

<u>4.2 Light Coupling In Conventional Solar Cells</u>

Light coupling in conventional solar cells is achieved by surface texturing. The surface texturing reduces front surface reflection thereby increasing the transmission into the cell. The light coupling into conventional solar cells is achieved by textured surfaces that serve as anti-reflection coating. Broadly speaking the textured surfaces can be fabricated by etch down or bottom up methods

4.2.1 Etch Down Methods

The anisotropic etching and laser ablation are the predominant etch down methods to improve light coupling into the silicon solar cell [96-98]. Other etch down techniques used for surface texturing include isotexturing, reactive ion etching mechanical scribing masked isotropic etching, acid etching and laser ablation [99-104]. These etch down methods are associated with texturing the solar cell by means of removal of the cell material. Specifically, these methods are no applicable to thin solar cells on flexible cheap organic substrates.

4.2.2 Bottom Up Methods

On the other hand, the bottom up method does not involve any etching of the active solar cell material. The textured surface is usually built upon the front surface of

41

the solar cell. This surface texture reduces the front surface reflection and increases the transmission into the solar cell. Biometric moth eye nanostructures on silicon or acrylic resin have demonstrated ultra-low broadband (< 1%) average reflection [105, 106]. Hemispherical texturing is low cost and easy to implement using convective/spin coating techniques that are compatible with micro fabrication process. Reflection less than 8% is observed for AOI up to 60^0 [86], Recently, we also demonstrated omni-directional anti-reflection coating from large area imprinted surface texture [107]. The inverted pyramids are textured onto cell surface using a resin imprint process. The process can be deployed for large-scale manufacturing and can be integrated on different solar cell substrates. The optical performance and efficiency improvement due to the surface texture on commercial amorphous Si solar cells is presented.

(a)   (b)
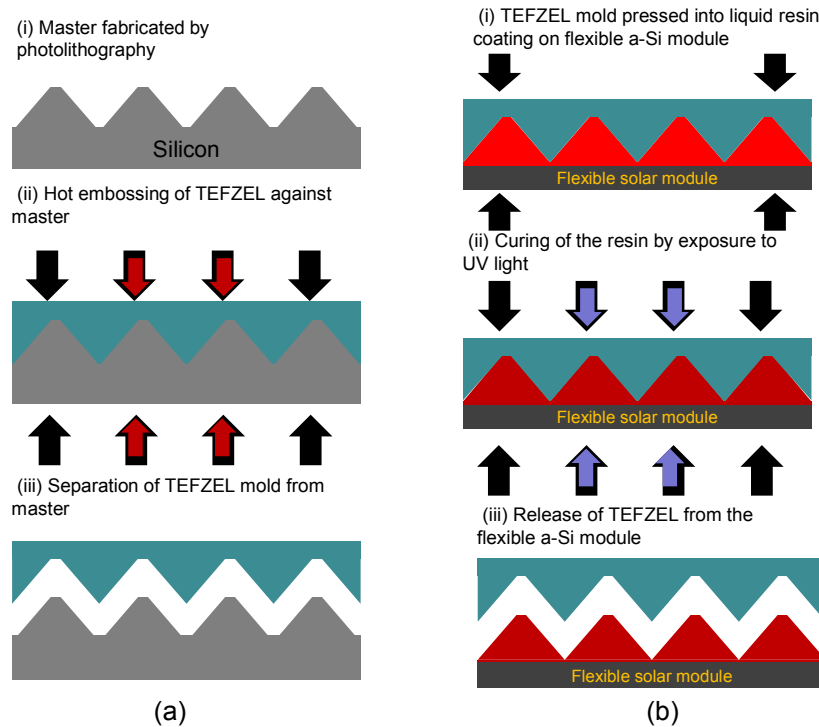
Figure 4-1: Schematic of the Fano Resonance enhanced photonic crystal Infrared Photodetectors based on transfer-printed InGaAs/Si nanomembranes

Figure 4-1 illustrates the process flow for the resin imprint surface texture. The Si master mold was prepared using photolithography with SiO_2 as the mask with 10 µm periodicity and square base of 9 µm, and then etched using 30% (by weight) KOH at 75^0C. The reverse molds were fabricated by hot embossing a Tefzel 50 µm ETFE film using the master mold. When a liquid resin film is applied to cell surface, a second imprint step was performed in a Nanonex nanoimprinter using the flexible, transparent reverse mold to create the inverted pyramid array in the resin film. UV curing of the resin film was performed through the transparent mold. The mold was then peeled off due to non-stickiness.

Commercial amorphous Si solar cells were used with an active area of 2×1.4 $inch^2$. The cells were encapsulated in plastic. We peeled off the plastic encapsulation layer and measured the I-V characteristics. Proper care was taken to ensure minimal degradation in the photovoltaic parameters. The total reflection of the resin imprint surface texture was measured under normal incidence using an integrating sphere. The surface roughness of the cells before the texture was measured with an Alpha Step IQ surface profiler. Solar cells, with and without the resin imprint texture, were characterized by the I-V measurement. With illumination under AM 1.5 conditions (100 mW/cm^2 and 25^0C), the I-V characterization yielded fill factor (FF), open-circuit voltage (V_{oc}), short circuit current (I_{sc}), and efficiency. From these parameters, the maximum power P_{max} and relative enhancement in efficiency was calculated.
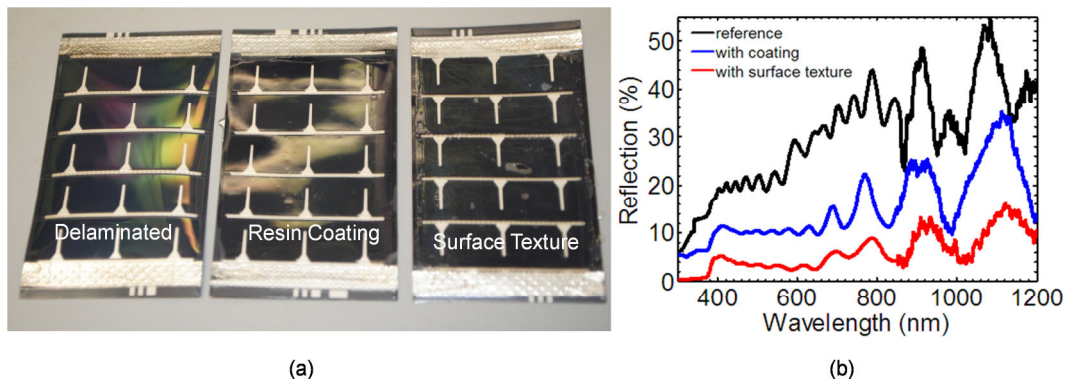
Figure 4-2: (a) Optical micrograph of a delaminated amorphous Si cell (left), resin coating on delaminated amorphous Si cell (middle) and the resin imprint texture on an amorphous Si cell (right). (b) Measured normal incidence reflection for a delaminated cell (black), cell with a low index resin film (blue), and cell with an inverted pyramid texture (red).

Figure 4-2 (a) shows the optical micrograph of an amorphous Si cell without and with the inverted pyramid texture. Measured reflection spectra shown in Figure 4-2 (b) were carried out at normal incidence. The textured cell appears dark in color, indicating less reflection as compared to the more reflecting untextured cell. In the absence of a resin film, the higher index TCO of the solar cell is exposed to air, thus we see more reflection. The low index resin reduces the reflection since the index contrast is reduced. Moreover, the resin imprint texture reduces reflection in a wide spectral range of 300 – 1,200 nm, illustrating its broad-spectrum nature. The reflection at the front surface of the texture can be recaptured by second and third hits, so the losses at the front surface are low. The multiple reflections increase the amount of light trapping and are expected to improve the efficiency of the cell.

To ensure that the amorphous Si cells to be textured had consistent properties, we measured I-V characteristics of many devices before and after delaminating the encapsulation. Minimal to no degradation was seen in the delaminated cells. The delaminated cells were mounted on a variable-angle stage that was used to adjust the incident angle of light from the solar simulator (normal to 60º, increments of 10º). Shown

in Figure 4-3(a) is the measured angle-dependent I-V characteristic of an amorphous Si cell before and after the resin imprint texture. Figure 4-3 (b) shows the I-V characteristics of an amorphous Si cell before and after a low index untextured resin coating.
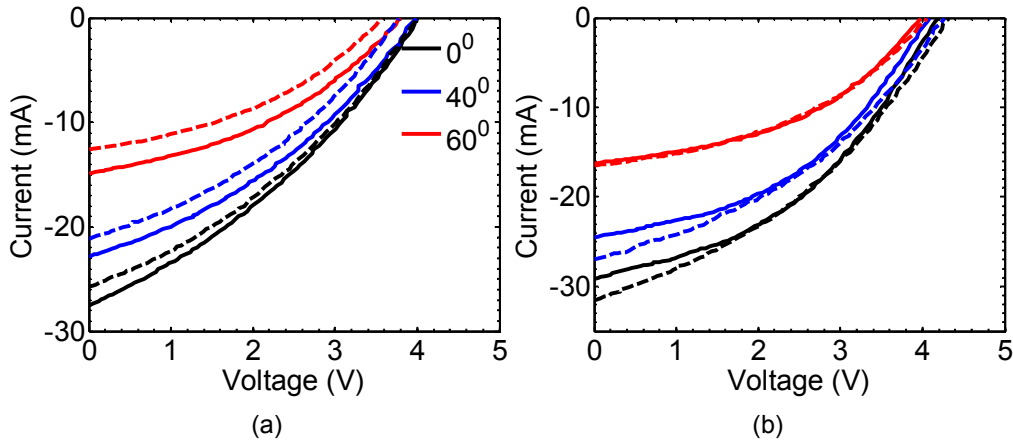
Figure 4-3: Measured I-V characteristics of amorphous Si cells: (a) before (dash) and after resin imprint texture (solid) and (b) before (dash) and after a low index resin film with no texture (solid) under AM 1.5 solar simulator at room temperature.

With the use of the surface texture (Figure 4-3 (a)), the omni-AR coating the open-circuit voltage V_{oc} remains unchanged and the short circuit current I_{sc} increases for all incident angles measured. When we use a low index resin on amorphous Si solar cells, the P_{max} reduces monotonically from 10^0 to 40^0 beyond which it increases as compared to the P_{max} of the uncoated cell. A large improvement is seen at large angle of incidence. This improvement demonstrates the omni-directionality of the inverted pyramid texturing for improved light absorption with reduced reflection over a wide spectral range and a large range of angles of incidence. With surface texture, V_{oc} remains largely unchanged. However, I_{sc} increases significantly. This suggests improved light coupling into the amorphous Si cell, thereby giving larger P_{max}. Care was taken to ensure the measurement conditions were repeatable for various incident angles and for solar cells before and after the texture. A set of four solar cells was measured to minimize statistical

45

variations associated with the test setup. The efficiency enhancement is the ratio of the power conversion efficiency with texture (coating) to the power conversion efficiency without texture (without coating). From Figure 4-4 it is evident that the resin imprint texture improves efficiency. The relative efficiency enhancement for the cell coated with low index resin with no texture at 60^0 is only 2.4% due to the reduced absorption in optical power. On the other hand, for the cells coated with the omni-AR texture the improvement is more significant at larger incident angles, with maximum relative efficiency improvement of 22% at 60°. Therefore, this resin imprint texture is more suitable for fixed-orientation solar cells, such as those installed on rooftops, for increased power output in early mornings and late afternoons.
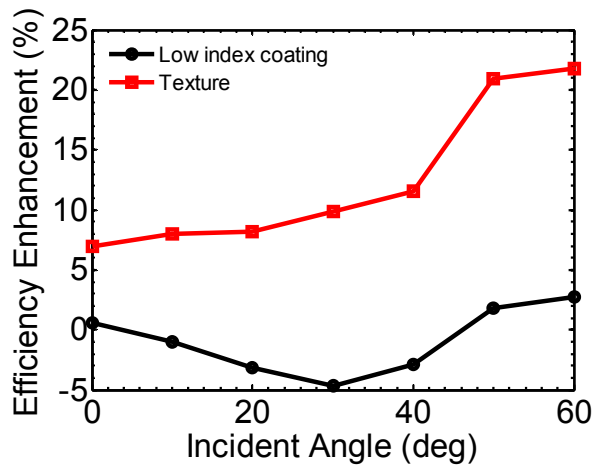
Figure 4-4: Statistics of relative enhancement in efficiency as a function of incident angle for six amorphous Si cells with the low index resin coated and Omni-AR textured structure.

The resin imprint process was demonstrated for omni-directional anti-reflection on flexible amorphous Si solar cells. The inverted pyramid texture from a Si master mold is transferred on amorphous Si solar cells. The texture reduces reflection of the cells in the spectral range of 300 – 1,200 nm, thus broad spectrum. Moreover, the texture

improves the efficiency of the cells at various incident angles from surface normal to 60°. The efficiency improves at larger incident angles to as high as 22% relative to the untextured cell. The improved efficiency is largely due to increased short circuit current. The efficiency improvement is attributed to the increased light coupling into the cells. The results show a promising method for surface texturing for all types of cells- crystalline Si, amorphous Si, thin film, and organic solar cells.

4.3 Near Perfect Anti-Reflection Coating
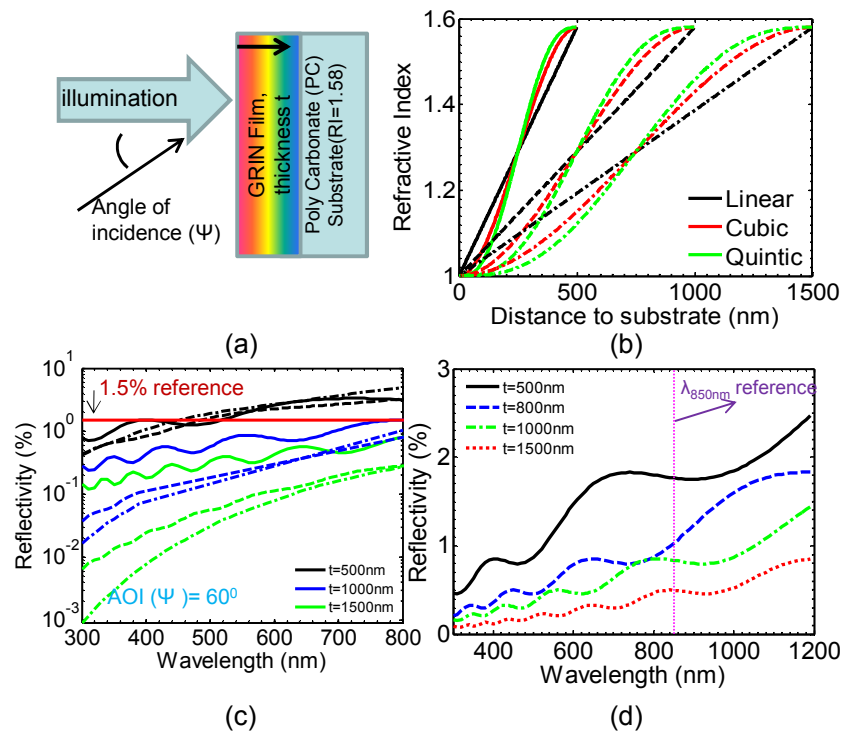
Figure 4-5: (a) Schematic of the GRIN film structure on Polycarbonate (PC) substrate; (b) Three different GRIN index profiles for different film thicknesses; (c) Simulated reflection spectra for different film thicknesses at 60^0 AOI. The solid, dash and dash-dot line correspond to the linear, cubic and quintic GRIN profile respectively; (d) Simulated reflection spectra for the linear GRIN at 60^0 AOI.

All the nanostructures gradually taper from the wide base to a fine point acting like a GRIN film. Clearly, different shape and sizes of the nanostructures give low reflection. However, there is not much clear understanding as to what shape and size will give us near perfect ARC behavior. We propose a methodology to relate the nanostructures of different shapes and sizes as an equivalent GRIN film. We investigate the rate of change of the RI as a function of the nanostructure thickness. Comparing the RI profile of a nanostructure for a given thickness to that of an equivalent GRIN film we can find the minimum feature size to give near perfect ARC. In this paper we focus the design of nanocone ARC structures that allow over 98.5% transmission over a broad visible spectral range with cone angles up to 120^0. We also compare the nanocone structures to pyramid, hemisphere and paraboloid structures in order to achieve a practical balance between high performance and manufacturability.

GRIN structures have been extensively investigated with various index profiles. [108-112] Here we consider GRIN structure on polycarbonate (PC) substrate, with film thickness t, as shown in Figure 4-5 (a). In our design, we consider three typical index profiles following linear, cubic, and qunitic functions (Figure 4-5 (b)). The PC substrate has index of 1.58 and the incident medium is air. 1,000 layers are used to simulate the GRIN film. The reflection simulations for the GRIN films were performed using rigorous coupled-wave analysis (RCWA) technique [42, 43] to compute transmission and reflectance. All the geometries are represented by rectangular blocks with a staircase like approximation.

The simulated reflectivity spectra is shown in Figure 4-5 (c), for different GRIN film thicknesses following three different index profiles at 60^0 angle of incidence (AOI). Generally the reflection increases with the increases of wavelength and AOI. Based on the simulation results, linear GRIN film has the highest (worst) reflectance as compared

48

to the other two types of GRIN films following cubic or qunitic functions. Thus, it is sufficient to model a linear GRIN film with minimum film thickness and maximum AOI (60^0) for R < 1.5% over broadband spectral range (400 – 850 nm) and wide AOI (0º – 60º). Shown in Figure 4-5 (d) are simulated reflection spectra for linear GRIN films with different thicknesses at 60^0 AOI. It is apparent that the maximum reflectance reduces with the increase of the linear GRIN film thickness. A minimum linear GRIN film thickness of 800 nm is needed in order to achieve R < 1.5% over a broadband spectral range and wide range of AOI (up to 60^0). In other words, if the change of index (n) with reference to the GRIN film thickness (t) dn/dt is less than 0.725 μm^{-1}, we can achieve R<1.5% over the target spectral band and the wide range of AOI. Based on these findings, we can now design a nanocone structure that will have performance similar to or better than a linear GRIN film. As long as the refractive index of the nanostructure changes at a lower rate, it is assured that the reflection will satisfy the design constraints.

4.3.1 Near Perfect Anti-Reflection Coating from Nanocone Structures

The effective RI of a nanocone structure increases from the index of the air to that of the substrate so that the gradual change in the RI reduces the reflection of light at substrate surface. The size and spacing of the features are sub-wavelength so that effective index theory can apply. Closely packed square lattice is used for simulations of the nanocone structures. The nanostructures are made of the material with the refractive index of 1.58, the same as that of the PC substrate. Figure 4-6(a) shows the three dimensional schematic of the nanocones used to represent the GRIN film and the effective refractive index profile for nanocones with base diameter of 281 nm. The green dash curves shown in Figure 4-6(c) represent the effective index of the nano cones with

different nanocone heights. The black (I), blue (II), red (III) and purple (IV) solid curves corresponds to the effective refractive of a linear GRIN film corresponding to (dn/dt) of 1.16 µm^{-1}, 0.725 µm^{-1}, 0.58 µm^{-1}and, 0.386 µm^{-1} respectively.

| (a) | (b) | (c) |
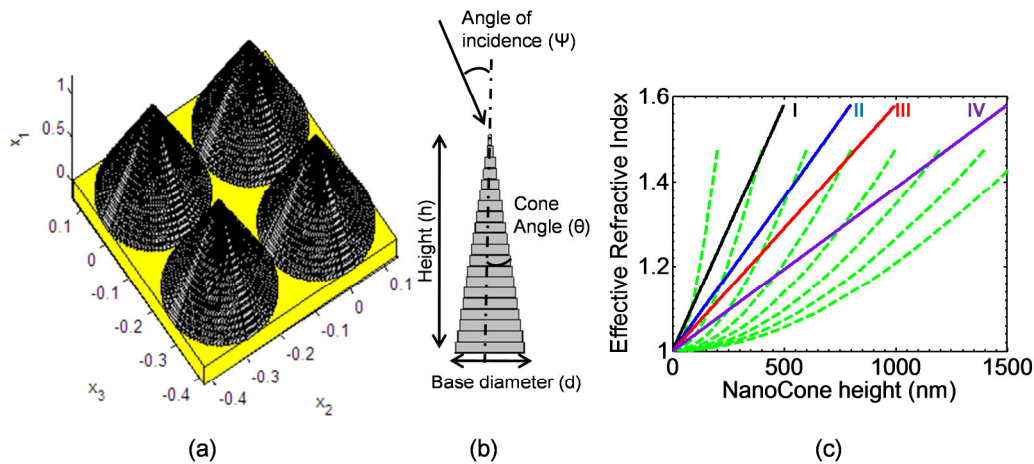
Figure 4-6: (a) Three dimensional (3D) schematic of the closely packed nanocones in a square lattice; (b) Schematic of the nanocones used for simulations showing the staircase like approximation of the nanocones with definitions of key parameters; (c) Simulated effective refractive index of different heights of the nanocones (green dash lines). Also shown are four solid curves with different effective index change rate (dn/dt) of 1.16 µm^{-1}(black, I), 0.725 µm^{-1}(blue, II), 0.58 µm^{-1} (red, III) and 0.386 µm^{-1} (purple, IV), respectively.

Based on the earlier discussions about GRIN film, to achieve low reflection (< 1.5%) over the entire spectral range (400 – 850 nm) for incident angles up to 60^{0}, the refractive index change rate (*dn/dt*) should be less than 0.725 µm^{-1}. Based on the *dn/dt* criteria, a solid blue line can be added to the figure shown in Figure 4-5(c). Based on this, we can predict that the nanocone height should be equal to or greater than 800 nm. To verify our predictions, we carried out RCWA simulations for closely packed nanocone ARC structures with nanocone height of 800 nm. The results are shown in Figure 4-7, with unpolarized, s- and p-polarized incident light. All three reflectivities are below 1.5% over the visible spectral range for incident angles up to 60^{0}.
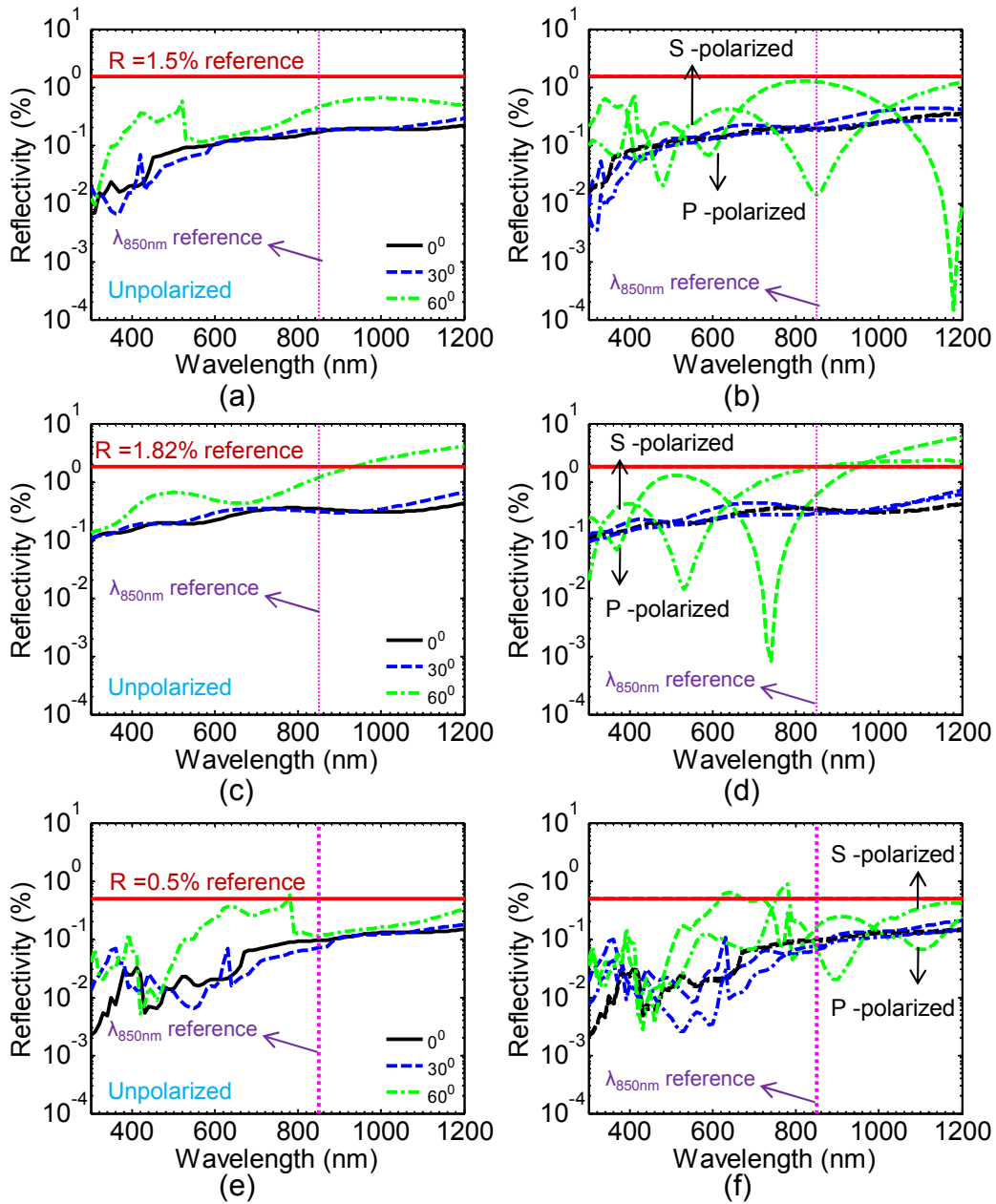
Figure 4-7: Simulated reflectivity of (a,c,e) unpolarized, (b,d,f) s-polarized (dash-dot) and p-polarized (dash) light for the closely packed nanocone ARC with 800 nm, 500 nm and 1500 nm cone height and 8^0 cone angle.

The results agree very well with our predictions based on the effective index GRIN film simulation. On the other hand, when the height reduces to less than 800 nm, say 500 nm, the maximum reflection is greater than 1.5% (Figure 4-7(c-d)).To verify the effectiveness of our process, we simulated the same nanocone AR structure with height of 1,500 nm, with the results shown in Figure 4-7 (e-f). Based on the predictions shown in Figure 4-5(d), we should expect the peak reflection for the unpolarized light should be < 0.5% for t=1,500 nm over the spectral range of 450 – 850 nm over 0 – 60^0 AOIs. The results shown in Figure 4-7 do supporting our predictions.
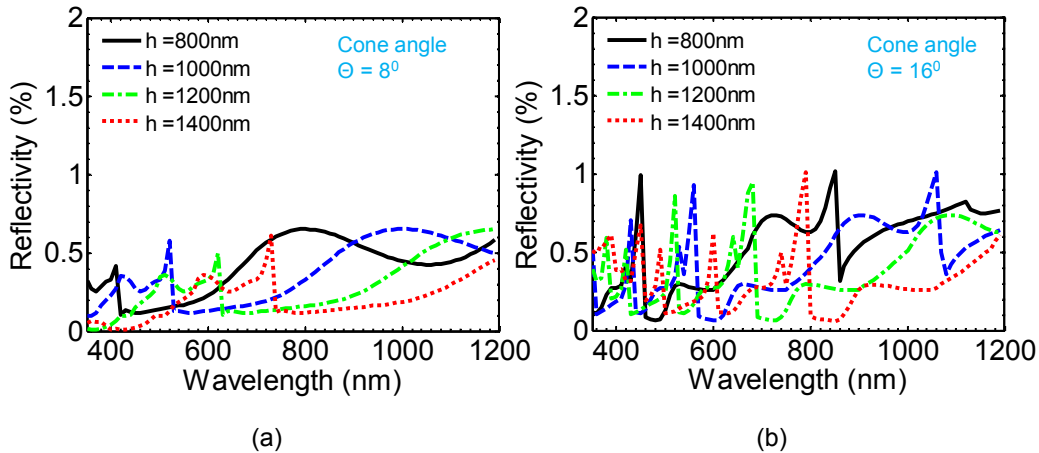
Figure 4-8: Simulated reflectivity at 60^0 angle of incidence of the closely packed nanocone ARC with (a) 8^0 cone angle and (b) 16^0 cone angle.

Next we consider the effect of changing the cone angle and the height of the nanocones. In order to study the aspect ratio we kept the height constant and changed the base diameter of the nanocones. For wavelengths greater than the base diameter of the cone, $\lambda > d$ the reflectance is low. When the base diameter d is greater than the wavelength, then the nanocones act like a diffraction grating. The high order diffractive light propagates and increases reflection. Reflectance maxima are seen in Figure 4-8 and are related to the ratio of the nanocone height to the wavelength, h/λ [113, 114] The

reflection does not change much as the cone height increases. The maximum allowed nanocone angle is 16^0 for nanocone height greater than 800 nm. The reflection remains below 1.5% for wavelengths up to 850 nm and incident angles up to 60^0.
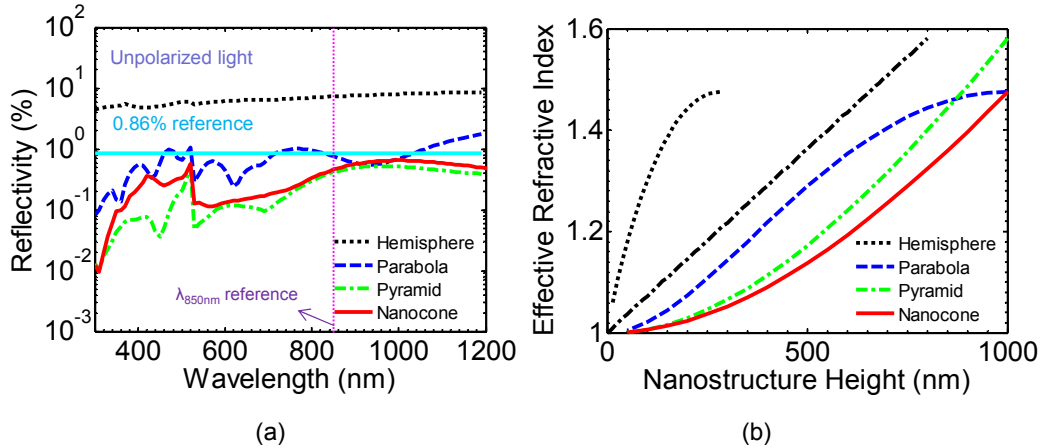
Figure 4-9: (a) Specular reflection at 60^0 AOI, and (b) Effective refractive index for hemisphere, parabola, pyramid and nanocone nanostructures. Also shown in black dash line is the effective index plot with index change rate (dn/dt) of 0.725 μm^{-1}, corresponding to the criteria for R<1.5%.

An obvious question arises: can we get ARC properties from other shapes? To answer this question we investigated common surface structures like hemisphere, parabola, and pyramid with similar structural parameters. All the structures are simulated on polycarbonate substrate with period of 281 nm at height of 1 µm at 60^0 angle of incidence. Shown in Figure 4-9(a) is the simulated specular reflection for various nanostructures considered here. Shown in Figure 4-9 (b) are the effective refractive index plots for these nanostructures with different heights. Considering the base period of 281 nm, the height of the hemisphere is 140 nm (radius). Hence its effective RI lies to the left of the linearly graded 0.8 µm GRIN film (with dn/dt=0.725 μm^{-1}), and the reflection is greater than 1.5%. The effective refractive index of the nanocone changes more gradually as compared to that of the parabolic cone hence we see less reflection for the

nanocone structure. However, the pyramid structure is index matched to the substrate hence has slightly better performance. Due to enhanced second strike [115] in the pyramids we see lower reflectance at shorter wavelengths. As the wavelength increases and becomes comparable to the height we see similar reflectance for the pyramids and nanocones.

4.3.2 Near Perfect Anti-Reflection Coating from Graded Refractive Index (GRIN) films

An ideal technology for making GRIN films from either organic or inorganic materials should be such that it provides broad band anti-reflection coating over wide range of wavelengths and incident angles. The technology should also be able to coat rigid or flexible substrate, flat or curved shapes and organic or inorganic substrates. Earlier while we demonstrated that nanostructures can serve as near-perfect anti-reflection coating, coating them on curved surfaces is quite challenging. On the other hand, the conventional inorganic anti-reflection coatings are susceptible to delamination when coating on organic substrates. A broadband omnidirectional organic AR coating requires refractive index matching from that of an organic substrate (n = 1.4 – 1.6) to that of the surrounding medium (usually air with n = 1.0). However, the bulk polymers cannot achieve RI values significantly below the theoretically determined limit of n = 1.29 making the index matching challenging [116]. Resonant infrared, matrix-assisted pulsed laser evaporation (RIR-MAPLE) is yet another means of offering a straightforward approach to enabling the required GRIN profile on organic substrates.[117, 118] The resonant infrared matrix-assisted pulsed laser evaporation (RIR-MAPLE) deposition technique can control the polymer blend domain sizes and continuously vary polymer blend ratios over a given film thickness. Thus is allows substrate independent broad band omni directional antireflection coating.

The following section describes the modeling of the graded refractive index (GRIN) anti-reflection (AR) coating for a polycarbonate substrate. The design criteria is to achieve less than 0.5% with transmission greater than 99.5% over a cone angle of 120^0 from a curved polycarbonate substrate. Since the reflection increase at higher incident angles, it is sufficient to simulate the GRIN film on the polycarbonate substrate with an incidence angle of 60^0. The GRIN-AR coating is modeled as a stack of 10 nm thick layers on polycarbonate (PC) substrate as shown in Figure 4-10(a). The transmission and reflection simulations for the GRIN films were performed using rigorous coupled-wave analysis (RCWA) technique [119]. A non-dispersive refractive index of 1.58 for the PC substrate was assumed in the simulations. Linear, cubic, quintic and exponential sine gradient films were investigated in the simulations [112, 120, 121]. The simulations predict that the reflection stays below 0.5% with transmission greater than 99.5% at angles of incidence as large as 60º throughout the visible spectrum (400 – 750 nm) for 1 μm thick exponential sine and cubic GRIN film.
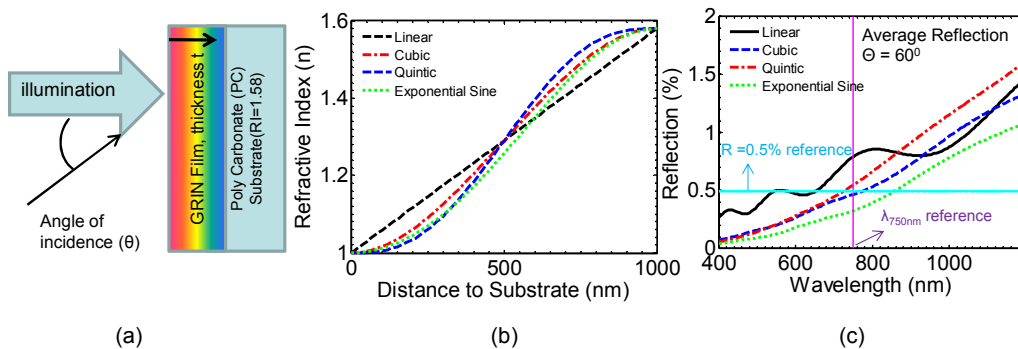
Figure 4-10: (a) Schematic of the GRIN film structure on Polycarbonate (PC) substrate; (b) Four different GRIN index profiles for 1 μm film thickness; and (c) Simulated reflection spectra for 1 μm thick film with different GRIN index profiles at 60^0 angle of incidence (AOI).

The resonant infrared matrix-assisted pulsed laser evaporation (RIR-MAPLE) deposition technique can control the polymer blend domain sizes and continuously vary

polymer blend ratios over a given film thickness. Of concern, is the limitation of the process control with the present MAPLE experimental setup that how quickly the polymer blend ratio is changed in 10 nm intervals? To ensure that the GRIN-AR prototype would still be effective we compare the rate of change of the PMMA to PS volume ratio for different graded index profiles. Shown in Figure 4-11(a) is the volume ratio of PMMA to PS for the four different graded index profiles. The thickness of each index profile is selected such that they give reflection less than 0.5% throughout the visible spectrum at incident angles as large as 60^0. All the simulations assume 60^0 angle of incidence unless otherwise stated. While 1 µm thick cubic graded film can meet the design criteria, it demands drastic volume ratios both at the air and GRIN film interface and GRIN film and PC substrate interface. On the other hand, linear GRIN film requires easily achievable PMMA to PS volume ratios. However, in order to meet the design criteria the linear GRIN film thickness should be increased to 1.4 µm. Bruggeman's effective medium theory [122], shown in Equation 4.1, is used to determine the volume ratio between PS and PMMA that yields a desired effective RI after the PMMA component is dissolved:

$$f \frac{n_a^2 - n^2}{n_a^2 + 2n^2} + (1 - f) \frac{n_{ps}^2 - n^2}{n_{ps}^2 + 2n^2} = 0; \qquad\qquad (4.1)$$

where f is the volume fraction of air pores; (1-f) is the volume fraction of the PS network; n_a is the RI of air (1.0), n_{ps} is the RI of PS. A non-dispersive refractive index of 1.58 is assumed for PS. It is assumed that the pore size is significantly smaller than the wavelength of incident light to avoid and scattering [123].
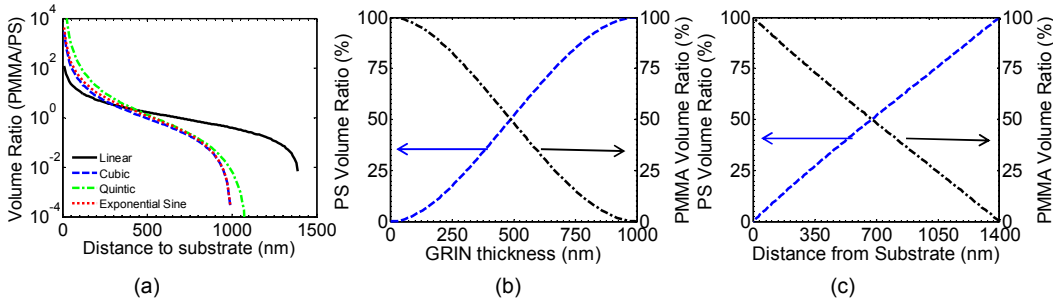
Figure 4-11: (a) Volume ratio of PMMA to PS for the four different GRIN index profile with corresponding thickness satisfying the design criteria. PS and PMMA volume ratio for (b) 1 µm thick cubic graded index film and (c) 1.4 µm thick linear graded index film.

The exponential sine grading demands extreme volume ratio compared to an easily achievable volume ratio for the linear grading. However, the linear grading requires a thicker film that increases the film growth time. Thus as a compromise we choose 1 µm cubic graded film. So far we have assumed infinite polycarbonate substrate. In practical applications, we need to consider the effect of finite substrate. Shown in Figure 4-12 (a – b) are the schematic of the cubic GRIN film on an infinite and 1 mm finite polycarbonate substrate. The reflection is below 0.5% for the cubic GRIN film with thickness greater than 1 µm, when it is placed on an infinite polycarbonate substrate (Figure 4-12 (d)). When the GRIN film is placed on top of the 1 mm thick   polycarbonate substrate, the reflection is greater than 0.5% for cubic GRIN films as thick as 1.6 µm (Figure 4-12 (e)). While the GRIN film provides and effective index matching from air to polycarbonate substrate, the bottom surface of the substrate reflects light back towards the top surface. The reflected light then experiences a gradual index matching from substrate to air. Hence the light effectively leaks out from the incident light region and the reflection increases. In order to mitigate the effect of the increased reflection due to finite substrate, we can place another GRIN film of same thickness on the back side of the substrate as shown in substrate Figure 4-12 (c).
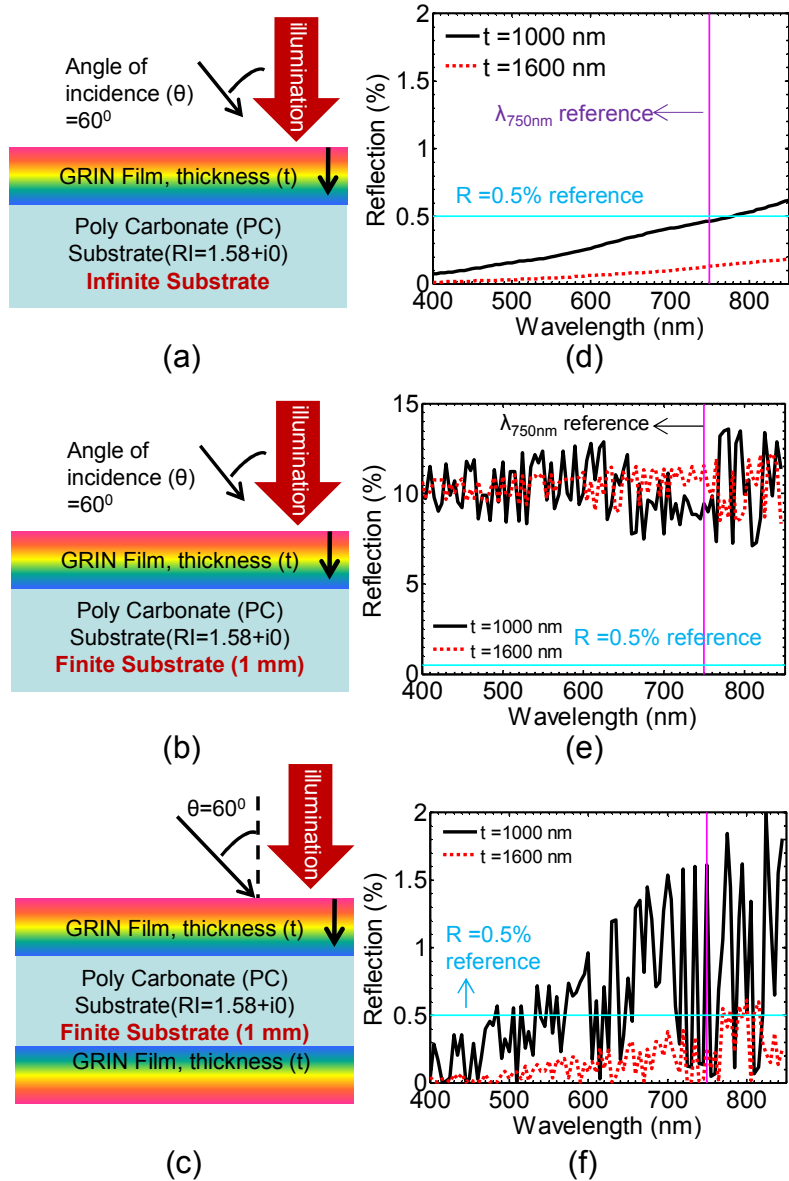
Figure 4-12: Schematic of the cubic GRIN film on top of (a) infinitely thick (b) 1 mm thick poly carbonate substrate; and (c) cubic GRIN film on either side of the 1 mm thick poly carbonate substrate. Simulated reflection of the cubic GRIN film on top of (d) infinitely thick (e) 1 mm thick poly carbonate substrate; and (f) cubic GRIN film on either side of the 1 mm thick poly carbonate substrate

The GRIN on the side of the substrate provides index matching from substrate to air at the transmitted light region. Hence the reflection remains lower than 0.5% as shown in Figure 4-12 (f). The oscillations in Figure 4-12 (e – f) are the Fabry-Perot oscillations due to the finite thickness polycarbonate substrate. The free spectral range of the oscillations is much smaller than the simulated wavelength step of 5 nm.

Next we consider the effect of non-uniform deposition on flat and curved surfaces. The non-uniformity during the deposition process might lead to non – uniform thickness across the substrate. We modeled the non-uniformities by considering a thicker or a thinner film at the edge of the substrate as compared to the center substrate. The thickness is assumed to increase linearly from a uniform thickness of 1 µm to a maximum thickness of 2 µm. The non-uniform region accounts for about 50% of the total area. For the case when the GRIN film is thicker at the edge as compared the center of the substrate, the reflection is further reduced since the index change from air to substrate is even more gradual. Thus the reflection remains below 0.5% even due to the introduction of the non – uniform deposition.
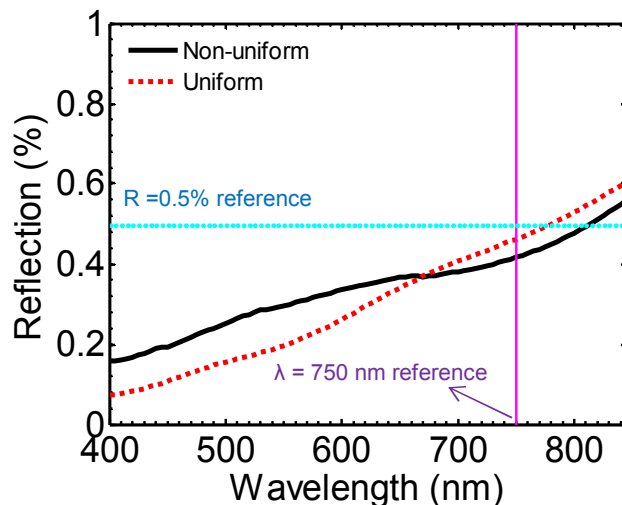
Figure 4-13: Simulated reflection from 1 µm thick (a) uniform and (b) non-uniform cubic GRIN film on an infinite polycarbonate substrate at 60^0 angle of incidence.

59

The situation is quite different when the thickness at the edge is less than the center of the wafer. Without going into the details of the origin of the non- uniformity from a pulsed laser deposition (PLD), the measured film thicknesses at different substrate-to-target distances can be approximated by the following equation 4.2. [124]

$$t = ae^{b\rho} (\cos\theta)^c \tag{4.2}$$

where a, b, c are process dependent parameters and ρ and θ are the radial distance from center of target, adjacent to θ, the zenith angle that yields a film thickness, t. Based on an experiment in collaboration with Duke University, the measured film thickness schematically appears as shown in Figure 4-14 (a). The measured film profile is approximated by a linear piecewise model with four regions (R1, R2, R3, R4) with different slopes. Infinite polycarbonate substrate is assumed for simulations. The model assumes 10 nm steps for each layer. The number of partitions within each region is determined by the slope of each region. Region R4 assumes uniform film thickness. The normalized thickness falls from unity to about 0.17 from the center to the edge of the 4 inch wafer. Cubic GRIN model is assumed for the simulations with 60^0 angle of incidence. Since the thickness at the edge of the wafer falls to 0.17 times the thickness at the center of the substrate, the reflection increases beyond 0.5% for the 1 μm thick cubic GRIN film at the center of the wafer. In order, to account for the non-uniformity, the GRIN film thickness can be increased to reduce the reflection. As expected, when the thickness of the GRIN film is 2.6 μm at the center of the wafer, the reflection reduces to about 0.59% for wavelengths up to 750 nm across the entire 4 inch wafer as seen in Figure 4-14 (b).
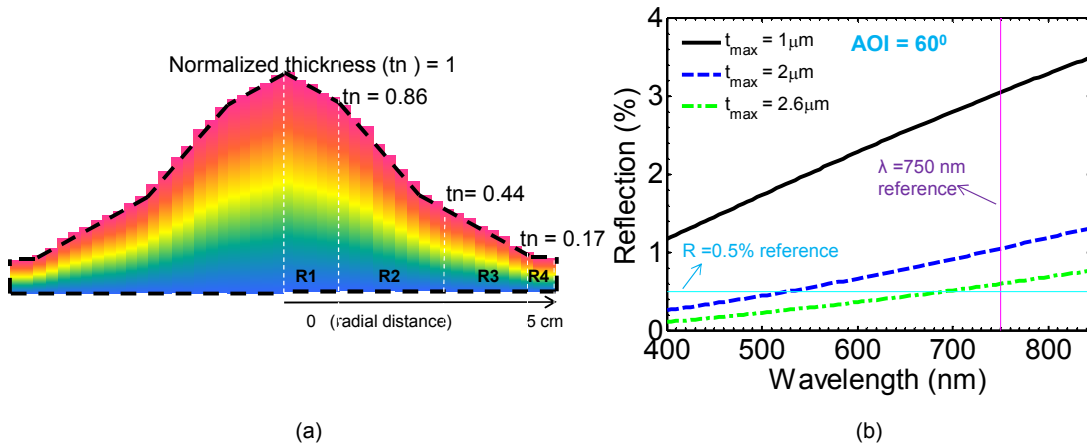
Figure 4-14: (a) Schematic of the non-uniform film deposition as fabricated by Resonant infrared, matrix-assisted pulsed laser evaporation (RIR-MAPLE) technology. (b) Simulated reflection for different the maximum film thickness (t_{max}) at the center of the substrate. The corresponding thickness at the edge of the wafer is 0.17 times the thickness at the center of the substrate.

Similarly we investigate the effect of GRIN film on a curved surface. Figure 4-15 (a) and Figure 4-15 (b) shows the schematic of a uniform and a non-uniform GRIN film on a curved substrate. The non-uniform layer is assumed to be twice as much as the compared to the uniform GRIN film thickness of 1 μm. Each color represents a unique refractive index. Infinite polycarbonate substrate is assumed with angle of incidence of 60^0. Cubic grading is assumed in the simulations. Figure 4-15 (c) and Figure 4-15 (d) shows the simulated spectral dependence of the reflection from uniform and non-uniform GRIN coating on the curved surface respectively. A flat surface is represented by a radius of curvature (R) equal to infinity. When the radius of curved is less than 51 μm, the reflection is greater than 0.5%. At lower radius of curvature, some of the incident light enters the GRIN film at a higher angle than 60^0 resulting in higher reflection. The reflection is always lower than 0.5% for all the radius of curvature greater than 51 μm. An explained previously, for the non-uniform coating case, since the thickness is greater

than 1 μm, the results closely follow the as predicted by the uniform coating case even for the curved surface.
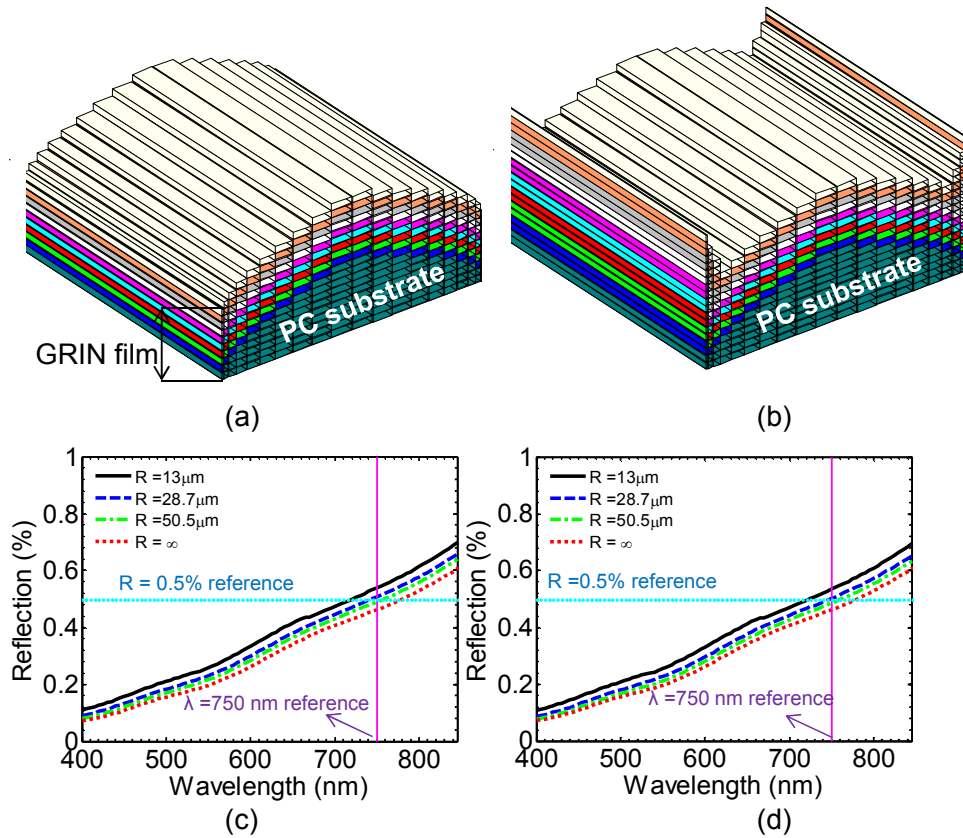
Figure 4-15: Schematic of (a) uniform and (b) non-uniform GRIN film with ten layers of distinct refractive index on curved surface. Simulated reflection from 1 μm (c) uniform and (d) non-uniform cubic GRIN film at 60[0] angle of incidence on curved surface with different radius of curvatures (R).

Chapter 5

Photonic Crystal Nanomembrane Reflector

5.1 Motivation

Over the last few years, significant research progresses have been made in the area of single layer dielectric membrane reflectors (MR), based on one-dimensional (1D) high contrast gratings (HCG) [125-129] or two-dimensional (2D) photonic crystal slabs (PCS) [130-136]. Due to the nature of the different mechanisms in these nano-structured dielectric MRs, as compared to the reflection principles in metallic reflectors and widely used multi-layer stacked distributed Bragg reflectors (DBR), it is very important to understand the angle- and polarization-dependent reflection properties [130, 131]. These properties can also be engineered by dispersion engineering of the modal properties for the desired angle- and polarization-dependent properties. 1D grating structures are intrinsically polarization – dependent. Various structures have been proposed in 1D HCG broadband reflection structures for TE (transverse electric) only, TM (transverse magnetic) only, or both TE and TM polarized light [137, 138]. Low birefringence in hollow core waveguides and broadband reflectors has also been reported in 1D HCGs [139, 140]. On the other hand, 2D PCS based MRs can be intrinsically polarization independent, due to the high symmetry properties [130, 131]. Lousse *et al.* provided detailed theoretical investigations on angle- and polarization-dependent characteristics in 2D PCS membrane reflectors [130]. Boutami *et al.* presented a design of 2D suspended InP PCS with a polarization independent reflection of ~250 nm bandwidth with reflectivity greater than 90% by exploiting two resonant waveguided modes at surface normal incidence [131]. We have reported earlier polarization independent reflections in a demonstrated MR on a glass substrate for surface-normal incident light [133, 134]. In the following section, we report detailed design and first experimental investigation of angle-

63

and polarization-dependent reflection properties in 2D PCS based membrane reflectors on silicon on insulator (SOI) substrate.

5.2 Design of the Nanomembrane Reflector

(a)   (b)
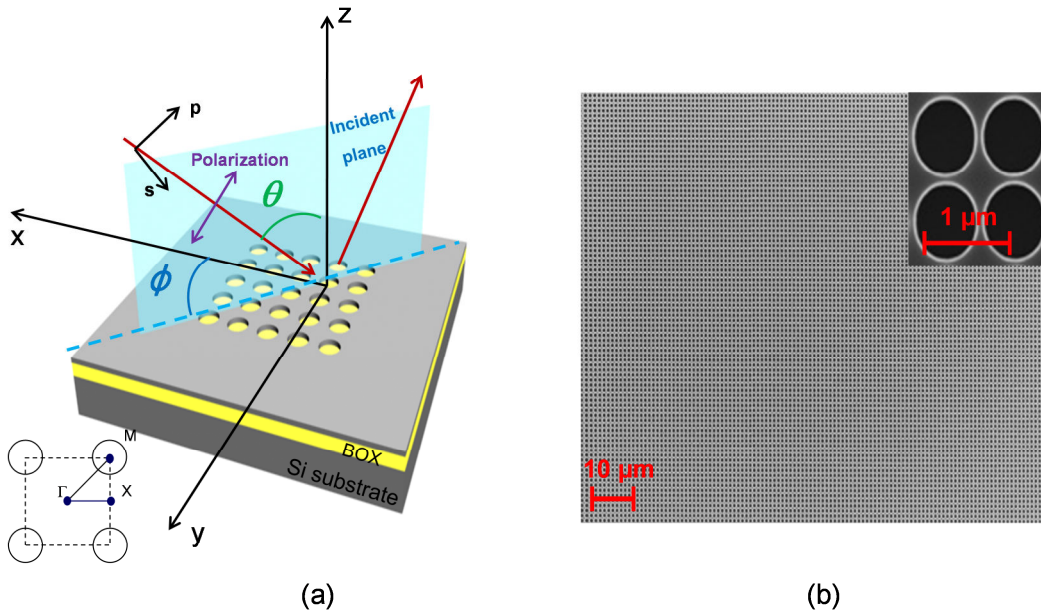
Figure 5-1: (a) Schematic of the broadband reflector with the angular and polarization definition of the incident light onto patterned SiNM reflectors. (b) SEM of the fabricated Si MR on SOI.

Shown in Figure 5-1 are the schematic and the scanning electron micrograph (SEM) of the membrane reflector under study. The incident beam direction is defined by two polar angles, the colatitude angle θ (angle from the surface-normal direction) and the azimuth angle Φ (angle from the positive x-axis to the orthogonal projection of the incident beam in the x-y plane). The incident beam polarization (E-vector) Ψ is defined as the angle from the positive x-axis to the polarization direction. The TE (s) or TM (p) polarizations are defined as the beam with E-vector perpendicular or parallel to the incident plane formed by the incident and reflected light. The conventional definition of

wave vector directions and the corresponding Brillouin zone in k-space with high symmetric points defined with Γ, X and M, respectively are also shown in Figure 5-1. The reflector was designed using Rigorous Coupled Wave Analysis (RCWA) simulations[43], with target wavelength around 1550 nm. The MR consists of 340 nm thick top Si with square lattice photonic crystal structure. The lattice constant (a) of the photonic crystal is 860 nm with the ratio of air hole radius to the lattice constant (r/a) of 0.45. It is possible to shift the spectral bandwidth and location of the reflection band by changing the geometric parameters of the reflector.

5.3 Angular Characteristics of the Nanomembrane Reflector

The simulated reflection spectra contour plots as a function of the incident angle are shown Figure 5-2(a,c) and Figure 5-2(b,d) for TE and TM polarizations, respectively. In Figure 5-2(a,b), the incident beam angle is changed from surface normal (θ = 0°) to θ = 80° in steps of 10° and Φ =0^0. At surface normal incidence, simulated specular bandwidth of 104 nm (1472 nm – 1576 nm) with reflection greater than 95% is observed for both the TE and TM polarizations. However, with the increase of incident angle, broadband high reflectivity can only be observed for TE polarizations. The TM polarization reflectivity reduced drastically with the increase of the incident angle. To better understand this phenomenon, we did a fine scan to simulate the reflectivity at small incident angles from 0^0 to 15^0. The results are shown in Figure 5-2(c, d). When the incident angle (θ) is increased from 0° to 8°, reflectivity greater than 95% is maintained for both TE (Figure 5-2(c)) and TM (Figure 5-2(d)) polarizations. At oblique incident angles, the symmetry of the square lattice is broken. For the TM polarization a transmission band opens up within the reflection band (Figure 5-2(d). This is caused by

65

the splitting of the Fano resonance or guided resonance modes. As a result, the non-degenerate modes at Γ – point begin to become coupled to the incident radiation for increasing incident angles [40, 57]. For the TM polarization a relatively narrower spectrum of 13 nm is reflected with high reflection (R > 95%).
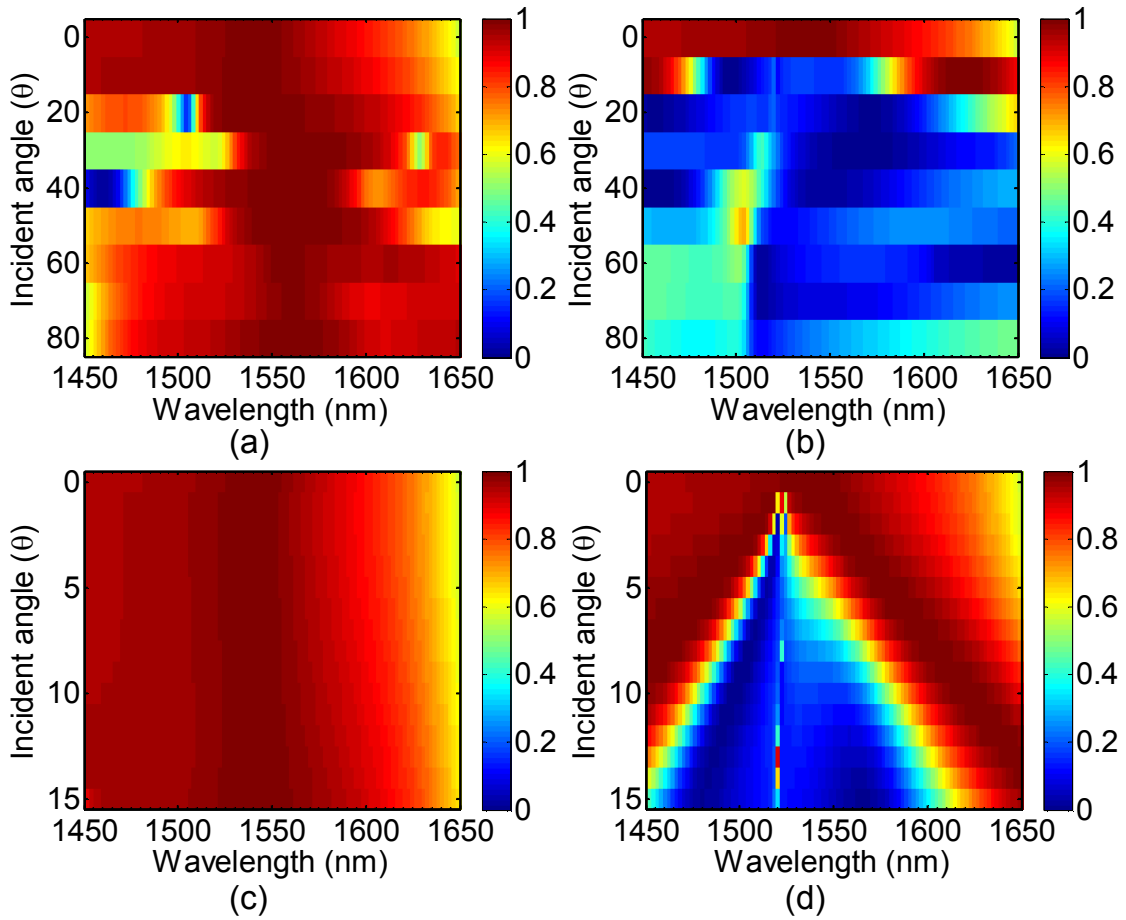
Figure 5-2: (a, b) Contour plots of simulated reflectivity over a large range of incident angles θ (given in degrees) for (a) TE and (b) TM polarized light; and (c, d) Contour plots of simulated reflectivity for close to normal small incident angles θ (given in degrees) for (c) TE and (d) TM polarized light.

Table 5.1: Simulated reflection characteristics of Si MR for different incidence angles for both TE and TM polarizations.

Polarization	Spectral range (nm)		Bandwidth (nm)	
Type (Range	R > 90%	R > 95%	R > 90%	R > 95%
TE (0 – 80^0)	1488 – 1586	1523 – 1570	98	47
TM (0 – 8^0)	1386 – 1477	1461 – 1474	91	13
TE/TM (0^0)	1388 – 1586	1472 – 1576	198	104

The TE polarized mode have less angle-dependent reflection properties, most likely related to the relatively-unchanged phase-matching conditions associated with the relatively flat modal dispersion properties.[33] TE polarized light reflects 1523 nm –1570 nm spectrum corresponding to a bandwidth of 47 nm for all incidence angles. The omni-directional reflection of this MR is limited by the incident angle dependent reflection of the TM polarization. Table 5.1 summarizes the simulated incident angle dependent reflection properties of the designed MR.

5.4 Dispersion Characteristics of the Nanomembrane Reflector

Detailed analysis of the angle dependent Fano resonant mode dispersion properties are presented in Figure 5-3. Figure 5-3(a) and Figure 5-3(b) show the reflection and transmission spectra at selected angles of θ =0^0 and 5^0 for TE and TM polarizations, respectively. The reflection at surface normal incidence (θ =0^0, Φ =0^0) indicates the broadband nature of the Si MR. Following similar approach reported earlier[141], the corresponding transmission spectra were plotted again in logarithmic scale, as shown in Figure 5-3(c) and Figure 5-3(d). At surface normal incidence, two

dominant guided mode resonances can be seen within the high reflection band where the transmission approaches zero. As the incident angle increases, more resonances are observed within the reflection band. To better understand the modal properties of these resonance modes, plane wave expansion method (PWE) was used to compute the dispersion characteristics of the NM reflector. The dispersion plot yields even and odd bands as shown in Figure 5-3(e) and Figure 5-3(f), respectively.[55] Considering the conventional definition of the Brillion zone symmetric points (Γ, *X*, and *M)* in the *k*-space (inset of Figure 5-1(a)) and the incident angles (θ, Φ), the normalized frequency (*a*/ λ) can be related to the normalized momentum $k_{\Gamma - X}$ in the dispersion plot as $k_{\Gamma - X}$ = (*a*/ λ) sin θ cos Φ, following a similar procedure reported earlier [142]. The identified Fano resonant modes from Figure 5-3(c,d) are then mapped onto the dispersion plots, shown as the disconnected symbols, corresponding to the resonance spectral locations under different incident angles. For the TE polarization, the dominant resonance mode I is relatively insensitive to the change of the incident angle within the range of 0 to 20^{0}, which is responsible for a wide reflection band around this resonance (Figure 5-3(c)). On the other hand, for the TM polarization, the dominant resonant mode I splits sharply into modes I-III with small changes in incident angles. This explains why the high reflection band at surface normal direction splits into two smaller reflection bands for higher incident angles (Figure 5-3(d)). For both polarizations, with the increase of the incident angles, more less dominant higher order modes moves into the reflection bands, which leads to drastic changes in reflection performances. With the control of the modal dispersion properties, the angle and polarization dependent reflection properties can be engineered for the desired applications [130].
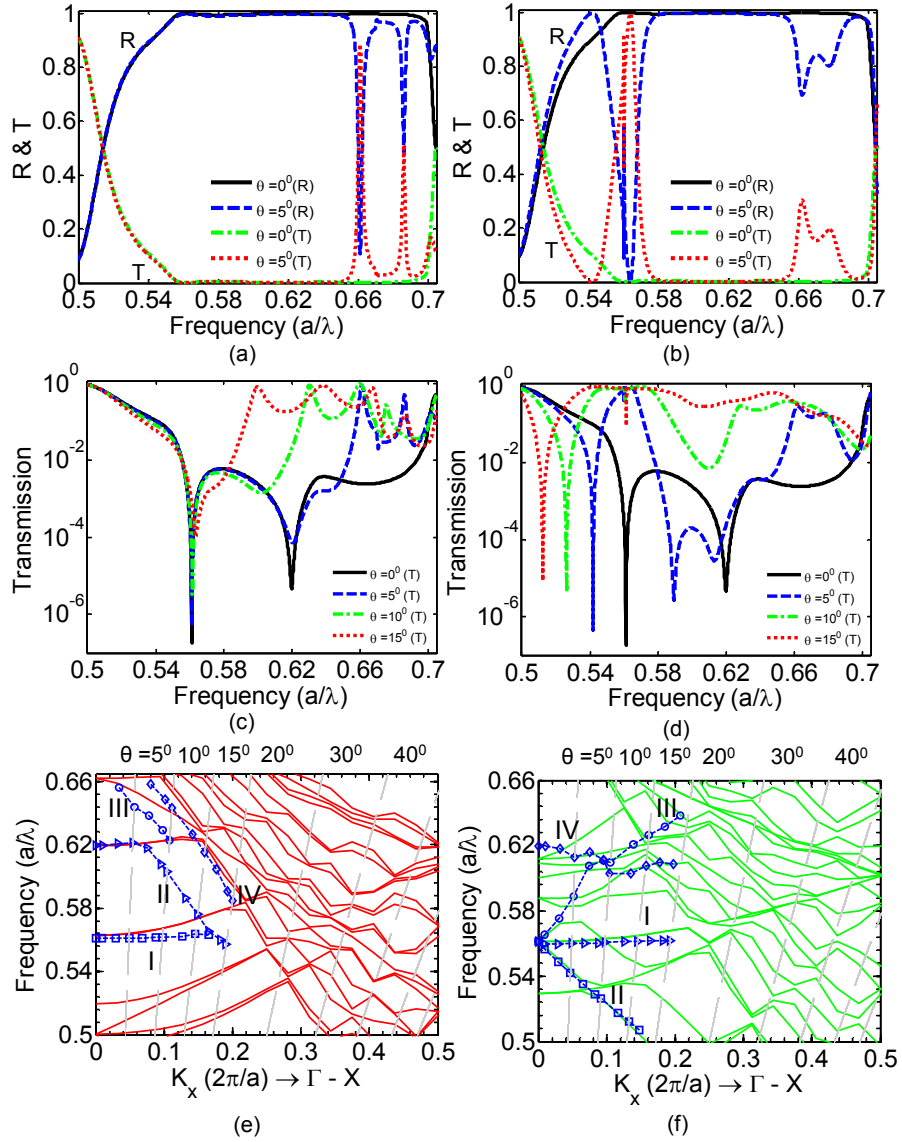
Figure 5-3: Simulated reflection and transmission on a linear scale for incident angles of θ =0⁰ and θ =5⁰ for (a) TE polarization and (b) TM polarization. Simulated transmission spectra showing locations of Fano resonances at various incident angles for (c) TE and (d) TM polarization. Simulated dispersion plots for even (red) and odd (green) guided modes along (Γ – X) direction for (e) TE and (f) TM polarized light. The different markers represent the Fano resonant modes for various incident angles. The straight dash gray lines represent the relationships between the normalized frequency and the normalized wave vectors along (Γ – X) direction. The bands labeled as I, II, III and IV correspond to different Fano resonant modes

5.5 Experimental Characterization of the Nanomembrane Reflector

The simulation results were validated by characterizing the fabricated MR. The MR was fabricated on SOI substrate, based on standard e-beam lithography patterning technique and plasma dry-etching processes [133, 134]. A broadband white light source is generated from a quartz tungsten halogen lamp that is collimated by a collimator. The beam is slightly focused (x4 lens) on the sample by the translational stage. The focused beam size is ~ 350 µm in diameter, much smaller than the 1 mm^2 patterned device area The reflected beam through the reflector was collected by the optical spectrum analyzer. The measured reflection spectrum was obtained by normalizing the measured reflection spectral intensity of the MR to that of the gold reference mirror. The polarization property was investigated by utilizing a Newport precision linear polarizer in our test set-up to control the incident beam polarization angle. For the surface normal incidence measurements, the polarizer was aligned along y – axis and x – axis for measuring TE and TM polarized light as shown in the schematic in Figure 5-1. The incident beam polarization was swept from $\Psi = 0^0$ to $\Psi = 90^0$ for both TE and TM polarized beam. For oblique incidence measurements, the reflector was mounted at an angle of 45^0 with reference to the surface normal on an angle dependent stage. The Φ angle was changed by rotating the sample in the x-y plane. Care was taken to measure the reflection spectra for the Si MR at the same location and under the same conditions.

5.5.1 Surface Normal Incidence

Shown in Figure 5-4(a) are the measured (denoted as "exp") and simulated (denoted as "sim") polarization dependent reflection spectra of the Si MR at surface normal incidence. The measured polarization independent reflection has a specular bandwidth of 180 nm (1400 nm – 1580 nm) - greater than 90%. The high symmetry of the

square lattice provides polarization independent broadband reflection for normal incidence, as seen in Figure 5-4(a) the reflection spectra for different polarization angle Ψ =0^0, 45^0, 90^0. Shown in Figure 5-4(b) are the measured and simulated reflection spectra for TE and TM polarized light incident at θ =45^0 (Φ =0^0) on the Si MR. The measured reflection spectra agree qualitatively with the simulated results for both surface normal and oblique incidence light on the Si MR. With the polarization along the x-axis (Figure 5-1(a)) of the lattice of the photonic crystal we see broadband reflection for TE polarization. We measured a 56 nm specular bandwidth for the TE polarization with reflectivity greater than 90%. A relatively low reflection is observed for the TM mode. An obvious question arises: what is the effect of incident plane azimuthal angle on the reflection of the Si MR.
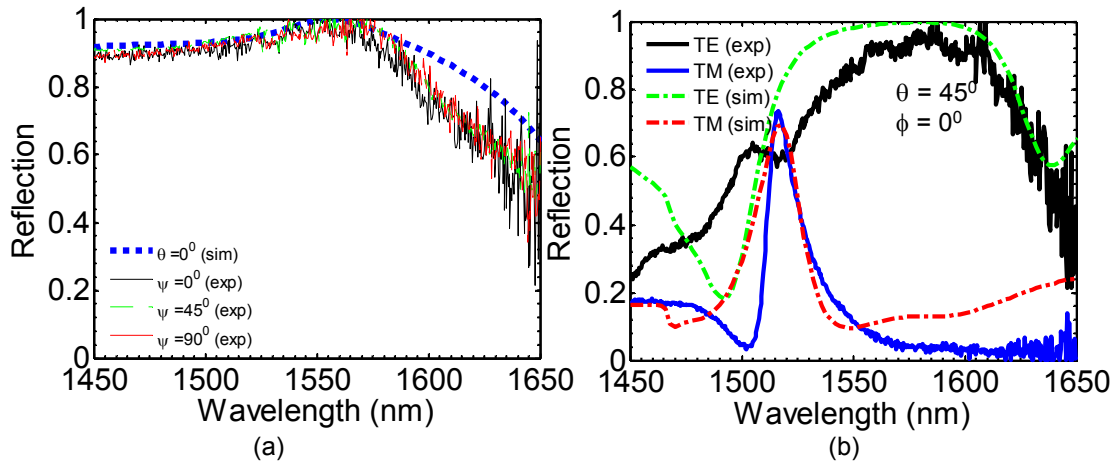
Figure 5-4: (a) Simulated ("sim") and measured ("exp") reflection spectra at normal incidence (θ =0^0) for various polarization (ψ) angles; and (b) Simulated ("sim") and measured ("exp") reflection spectra for TE and TM polarized light incident at θ =45^0 (Φ = 0^0).

5.5.2 Incident Beam Plane along (ΓX) Direction
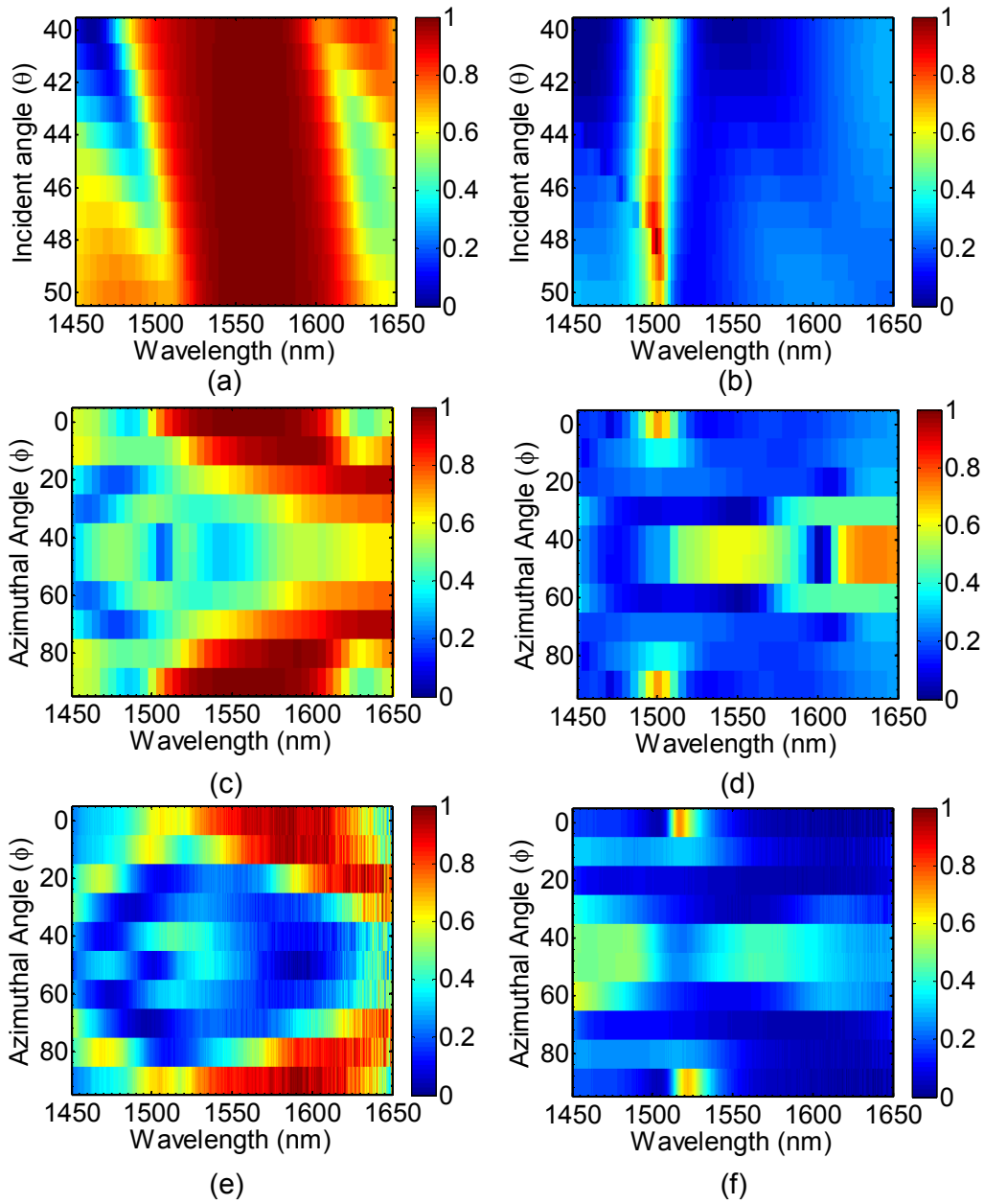
Figure 5-5: Contour plots of simulated reflectivity of TM (a) and TE (b) polarized light for a small range of incident angles close to an oblique incidence of θ =45^0. Contour plots of simulated (c, d) and measured (e, f) reflectivity of the incident plane azimuthal angle Φ (given in degrees) for TE (c, e) and TM (d, f) polarized light incident at 45^0.

Figure 5-5(a,b) show relatively less variation in the simulated reflection of the Si MR for both the TE and TM polarization for a range of angles close an oblique incidence (θ) of 45^0 (Φ=0). In other words, the testing of the mirror at an oblique incidence of 45^0 is quite tolerant to small incident angle misalignments. With the incident angle θ of 45^0, the impact of the incident plane azimuthal angle (Φ) was investigated. The simulated and measured reflection contour plots are shown in Figure 5-5. At an oblique incidence, the symmetry of the square lattice is broken as seen by the TE and TM polarizations. As a result, the non-degenerate modes at Γ – point begin to become coupled to the incident radiation for increased incident angles [143]. A high degree of symmetry of the square lattice gives a symmetric response when the in-plane polarization angle changes from 0^0 to 90^0 for both the TE and TM polarizations. This symmetric response is verified experimentally for both the TE and TM polarizations.

Table 5.2: Simulated reflection characteristics of Si MR for different polarization angles for TE polarization incident at 45^0.

Incident plane	Spectral range (nm)			Bandwidth (nm)		
	R > 90%	R > 95%	R > 99%	R > 90%	R > 95%	R > 99%
0^0	1516 – 1602	1523 – 1595	1542 – 1580	86	72	38
10^0	1550 – 1611	1565 – 1606	–	61	51	–
15^0	1580 – 1618	1598 – 1614	–	38	16	–
20^0	1612 – 1664	1648 – 1654	–	52	6	–
30^0	1696 – 1706	–	–	10	–	–
40^0	1782 – 1801	1788 – 1793	–	19	5	–
45^0	1755 – 1795	1760 – 1787	1766 – 1778	40	27	12

Table 5.2 summarizes the simulated TE polarization reflection characteristics of Si MR for different incident plane azimuthal angle incident at 45^0. For TE polarization, this device remarkably achieves reflection (R > 90%) in an 86 nm wide band for light incident at 45^0. When the incident plane is misaligned with reference to the one of the primary axis the reflection band shifts and reflectivity reduces. It is interesting to note that despite the azimuthal misalignment of the incident plane, this reflector still reflects TE polarization with reflectivity greater than 90% for 1580 nm – 1602 nm spectrum with a 15^0 angular bandwidth. The angular tolerance can be increased at the expense of reduced bandwidth. An incident plane azimuthal misalignment shifts the spectral position of the reflection band and simultaneously reduces reflection at oblique incidence. The simulated bandwidth for the TE polarization changes from 86 nm to 40 nm when the incident plane azimuthal angle changes from 0^0 to 45^0.

The Si MR gives high reflectivity at both surface normal and oblique angle incidences. A simulated 104 nm polarization independent specular bandwidth with reflection greater than 95% is easily achieved by the Si MR at surface normal incidence. We measured a specular bandwidth of 180 nm and 56 nm for the TE polarization at surface normal and oblique incidence of 45^0 respectively with reflection greater than 90%. The incident plane misalignment shifts the spectral position of the reflection band and simultaneously reduces reflection at oblique incidence. The experimental spectrum approximates the theoretical spectral response of this Si MR. The simulated specular bandwidth of the designed reflector is 86 nm and the measured bandwidth was found to be 56 nm for the TE polarization. For oblique incidence at 45^0, the reflector provides greater than 90% reflection with a 30^0 incident plane angular tolerance and a 22 nm bandwidth for the TE polarization. The presence of the misalignment limits the use of the reflector where special spectral and polarization filtering is required. All the results can

74

be helpful for such kind of reflectors into a wide range of photonic applications such as lasers, polarization dependent filters, optical interconnects, hollow core waveguides, beam splitters, coupled cavity systems etc.

Chapter 6

Integrated Grating Reflector and Coupler

6.1 Background

In order to account for continuous wave single wavelength emission with lower power consumption attention has shifted towards dual direction emission from the vertical surface cavity emission laser. In the so called hybrid laser structure, the partially reflecting mirror acts as an in-plane coupling element as well. The coupled light can be amplified or modulated in a slow light amplifier or in an electro-optic modulator. With the miniaturization of photonic devices, as the size of the reflector is reduced, the typical diffraction analysis considering the plane wave incidence on infinitely long grating breaks down. For surface normal incidence, the finite size of gratings, finite size incident beams and finite lateral extent of the grating, the angular components in addition the zero degree leads to scattering losses. This has a profound effect on the reflection. None the less, by placing a high index material waveguide, we can capture the unwanted scattering losses to a useful in-plane coupling light. In the following section, we investigate the effect of the finite size grating and the Gaussian beams on the reflection and in-plane coupling.

6.2 Design and Simulation

The schematic of the grating reflector is show in Figure 6-1(a). The 1D grating lies on top of the device silicon waveguide of the silicon-on-insulator substrate. The grating period (Λ), thickness (t_g), fill factor (FF) and the number of grating elements (N) control the reflection, in – plane coupling and scattering losses of the light. We use finite difference time domain (FDTD) technique to analyze the electromagnetic response of the grating reflector [77]. A Gaussian beam with the size equal to the reflector size

76

propagates in the z- direction unless otherwise stated. The coupled light propagates perpendicular to the incoming light in both the +x and –x direction as shown in the schematic. Perfectly matched layers (PMLs) were incorporated at the boundaries of the computational domain to avoid unnecessary reflections of light at the boundaries. The simulations presented below are designed for a transverse electric (TE) mode surface normal vertical to in-plane coupler. The electric field is aligned along the gratings. The reflector consists of a thin 340 nm silicon grating with 1 µm buried oxide layer. The grating period (Λ) and width (w) are 960 nm and 528 nm respectively.
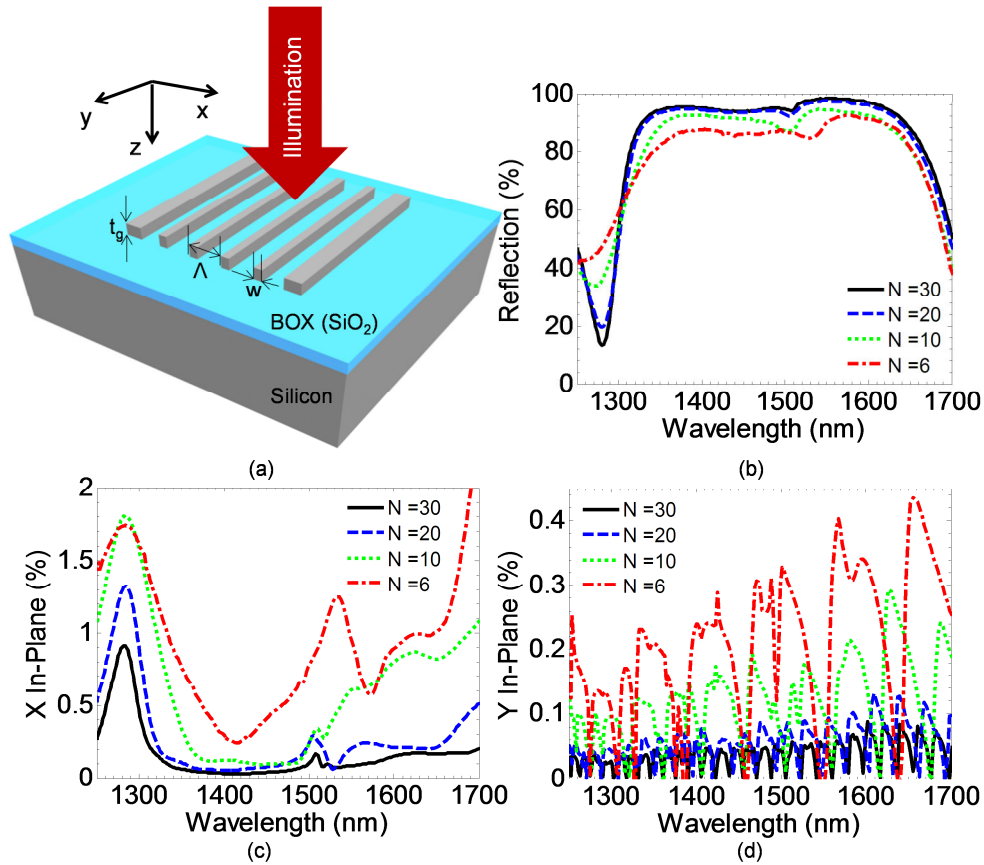
Figure 6-1: (a) Schematic of the grating reflector based on silicon-on-insulator substrate, where Λ, w, and t_g are the grating period, width and height respectively. Simulated (b) reflection and the single side scattering (c) parallel to and (d) perpendicular to the grating direction for the reflector with different sizes

The length of the grating is equal to the product of the number of grating elements and the lattice period. A grating reflector (GR) can be viewed as a combination of a homogeneous slab and an optical resonator. When the incoming light strikes the surface of the reflector, the light is reflected, transmitted and coupled into the in-plane propagating modes. The in-plane propagating modes reaching the boundary of the reflector see a discontinuous transition of the guided modes to a homogeneous slab supporting fully guided modes and results in scattering. When the Gaussian beam is small, the beam divergence increases [144]. The relatively large angles of incidence components of the plane-waves are not fully reflected from the structure, thus resulting in lower reflectivity (Figure 6-1(b)). When the number of grating periods is more than twenty, the angular divergence of the Gaussian beam is less than the angular full width and half maximum of the reflector. Consequently, the majority of the energy from the plane wave lies within the reflective region of the grating and the finite extent of the beam has minimal effect. The grating vector provides the phase matching condition in the direction of grating as a result; we see more coupling in the x-direction as compared to the y – direction. From the study of the field distribution of the modes, it is seen that the mode bounces along the y – direction as well yielding a Fabry – Perot like oscillation as shown in Figure 6-1(d). When the grating size is reduced, the scattering in the y – direction is comparable to the scattering in x – direction. The otherwise useless scattered light can be guided by a high index waveguide. This captured light can utilized for a variety of applications like diagnostic application within a photonic chip or serve an alternating path for light emission for VSCELs to name few.
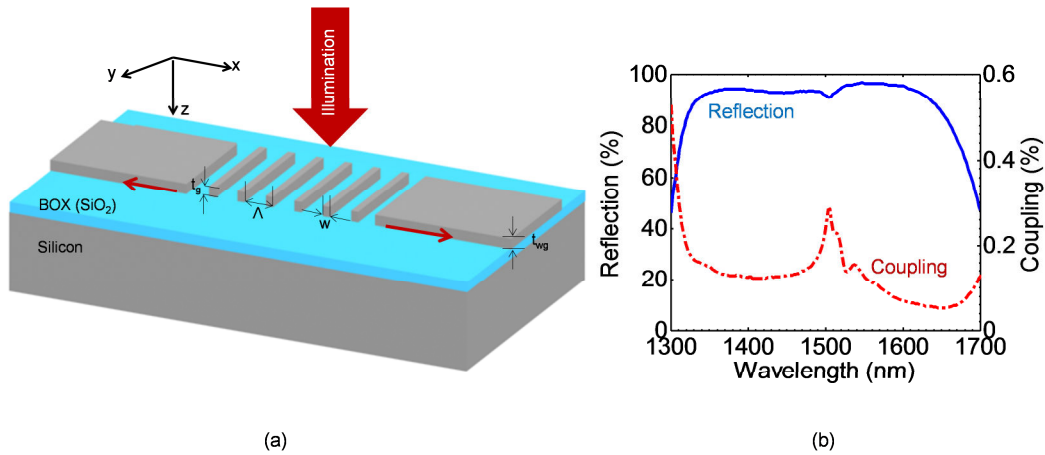
Figure 6-2: (a) Schematic of the grating reflector based on silicon-on-insulator substrate, where Λ, w, and t_g are the grating period, width and height respectively. The waveguide thickness is denoted by t_{wg}. (b) Simulated surface normal reflection and single side in-plane coupling for a grating reflector with grating period (Λ), width (w) and thickness of 960 nm, 528 nm and 340 nm respectively.

The high index waveguide confines the otherwise scattered leaky modes at abrupt discontinuity of the standalone reflector. Figure 6-2(a) shows a schematic of the grating reflector to serve as both a reflector and an in – plane coupler. The number of grating element was set to 20 and the length of the grating was chosen to be 20 periods. Shown in Figure 6-2(b) is the simulated surface normal reflection and single side in-plane coupling for a grating reflector. A maximum of 96.7% reflection with 0.13% in plane – coupling into the waveguide is achieved at 1550 nm wavelength. Negligible light scatters along y – direction. For the same 20 period grating reflector, when the size of the beam spot is reduced to 10 periods, a maximum in – plane coupling of 0.3% and high reflection of 96.1% is possible with the beam spot is close to the edge of the grating reflector at 1553 nm. Around 92% reflection is achieved with only six grating periods. Our investigation reveals that as the grating reflector size shrinks, the mirror losses increase and the reflectivity reduces.
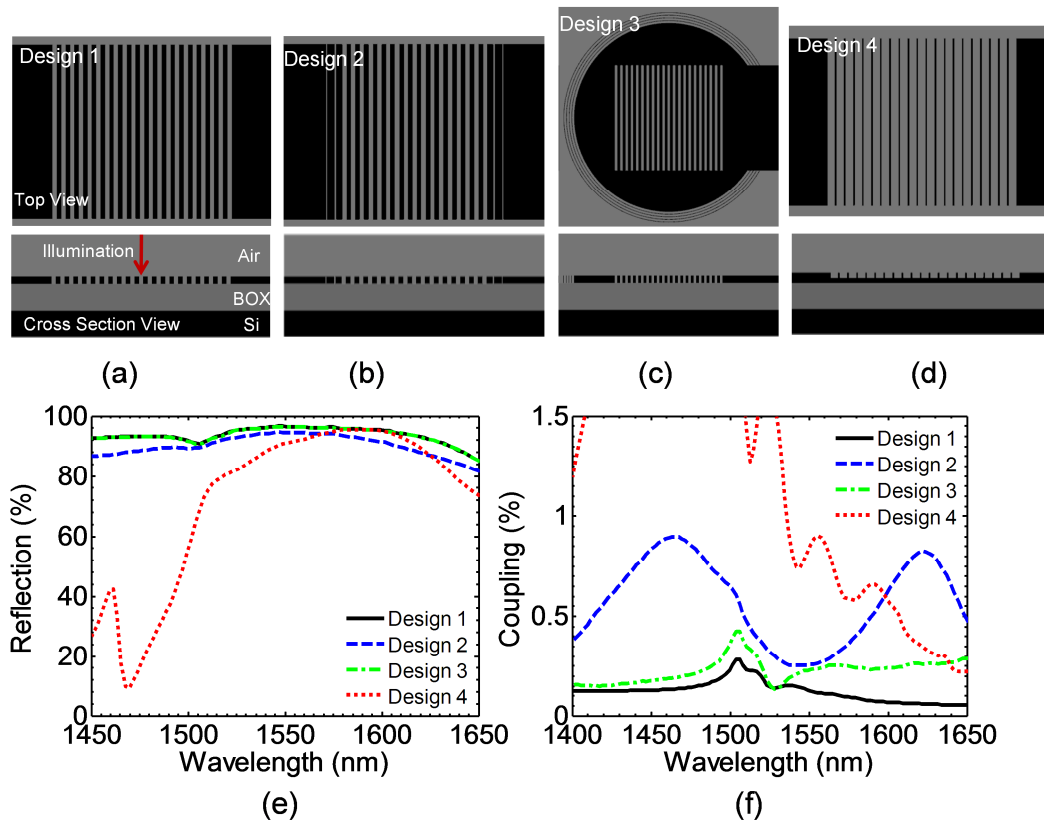
Figure 6-3: Top view and cross section view of the simulation schematic of the completely etched reflector (a) without and (b) line defect; (c) circular distributed Bragg reflector surrounding a defect free completely etched reflector and (d) partially etched grating with distributed Bragg reflector on one side of the reflector. Simulated (e) reflection and (f) single side coupling efficiency for the four different grating reflector designs.

In the quest for achieving high reflection and in – plane coupling simultaneously we invested different grating reflector designs as shown in Figure 6-3. For all the designs 20 grating elements are assumed. The length of the grating is fixed to number of grating elements times the period of the grating. The grating period, width and thickness are 960 nm, 528 nm and 340 nm respectively for designs 1 through 3. In design 2 (Figure 6-3(b)), two line defects were introduced at either ends of the reflector to couple more in-plane

80

guided mode into the waveguide. Design 3 (Figure 6-3(c)) involved the use of the four pair circular distributed Bragg reflector to provide uni-directional coupling and reduce the losses in along the y – direction.

Table 6.1: Simulated reflection characteristics of Si MR for different polarization angles for TE polarization incident at 45^0.

	Design 1	Design 2	Design 3	Design 4
Grating Period (Λ)	960 nm	960 nm	960 nm	980 nm
Fill Factor (FF)	0.55	0.55	0.55	0.2
Grating thickness (t_g)	340 nm	340 nm	340 nm	234 nm
Waveguide thickness (t_{wg})	340 nm	340 nm	340 nm	464 nm
Number of Grating elements(N)	20	20	20	20
Size of the Beam spot	20Λ	20Λ	20Λ	20Λ
Uni-direction (Uni) or Bi-direction (Bi) Output	Bi	Bi	Uni	Uni
Wavelength at maximum reflection (λ_{max})	1550 nm	1550 nm	1550 nm	1594 nm
Maximum Reflection (R_{max}) at λ_{max}	96.5%	94.5%	96.5%	96.4%
Maximum coupling (C_{max}) at λ_{max}	0.13%	0.26%	0.25%	0.5%

Finally in design 4 (Figure 6-3(d)) we utilize a higher order grating, which allows us to adjust the power into the higher order diffracted modes, thus enabling increased in – plane coupling. The four pair circular distributed Bragg reflector facilitates uni-

directional coupling. Table 5.2 summarizes the relevant grating design parameters and the maximum achievable reflection and corresponding single side in – plane coupling for the different grating reflector designs (as shown in Figure 6-3 (a – d)). The simulated spectral reflection and single side coupling for the different designs of the reflector is shown in   Figure 6-3(e) and Figure 6-3(f) respectively. Using Design 4 we can simultaneously achieve high reflection of 96.4% and an in – plane coupling of 0.5%. With the optimization of the grating parameters and the spacing between the grating reflector and the distributed Bragg reflector, we believe it is possible to further increase both the reflection and the in-plane coupling while minimizing the scattering losses and unwanted transmission to the substrate.

<div align="center">6.3 Measurements</div>

Using standard electron beam lithography and reactive ion etching (RIE) dry etch technique, the grating reflectors were fabricated on 340 nm silicon – on – insular substrate with 1 µm buried oxide. The period, width, thickness and length of the grating was 960 nm, 528 nm 340 nm and 400 µm respectively. A linear taper of 2 mm length was used to reduce the waveguide size from 400 µm to 10 µm as shown in Figure 6-4(a). The in-plane coupling and reflection were characterized by measuring the in-coupled and the reflected light spectra with an Agilent tunable laser system with 1pm resolution. The in – plane coupling efficiency was measured using the cut back method.   The light was incident on the grating from top and the coupled power was measured at the cleaved facet using a power meter. Reflection was measured by normalizing the power reflected from the grating reflector to a standard reference gold mirror. The incident beam goes through an optical circulator, a laser beam collimator, an optical lens, a linear polarizer and an objective lens. The x10 objective lens with numerical aperture (NA) of 0.43 was

used to reduce the spot size to 40 μm. The circulator was used to ensure surface normal incidence. An infrared camera was used for initial alignment.
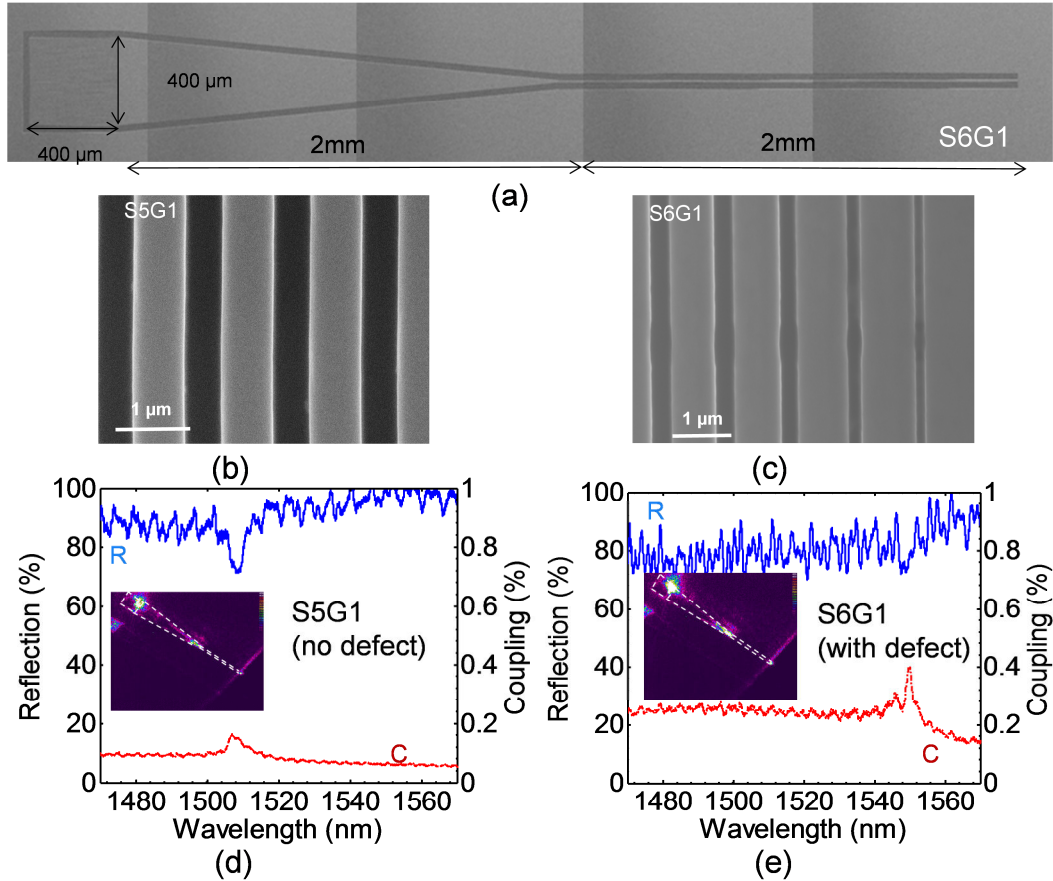
Figure 6-4: Scanning electron micrograph (a) stitched together to show the entire fabricated grating reflector; zoom – in section of the grating reflector (b) without defect and (c) with defect. Measured reflection and single side in-plane coupling for the grating coupler (d) without defect and (e) with defect. The inset shows the in-plane coupled light at the edge of the cleaved facet. The white dash line outlines the grating coupler, linear taper and the output waveguide section.

The fabricated grating reflectors have a grating period and thickness of 960 nm and 340 nm respectively. The FF of the reflector with and without any line defects are 0.69 and 0.55 respectively. The two line defects have fill factor of 0.85 and 0.79. Figure

6-4 (d) and Figure 6-4(e) show the measured reflection and the in-plane light coupling for the grating reflectors without and with line defects. The guided mode resonance shifts from 1510 nm to 1550 nm due to increased fill factor for the reflector with defect. At the guided mode resonance, maximum in – plane coupling of 0.2% and 0.4% is measured for the reflectors without and with line defects. However, the increase in the in-plane coupling is accompanied by the drop in the reflection. Almost 100% reflection with 0.06% in – plane coupling is measured with the reflector without any defects at wavelengths away from the guided mode resonance. The reflection drops to 95% whereas the in – plane coupling increases to 0.17% in the presence of the defects at wavelengths away from the guided mode resonance. The measured in-plane coupling does not account for any waveguide scattering loss or the Fresnel loss from the cleaved facet. Thus the actual coupling efficiency is expected to be slightly greater than the measured in-plane coupling.

Chapter 7

Concluding Remarks and Future Research

7.1 Conclusions

In this thesis, various kinds of photonic and optoelectronic devices are presented. Enhanced absorption from nanomembranes to atomic monolayers, surface normal vertical to in-plane coupling, near perfect anti-reflection coatings and high performance membrane reflectors are demonstrated with the incorporation of the micro- and nano-scale structures for out-of-plane light coupling and absorption for high performance solar cells and photodetectors, with maximum absorption in the functional layer and minimal front-surface reflection and minimal rear-surface transmission. The thesis presents an extensive numerical modeling, as well as experimental process and device characterizations.

Enhanced absorption from ultra-thin nanomembrane is demonstrated both numerically and experimentally by the incorporation of Fano resonant photonic crystal filters. Specifically, when the leakage rate of the guided mode from the resonant filter is made equal to the absorption rate of the absorbing medium, perfect absorption occurs. We numerically demonstrate near perfect absorption from atomic monolayers from two dimensional materials like graphene and molybdenum disulphide at infrared and visible wavelengths. Absorption enhanced spectrally selective photodetector on glass substrate is demonstrated experimentally from stacked InGaAs nanomembrane and silicon Fano resonant nanomembrane filter based on transfer printing technique.

Upon exploring the higher order gratings and optimizing of the power in the higher order diffracted modes, an efficient surface normal grating coupler is designed. The fourth order grating couplers can couple light from air into the waveguide or from waveguide into the air with high coupling efficiency. Unidirectional coupling is also

possible with the incorporation of the distributed Bragg reflector. The fourth order grating coupler couples 88% of the surface normal incident light at 1,535 nm from surface normal to in-plane waveguide with 3 dB bandwidth of 42 nm. We experimentally demonstrated 20% single side coupling efficiency with 3 dB bandwidth of 52 nm. With the optimization of the thickness of the buried oxide, incorporation of bottom reflector, anti-reflection coating, it is possible to achieve perfect light coupling. The fourth order coupler can be easily implemented on a standard SOI wafer as compared to more demanding second order grating coupler design parameters. The larger periods of the fourth order grating also facilitates the use of deep UV lithography as compared to more expensive and time consuming electron beam lithography for the smaller design parameters of the first order grating coupler.

Omni-directional antireflection coatings were designed for efficiency enhanced solar cells and high transmission for ophthalmic lenses. Omni-AR coating based on a micro scale inverted pyramid surface texture was experimentally realized on commercially available large area flexible solar cells via nanoimprint process. The surface texture reduces reflection, effectively traps light, increases the short circuit current density and hence increases the cell efficiency. The coupling increases by 22% at oblique incidence of 60^0. A design methodology was developed upon comparing the rate of change of the refractive index of a nanostructure to an effective graded index (GRIN) film to achieve near perfect transmission. Different shape of nanostructures was investigated to serve as near perfect antireflection coating. Numerical models were also built to study the non-uniform deposition of the GRIN film on flexible and rigid substrates based on Resonant infrared, matrix-assisted pulsed laser evaporation (RIR-MAPLE) technology. Near perfect transmission from polycarbonate substrate over a broad

wavelength spectrum and wide range of incident aangles were demonstrated numerically.

Finally, the angular and polarization properties of a membrane reflector based on guided mode resonance (GMR) are investigated thoroughly. The silicon membrane reflector (Si MR) gives high reflectivity at both surface normal and oblique angle incidences. Polarization independent reflection was obtained at surface normal direction. High reflection can also be obtained for one transverse electric (TE) polarization state over a wide range of incident angles. The incident plane misalignment shifts the spectral position of the reflection band and simultaneously reduces reflection at oblique incidence. The experimental spectrum approximates the theoretical spectral response of this Si MR.

7.2 Suggestions and Future Research

7.2.1 Perfect Absorption

A simple cost effective mechanical exfoliation technique shows the potential of integrating the novel two dimensional materials [63, 64]. While we have focused our work on the numerically modeling the near perfect absorption at surface normal incidence, the impact of oblique incidence needs to be investigated. Additionally, by further optimization, it might be possible to design a relatively broad band near perfect absorber. Corresponding experimental demonstration will further support the feasibility of the critically coupled enhanced absorption scheme for communication, imaging and energy harvesting applications.

7.2.2 Integrated Grating Reflector and Coupler

The grating couplers are used extensively for coupling light from the fibre into and out of the photonic circuit. For surface normal coupling, the power in the higher

diffracted orders is responsible for the in-plane coupling. A variety of grating parameters like grating period, width, height, number of elements, refractive index of the surrounding medium and waveguide thickness determine the power in the diffracted order. An optimization technique could be developed for designing higher order grating couplers by considering the design parameters for broadband high efficiency surface normal coupling. The higher order couplers allow the use of photolithography over more expensive electron beam lithography with larger fabrication tolerances thereby making the photonic circuits cheaper.

There also exists a need for uni-direction coupling in the integrated photonic circuits. The spacing between the in-plane reflector and the grating elements plays a crucial role in providing the uni-direction coupling of the incident light to the waveguide. An efficient optimization method needs to be developed for designing the uni-directional coupling structures.

Appendix A

List Of Publications

Journal Publications

1. W. Zhou, D. Zhao, Y.-C. Shuai, H. Yang, S. Chuwongin, **A. S. Chadha**, J.-H. Seo, K. X. Wang, V. Liu, Z. Ma, and S. Fan, "Progress in 2D photonic crystal Fano resonance photonics," Progress in Quantum Electronics, vol. 38, pp. 1-74, 2014.

2. Y. Shuai, D. Zhao, **A. S. Chadha**, J.-H. Seo, H. Yang, S. Fan, Z. Ma, and W. Zhou, "Coupled double-layer Fano resonance photonic crystal filters with lattice-displacement," *Applied Physics Letters,* vol. 103, p. 241106, 2013.

3. **A. S. Chadha**, D. Zhao, S. Chuwongin, Z. Ma, and W. Zhou, "Polarization- and angle-dependent characteristics in two dimensional photonic crystal membrane reflectors," *Applied Physics Letters,* vol. 103, p. 211107, 2013.

4. R. D. McCormick, E. D. Cline, **A. S. Chadha**, W. Zhou, and A. D. Stiff-Roberts, "Tuning the Refractive Index of Homopolymer Blends by Controlling Nanoscale Domain Size via RIR-MAPLE Deposition," *Macromolecular Chemistry and Physics,* vol. 214, pp. 2643–2650, 2013.

5. J. Wang, Y.-J. Lee, **A. S. Chadha**, J. Yi, M. L. Jespersen, J. J. Kelley, H. M. Nguyen, M. Nimmo, A. V. Malko, and R. A. Vaia, "Effect of Plasmonic Au Nanoparticles on Inverted Organic Solar Cell Performance," *The Journal of Physical Chemistry C,* vol. 117, pp. 85-91, 2012.

Conference Proceedings

6. **A. S. Chadha**, D. Zhao, and W. Zhou, "An all-dielectric broadband high-transmission efficiency circular polarizer," in *SPIE OPTO*, 2014, pp. 89941M-89941M-8.

7. **A. S. Chadha,** Y. Shuai, and W. Zhou, "High-order grating coupler for high-efficiency vertical to in-plane coupling," in *SPIE OPTO*, 2014, pp. 89950W-89950W-6.

8. **A. S. Chadha**, W. Zhou, and E. D. Cline, "Design criteria to optimize the near perfect anti-reflection coating," in *Photovoltaic Specialists Conference (PVSC), 2012 38th IEEE*, 2012, pp. 002521-002523.

9. **A. S. Chadha**, E. D. Cline, M. Tao, and W. Zhou, "Large area imprinted surface textures for omnidirectional conformal AR coatings on flexible amorphous silicon solar cells," in *Photovoltaic Specialists Conference (PVSC), 2012 38th IEEE*, 2012, pp. 000327-000330.

10. R. D. McCormick, E. D. Cline, **A. S. Chadha**, W. Zhou, and A. D. Stiff-Roberts, "Tuning the refractive index of blended polymer films by RIR-MAPLE deposition," in *SPIE OPTO*, 2012, pp. 825806-825806-6.

11. **A. S. Chadha**, W. Yang, T. K. Saha, S. Chuwongin, Y. Shuai, W. Zhou, Z. Ma, and G. J. Brown, "Spectral selective absorption enhancement from stacked ultra-thin InGaAs/Si Fano resonance membranes," in *SPIE OPTO*, 2012, pp. 82680G-82680G-7

References

[1]   B. J. Walker, G. P. Nair, L. F. Marshall, V. Bulović, and M. G. Bawendi, "Narrow-Band Absorption-Enhanced Quantum Dot/J-Aggregate Conjugates," *Journal of the American Chemical Society,* vol. 131, pp. 9624-9625, 2009/07/22 2009.

[2]   F. Wang, G. Dukovic, L. E. Brus, and T. F. Heinz, "The optical resonances in carbon nanotubes arise from excitons," *Science,* vol. 308, pp. 838-841, 2005.

[3]   K. F. Mak, C. Lee, J. Hone, J. Shan, and T. F. Heinz, "Atomically thin MoS 2: a new direct-gap semiconductor," *Physical Review Letters,* vol. 105, p. 136805, 2010.

[4]   H. Liu, A. T. Neal, Z. Zhu, D. Tománek, and P. D. Ye, "Phosphorene: A New 2D Material with High Carrier Mobility," *arXiv preprint arXiv:1401.4133,* 2014.

[5]   E. S. Reich, "Phosphorene excites materials scientists," *Nature,* vol. 506, pp. 19-19, 2014.

[6]   X. Wang, L. Zhi, and K. Müllen, "Transparent, Conductive Graphene Electrodes for Dye-Sensitized Solar Cells," *Nano Letters,* vol. 8, pp. 323-327, 2008/01/01 2007.

[7]   K. S. Kim, Y. Zhao, H. Jang, S. Y. Lee, J. M. Kim, K. S. Kim, J.-H. Ahn, P. Kim, J.-Y. Choi, and B. H. Hong, "Large-scale pattern growth of graphene films for stretchable transparent electrodes," *Nature,* vol. 457, pp. 706-710, 2009.

[8]   H.-Z. Geng, K. K. Kim, K. P. So, Y. S. Lee, Y. Chang, and Y. H. Lee, "Effect of Acid Treatment on Carbon Nanotube-Based Flexible Transparent Conducting Films," *Journal of the American Chemical Society,* vol. 129, pp. 7758-7759, 2007/06/01 2007.

[9]   P. Matyba, H. Yamaguchi, G. Eda, M. Chhowalla, L. Edman, and N. D. Robinson, "Graphene and Mobile Ions: The Key to All-Plastic, Solution-Processed Light-Emitting Devices," *ACS Nano,* vol. 4, pp. 637-642, 2010/02/23 2010.

[10]   T. Mueller, F. Xia, and P. Avouris, "Graphene photodetectors for high-speed optical communications," *Nat Photon,* vol. 4, pp. 297-301, 2010.

[11]   S. Bae, H. Kim, Y. Lee, X. Xu, J.-S. Park, Y. Zheng, J. Balakrishnan, T. Lei, H. Ri Kim, Y. I. Song, Y.-J. Kim, K. S. Kim, B. Ozyilmaz, J.-H. Ahn, B. H. Hong, and S. Iijima, "Roll-to-roll production of 30-inch graphene films for transparent electrodes," *Nat Nano,* vol. 5, pp. 574-578, 2010.

[12]   C. D. Sheraw, L. Zhou, J. R. Huang, D. J. Gundlach, T. N. Jackson, M. G. Kane, I. G. Hill, M. S. Hammond, J. Campi, B. K. Greening, J. Francl, and J. West, "Organic thin-film transistor-driven polymer-dispersed liquid crystal displays on flexible polymeric substrates," *Applied Physics Letters,* vol. 80, pp. 1088-1090, 2002.

[13]   J. Wang, Y. Hernandez, M. Lotya, J. N. Coleman, and W. J. Blau, "Broadband Nonlinear Optical Response of Graphene Dispersions," *Advanced Materials,* vol. 21, pp. 2430-2435, 2009.

[14]   F. Rana, "Graphene Terahertz Plasmon Oscillators," *Nanotechnology, IEEE Transactions on,* vol. 7, pp. 91-99, 2008.

[15]   S. A. Mikhailov, "Non-linear electromagnetic response of graphene," *EPL (Europhysics Letters),* vol. 79, p. 27002, 2007.

[16]   R. R. Nair, P. Blake, A. N. Grigorenko, K. S. Novoselov, T. J. Booth, T. Stauber, N. M. R. Peres, and A. K. Geim, "Fine Structure Constant Defines Visual Transparency of Graphene," *Science,* vol. 320, p. 1308, June 6, 2008 2008.

[17]   (2013). Available: http://www.slashgear.com/ibm-silicon-nanophotonics-speeds-servers-with-25gbps-light-10260108

[18]   A. Alduino, L. Liao, R. Jones, M. Morse, B. Kim, W.-Z. Lo, J. Basak, B. Koch, H.-F. Liu, H. Rong, M. Sysak, C. Krause, R. Saba, D. Lazar, L. Horwitz, R. Bar, S. Litski, A. Liu, K. Sullivan, O. Dosunmu, N. Na, T. Yin, F. Haubensack, I. w. Hsieh, J. Heck, R. Beatty, H. Park, J. Bovington, S. Lee, H. Nguyen, H. Au, K. Nguyen, P. Merani, M. Hakami, and M. Paniccia, "Demonstration of a High Speed 4-Channel Integrated Silicon Photonics WDM Link with Hybrid Silicon Lasers," in *Integrated Photonics Research, Silicon and Nanophotonics and Photonics in Switching*, Monterey, California, 2010, p. PDIWI5.

[19]   H. Park, A. W. Fang, S. Kodama, and J. E. Bowers, "Hybrid silicon evanescent laser fabricated with a silicon waveguide and III-V offset quantum well," *Optics Express,* vol. 13, pp. 9460-9464, 2005.

[20]   G. Roelkens, D. Van Thourhout, R. Baets, R. Notzel, and M. Smit, "Laser emission and photodetection in an InP/InGaAsP layer integrated on and coupled to a Silicon-on-Insulator waveguide circuit," *Optics Express,* vol. 14, pp. 8154-8159, 2006.

[21]   R. Crabb and F. Treble, "Thin silicon solar cells for large flexible arrays," *Nature,* vol. 213, pp. 1223 - 1224, 1967.

[22]   P. I. Hsu, R. Bhattacharya, H. Gleskova, M. Huang, Z. Xi, Z. Suo, S. Wagner, and J. C. Sturm, "Thin-film transistor circuits on large-area spherical surfaces," *Applied Physics Letters,* vol. 81, pp. 1723-1725, 2002.

[23]   K.-H. Kim, E.-Y. Jeon, B. W. Park, D. H. Song, J.-H. Lee, G. S. Lee, K.-C. Shin, H. S. Kim, and T.-H. Yoon, "Pixel electrode structure for high transmittance in a multi-domain vertical alignment liquid crystal display device," *Journal of Physics D: Applied Physics,* vol. 45, p. 065103, 2012.

[24]   M. Oh-e and K. Kondo, "Electro-optical characteristics and switching behavior of the in-plane switching mode," *Applied Physics Letters,* vol. 67, pp. 3895-3897, 1995.

[25]   C. Z. van Doorn, "Dynamic behavior of twisted nematic liquid-crystal layers in switched fields," *Journal of Applied Physics,* vol. 46, pp. 3738-3745, 1975.

[26]   S. R. Quake and A. Scherer, "From micro-to nanofabrication with soft materials," *Science,* vol. 290, pp. 1536-1540, 2000.

[27]   D.-H. Kim and J. A. Rogers, "Bend, buckle, and fold: mechanical engineering with nanomembranes," *ACS nano,* vol. 3, pp. 498-501, 2009.

[28]   H.-C. Yuan, J. Shin, G. Qin, L. Sun, P. Bhattacharya, M. G. Lagally, G. K. Celler, and Z. Ma, "Flexible photodetectors on plastic substrates by use of printing transferred single-crystal germanium membranes," *Applied Physics Letters,* vol. 94, pp. 013102-013102-3, 2009.

[29]   H.-C. Yuan, G. K. Celler, and Z. Ma, "7.8-GHz flexible thin-film transistors on a low-temperature plastic substrate," *Journal of Applied Physics,* vol. 102, pp. 034501-034501-4, 2007.

[30]   D.-H. Kim, J.-H. Ahn, W. M. Choi, H.-S. Kim, T.-H. Kim, J. Song, Y. Y. Huang, Z. Liu, C. Lu, and J. A. Rogers, "Stretchable and foldable silicon integrated circuits," *Science,* vol. 320, pp. 507-511, 2008.

[31]   S. John, "Strong localization of photons in certain disordered dielectric superlattices," *Physical Review Letters,* vol. 58, pp. 2486-2489, 1987.

[32]   E. Yablonovitch, "Inhibited spontaneous emission in solid-state physics and electronics," *Physical review letters,* vol. 58, p. 2059, 1987.

[33]   W. Zhou, Z. Ma, H. Yang, Z. Qiang, G. Qin, H. Pang, L. Chen, W. Yang, S. Chuwongin, and D. Zhao, "Flexible photonic-crystal Fano filters based on transferred

95

semiconductor nanomembranes," *Journal of Physics D: Applied Physics,* vol. 42, p. 234007, 2009.

[34]   K. Posani, V. Tripathi, S. Annamalai, N. Weisse-Bernstein, S. Krishna, R. Perahia, O. Crisafulli, and O. Painter, "Nanoscale quantum dot infrared sensors with photonic crystal cavity," *Applied physics letters,* vol. 88, pp. 151104-151104-3, 2006.

[35]   I. Choi and Y. Choi, "Plasmonic nanosensors: Review and prospect," *Selected Topics in Quantum Electronics, IEEE Journal of,* vol. 18, pp. 1110-1121, 2012.

[36]   X. Yong-Gang, W. Xin, H. Xin-Hua, L. Xiao-Han, and Z. Jian, "Modification of Absorption of a Bulk Material by Photonic Crystals," *Chinese Physics Letters,* vol. 19, p. 1819, 2002.

[37]   S. Lin, J. Fleming, Z. Li, I. El-Kady, R. Biswas, and K. M. Ho, "Origin of absorption enhancement in a tungsten, three-dimensional photonic crystal," *Journal of the Optical Society of America B,* vol. 20, pp. 1538-1541, 2003.

[38]   G. Veronis, R. W. Dutton, and S. Fan, "Metallic photonic crystals with strong broadband absorption at optical frequencies over wide angular range," *Journal of applied physics,* vol. 97, pp. 093104-093104-4, 2005.

[39]   J.-K. Yang, M.-K. Seo, I.-K. Hwang, S.-B. Kim, and Y.-H. Lee, "Polarization-selective resonant photonic crystal photodetector," *Applied Physics Letters,* vol. 93, pp. 211103-211103-3, 2008.

[40]   S. Fan and J. D. Joannopoulos, "Analysis of guided resonances in photonic crystal slabs," *Physical Review B,* vol. 65, p. 235112, 2002.

[41]   U. Fano, "Effects of configuration interaction on intensities and phase shifts," *Physical Review,* vol. 124, p. 1866, 1961.

[42]   K. C. Johnson, "Coupled scalar wave diffraction theory," *Applied Physics A: Materials Science & Processing,* vol. 24, pp. 249-260, 1981.

[43]   M. G. Moharam and T. K. Gaylord, "Rigorous coupled-wave analysis of planar-grating diffraction," *J. Opt. Soc. Am.,* vol. 71, pp. 811-818, 1981.

[44]   A. chadha, W. Yang, T. Saha, S. Chuwongin, Y. Shuai, W. Zhou, G. J. Brown, and Z. Ma, "Spectral selective absorption enhancement from stacked ultra-thin InGaAs/Si Fano resonance membranes " *Proceedings of SPIE,* vol. 8268, p. 8268G, 2012.

[45]   W. Zhou, Z. Qiang, L. Chen, H. Yang, and G. J. Brown, "Spectrally selective infrared absorption enhancement in photonic crystal cavities," pp. 709507-709507, 2008.

[46]   F. Bonaccorso, Z. Sun, T. Hasan, and A. Ferrari, "Graphene photonics and optoelectronics," *Nature Photonics,* vol. 4, pp. 611-622, 2010.

[47]   A. Kumar and P. K. Ahluwalia, "Tunable Electronic and Dielectric Properties of Molybdenum Disulfide," in *MoS2.* vol. 21, Z. M. Wang, Ed., ed: Springer International Publishing, 2014, pp. 53-76.

[48]   K. Kim, J.-Y. Choi, T. Kim, S.-H. Cho, and H.-J. Chung, "A role for graphene in silicon-based semiconductor devices," *Nature,* vol. 479, pp. 338-344, 2011.

[49]   M. Ramezani Masir, P. Vasilopoulos, and F. M. Peeters, "Fabry-Pérot resonances in graphene microstructures: Influence of a magnetic field," *Physical Review B,* vol. 82, p. 115417, 2010.

[50]   M. Furchi, A. Urich, A. Pospischil, G. Lilley, K. Unterrainer, H. Detz, P. Klang, A. M. Andrews, W. Schrenk, and G. Strasser, "Microcavity-integrated graphene photodetector," *Nano letters,* vol. 12, pp. 2773-2777, 2012.

[51]   M. M. Y. A. Alsaif, K. Latham, M. R. Field, D. D. Yao, N. V. Medehkar, G. A. Beane, R. B. Kaner, S. P. Russo, J. Z. Ou, and K. Kalantar-zadeh, "Tunable Plasmon

Resonances in Two-Dimensional Molybdenum Oxide Nanoflakes," *Advanced Materials,* pp. n/a-n/a, 2014.

[52]   L. Ju, B. Geng, J. Horng, C. Girit, M. Martin, Z. Hao, H. A. Bechtel, X. Liang, A. Zettl, Y. R. Shen, and F. Wang, "Graphene plasmonics for tunable terahertz metamaterials," *Nat Nano,* vol. 6, pp. 630-634, 2011.

[53]   G. Pirruccio, L. Martín Moreno, G. Lozano, and J. Gómez Rivas, "Coherent and Broadband Enhanced Optical Absorption in Graphene," *ACS Nano,* vol. 7, pp. 4810-4817, 2013/06/25 2013.

[54]   A. Yariv, "Critical coupling and its control in optical waveguide-ring resonator systems," *Photonics Technology Letters, IEEE,* vol. 14, pp. 483-485, 2002.

[55]   S. G. Johnson, S. Fan, P. R. Villeneuve, J. Joannopoulos, and L. Kolodziejski, "Guided modes in photonic crystal slabs," *Physical Review B,* vol. 60, p. 5751, 1999.

[56]   S. S. Wang, R. Magnusson, J. S. Bagby, and M. G. Moharam, "Guided-mode resonances in planar dielectric-layer diffraction gratings," *J. Opt. Soc. Am. A,* vol. 7, pp. 1470-1474, 1990.

[57]   S. Fan, W. Suh, and J. Joannopoulos, "Temporal coupled-mode theory for the Fano resonance in optical resonators," *JOSA A,* vol. 20, pp. 569-572, 2003.

[58]   W. Suh, W. Zheng, and F. Shanhui, "Temporal coupled-mode theory and the presence of non-orthogonal modes in lossless multimode cavities," *Quantum Electronics, IEEE Journal of,* vol. 40, pp. 1511-1518, 2004.

[59]   M. Bruna and S. Borini, "Optical constants of graphene layers in the visible range," *Applied Physics Letters,* vol. 94, pp. -, 2009.

[60]   Q. Bao, H. Zhang, Y. Wang, Z. Ni, Y. Yan, Z. X. Shen, K. P. Loh, and D. Y. Tang, "Atomic-Layer Graphene as a Saturable Absorber for Ultrafast Pulsed Lasers," *Advanced Functional Materials,* vol. 19, pp. 3077-3083, 2009.

[61]   A. Castellanos-Gomez, N. Agraït, and G. Rubio-Bollinger, "Optical identification of atomically thin dichalcogenide crystals," *Applied Physics Letters,* vol. 96, p. 213116, 2010.

[62]   T. Bååk, "Silicon oxynitride; a material for GRIN optics," *Applied Optics,* vol. 21, pp. 1069-1072, 1982/03/15 1982.

[63]   A. Reina, H. Son, L. Jiao, B. Fan, M. S. Dresselhaus, Z. Liu, and J. Kong, "Transferring and Identification of Single- and Few-Layer Graphene on Arbitrary Substrates," *The Journal of Physical Chemistry C,* vol. 112, pp. 17741-17744, 2008/11/20 2008.

[64]   A. Castellanos-Gomez, M. Poot, G. A. Steele, H. S. van der Zant, N. Agraït, and G. Rubio-Bollinger, "Elastic properties of freely suspended MoS2 nanosheets," *Advanced Materials,* vol. 24, pp. 772-775, 2012.

[65]   V. R. Almeida, R. R. Panepucci, and M. Lipson, "Nanotaper for compact mode conversion," *Opt. Lett.,* vol. 28, pp. 1302-1304, 2003.

[66]   M. Loncar, D. Nedeljkovic, T. Doll, J. Vuckovic, A. Scherer, and T. P. Pearsall, "Waveguiding in planar photonic crystals," *Applied Physics Letters,* vol. 77, pp. 1937-1939, 2000.

[67]   J. V. Galan, P. Sanchis, J. Blasco, and J. Martí, "Broadband and highly efficient grating couplers for silicon-based horizontal slot waveguides," *Proc. SPIE,* vol. 6996, pp. 69960Q1-9, 2008.

[68]   C. Gunn, "Fully Integrated VLSI CMOS and Photonics "CMOS Photonics"," in *IEEE Symposium on VLSI Technology*, 2007, pp. 6-9.

[69]   A. Narasimha and E. Yablonovitch, "Efficient optical coupling into single mode Silicon-on-Insulator thin films using a planar grating coupler embedded in a high index contrast dielectric stack," in *Conference on Lasers and Electro-Optics*, 2003, pp. 1074-1076.

[70]   S. Scheerlinck, J. Schrauwen, F. Van Laere, D. Taillaert, D. Van Thourhout, and R. Baets, "Efficient, broadband and compact metal grating couplers for silicon-on-insulator waveguides," *Opt. Express,* vol. 15, pp. 9625-9630, 2007.

[71]   F. Van Laere, W. Bogaerts, D. Taillaert, P. Dumon, D. Van Thourhout, and R. Baets, "Compact Focusing Grating Couplers Between Optical Fibers and Silicon-on-Insulator Photonic Wire Waveguides," in *Conference on Optical Fiber Communication and the National Fiber Optic Engineers*, 2007, pp. 1-3.

[72]   D. Taillaert, F. Van Laere, M. Ayre, W. Bogaerts, D. Van Thourhout, P. Bienstman, and R. Baets, "Grating couplers for coupling between optical fibers and nanophotonic waveguides," *Jpn. J. Appl. Phys,* vol. 45, pp. 6071–6077, 2006.

[73]   X. Chen, C. Li, and H. K. Tsang, "Characterization of silicon-on-insulator waveguide chirped grating for coupling to a vertical optical fiber," in *Conference on Optical MEMs and Nanophotonics* 2008, pp. 56-57.

[74]   L. Frederik Van, V. K. Maria, T. Dirk, T. Dries Van, F. K. Thomas, and B. Roel, "Compact Slanted Grating Couplers Between Optical Fiber and InP-InGaAsP Waveguides," *Photonics Technology Letters, IEEE,* vol. 19, pp. 396-398, 2007.

[75]   L. Zhu, V. Karagodsky, and C. Chang-Hasnain, "Novel high efficiency vertical to in-plane optical coupler," *Proc.SPIE,* vol. 8270, pp. 82700L-11, 2012.

[76]   D. Taillaert, F. Van Laere, M. Ayre, W. Bogaerts, D. Van Thourhout, P. Bienstman, and R. Baets, "Grating couplers for coupling between optical fibers and

nanophotonic waveguides," *Japanese Journal of Applied Physics Part 1-Regular Papers Brief Communications & Review Papers,* vol. 45, pp. 6071-6077, 2006.

[77]   A. F. Oskooi, D. Roundy, M. Ibanescu, P. Bermel, J. D. Joannopoulos, and S. G. Johnson, "Meep: A flexible free-software package for electromagnetic simulations by the FDTD method," *Computer Physics Communications,* vol. 181, pp. 687-702, 2010.

[78]   V. Karagodsky, F. G. Sedgwick, and C. J. Chang-Hasnain, "Theoretical analysis of subwavelength high contrast grating reflectors," *Opt. Express,* vol. 18, pp. 16973-16988, 2010.

[79]   R. Magnusson and S. S. Wang, "New principle for optical filters," *Applied Physics Letters,* vol. 61, pp. 1022-1024, 1992.

[80]   T. Tamir and S. Peng, "Analysis and design of grating couplers," *Applied Physics A: Materials Science & Processing,* vol. 14, pp. 235-254, 1977.

[81]   S. P. Pogossian, L. Vescan, and A. Vonsovici, "The Single-Mode Condition for Semiconductor Rib Waveguides with Large Cross Section," *J. Lightwave Technol.,* vol. 16, pp. 1851-1853, 1998.

[82]   C. F. R. Mateus, M. C. Y. Huang, D. Yunfei, A. R. Neureuther, and C. J. Chang-Hasnain, "Ultrabroadband mirror using low-index cladded subwavelength grating," *Photonics Technology Letters, IEEE,* vol. 16, pp. 518-520, 2004.

[83]   R. M. Emmons and D. G. Hall, "Buried-oxide silicon-on-insulator structures. II. Waveguide grating couplers," *IEEE Journal of Quantum Electronics,* vol. 28, pp. 164-175, 1992.

[84]   T. Suhara and H. Nishihara, "Integrated optics components and devices using periodic structures," *Quantum Electronics, IEEE Journal of,* vol. 22, pp. 845-867, 1986.

[85]   J. Q. Xi, M. F. Schubert, J. K. Kim, E. F. Schubert, M. Chen, S. Y. Lin, W. Liu, and J. A. Smart, "Optical thin-film materials with low refractive index for broadband elimination of Fresnel reflection," *Nature Photonics,* vol. 1, pp. 176-179, 2007.

[86]   W. Zhou, M. Tao, L. Chen, and H. Yang, "Microstructured surface design for omnidirectional antireflection coatings on solar cells," *Journal of Applied Physics,* vol. 102, p. 103105, 2007.

[87]   D. Bouhafs, A. Moussi, A. Chikouche, and J. M. Ruiz, "Design and simulation of antireflection coating systems for optoelectronic devices: Application to silicon solar cells," *Solar Energy Materials and Solar Cells,* vol. 52, pp. 79-93, 1998.

[88]   Z. Huang, H. Fang, and J. Zhu, "Fabrication of Silicon Nanowire Arrays with Controlled Diameter, Length, and Density," *Advanced Materials,* vol. 19, pp. 744-748, 2007.

[89]   S. R. Kennedy and M. J. Brett, "Porous Broadband Antireflection Coating by Glancing Angle Deposition," *Appl. Opt.,* vol. 42, pp. 4573-4579, 2003.

[90]   S. Koynov, M. S. Brandt, and M. Stutzmann, "Black nonreflecting silicon surfaces for solar cells," *Applied Physics Letters,* vol. 88, pp. 203107-3, 2006.

[91]   C. C. Striemer and P. M. Fauchet, "Dynamic etching of silicon for broadband antireflection applications," *Applied Physics Letters,* vol. 81, pp. 2980-2982, 2002.

[92]   L. Hyunwoo, L. Eunjoo, and L. Soohong, "Investigation of nano-porous silicon antireflection coatings for crystalline silicon solar cells," in *Nanotechnology Materials and Devices Conference, 2006. NMDC 2006. IEEE*, 2006, pp. 340-341.

[93]   F. Liu, B. Dong, and X. Liu, "Bio-Inspired Photonic Structures: Prototypes, Fabrications and Devices," *Optical Devices in Communication and Computation,* 2012.

[94]   H. K. Raut, V. A. Ganesh, A. S. Nair, and S. Ramakrishna, "Anti-reflective coatings: A critical, in-depth review," *Energy & Environmental Science,* vol. 4, pp. 3779-3804, 2011.

[95]   P. Vukusic and J. R. Sambles, "Photonic structures in biology," *Nature,* vol. 424, pp. 852-855, 2003.

[96]   P. Papet, O. Nichiporuk, A. Kaminski, Y. Rozier, J. Kraiem, J. F. Lelievre, A. Chaumartin, A. Fave, and M. Lemiti, "Pyramidal texturing of silicon solar cell with TMAH chemical anisotropic etching," *Solar Energy Materials and Solar Cells,* vol. 90, pp. 2319-2328, 2006.

[97]   D. H. Macdonald, A. Cuevas, M. J. Kerr, C. Samundsett, D. Ruby, S. Winderbaum, and A. Leo, "Texturing industrial multicrystalline silicon solar cells," *Solar Energy,* vol. 76, pp. 277-283, 2004.

[98]   M. Moreno, D. Daineka, and P. Roca i Cabarrocas, "Plasma texturing for silicon solar cells: From pyramids to inverted pyramids-like structures," *Solar Energy Materials and Solar Cells,* vol. 94, pp. 733-737, 2010.

[99]   A. Hauser, I. Melnyk, P. Fath, S. Narayanan, S. Roberts, and T. Bruton, "A simplified process for isotropic texturing of mc-Si," in *Photovoltaic Energy Conversion, 2003. Proceedings of 3rd World Conference on*, 2003, pp. 1447-1450.

[100]   Y. Inomata, K. Fukui, and K. Shirasawa, "Surface texturing of large area multicrystalline silicon solar cells using reactive ion etching method," *Solar energy materials and solar cells,* vol. 48, pp. 237-242, 1997.

[101]   H. Nakaya, M. Nishida, Y. Takeda, S. Moriuchi, T. Tonegawa, T. Machida, and T. Nunoi, "Polycrystalline silicon solar cells with V-grooved surface," *Solar energy materials and solar cells,* vol. 34, pp. 219-225, 1994.

[102]   M. Stocks, A. Carr, and A. Blakers, "Texturing of polycrystalline silicon," *Solar energy materials and solar cells,* vol. 40, pp. 33-42, 1996.

[103]   O. Kluth, B. Rech, L. Houben, S. Wieder, G. Schöpe, C. Beneking, H. Wagner, A. Löffl, and H. Schock, "Texture etched ZnO: Al coated glass substrates for silicon based thin film solar cells," *Thin Solid Films,* vol. 351, pp. 247-253, 1999.

[104]   M. Abbott and J. Cotter, "Optical and electrical properties of laser texturing for high-efficiency solar cells," *Progress in Photovoltaics: Research and Applications,* vol. 14, pp. 225-235, 2006.

[105]   Q. Chen, G. Hubbard, P. A. Shields, C. Liu, D. W. E. Allsopp, W. N. Wang, and S. Abbott, "Broadband moth-eye antireflection coatings fabricated by low-cost nanoimprinting," *Applied Physics Letters,* vol. 94, pp. 263118-3, 2009.

[106]   N. Yamada, T. Ijiro, E. Okamoto, K. Hayashi, and H. Masuda, "Characterization of antireflection moth-eye film on crystalline silicon photovoltaic module," *Opt. Express,* vol. 19, pp. A118-A125, 2011.

[107]   A. S. Chadha, E. D. Cline, M. Tao, and W. Zhou, "Large area imprinted surface textures for omnidirectional conformal AR coatings on flexible amorphous silicon solar cells," in *Photovoltaic Specialists Conference (PVSC), 2012 38th IEEE*, 2012, pp. 000327-000330.

[108]   J. Dobrowolski, Y. Guo, T. Tiwald, P. Ma, and D. Poitras, "Toward perfect antireflection coatings. 3. Experimental results obtained with the use of Reststrahlen materials," *Applied optics,* vol. 45, pp. 1555-1562, 2006.

[109]   J. Dobrowolski, D. Poitras, P. Ma, H. Vakil, and M. Acree, "Toward perfect antireflection coatings: numerical investigation," *Applied optics,* vol. 41, pp. 3075-3083, 2002.

[110]   D. Poitras and J. Dobrowolski, "Toward perfect antireflection coatings. 2. Theory," *Applied optics,* vol. 43, pp. 1286-1295, 2004.

[111]   B. G. Bovard, "Rugate filter theory: an overview," *Appl. Opt.,* vol. 32, pp. 5427-5442, 1993.

[112]   D. Poitras, S. Larouche, and L. Martinu, "Design and Plasma Deposition of Dispersion-Corrected Multiband Rugate Filters," *Appl. Opt.,* vol. 41, pp. 5249-5255, 2002.

[113]   P. B. Clapham and M. C. Hutley, "Reduction of Lens Reflexion by the Moth Eye Principle," *Nature,* vol. 244, pp. 281-282, 1973.

[114]   Y. F. Huang, S. Chattopadhyay, Y. J. Jen, C. Y. Peng, T. A. Liu, Y. K. Hsu, C. L. Pan, H. C. Lo, C. H. Hsu, and Y. H. Chang, "Improved broadband and quasi-omnidirectional anti-reflection properties with biomimetic silicon nanostructures," *Nature nanotechnology,* vol. 2, pp. 770-774, 2007.

[115]   J. Zhao, A. Wang, P. Campbell, and M. A. Green, "22.7% efficient silicon photovoltaic modules with textured front surface," *Electron Devices, IEEE Transactions on,* vol. 46, pp. 1495-1497, 1999.

[116]   W. Groh and A. Zimmermann, "What is the lowest refractive index of an organic polymer?," *Macromolecules,* vol. 24, pp. 6660-6663, 1991.

[117]   R. Pate, K. R. Lantz, and A. D. Stiff-Roberts, "Tabletop Resonant Infrared Matrix-Assisted Pulsed Laser Evaporation of Light-Emitting Organic Thin Films," *Selected Topics in Quantum Electronics, IEEE Journal of,* vol. 14, pp. 1022-1030, 2008.

[118]   R. Pate and A. D. Stiff-Roberts, "The impact of laser-target absorption depth on the surface and internal morphology of matrix-assisted pulsed laser evaporated conjugated polymer thin films," *Chemical Physics Letters,* vol. 477, pp. 406-410, 2009.

[119]   K. Johnson, "Coupled scalar wave diffraction theory," *Applied physics,* vol. 24, pp. 249-260, 1981.

[120]   D. Poitras, "Admittance Diagrams of Accidental and Premeditated Optical Inhomogeneities in Coatings," *Appl. Opt.,* vol. 41, pp. 4671-4679, 2002.

[121]   D. Poitras and J. A. Dobrowolski, "Toward Perfect Antireflection Coatings. 2. Theory," *Appl. Opt.,* vol. 43, pp. 1286-1295, 2004.

[122]   M. Khardani, M. Bouaïcha, and B. Bessaïs, "Bruggeman effective medium approach for modelling optical properties of porous silicon: comparison with experiment," *physica status solidi (c),* vol. 4, pp. 1986-1990, 2007.

[123]   G. B. Smith, "The scope of effective medium theory for fine metal particle solar absorbers," *Applied Physics Letters,* vol. 35, pp. 668-670, 1979.

[124]   K. L. Saenger, "On the origin of spatial nonuniformities in the composition of pulsed-laser-deposited films," *Journal of Applied Physics,* vol. 70, pp. 5629-5635, 1991.

[125]   C. F. R. Mateus, M. C. Y. Huang, L. Chen, C. J. Chang-Hasnain, and Y. Suzuki, "Broadband mirror (1.12-1.62 µm) using single-layer sub-wavelength grating," *IEEE Photon. Technol. Lett,* vol. 16, pp. 1676-1678, 2004.

[126]   S. Boutami, B. Bakir, P. Regreny, J. Leclercq, and P. Viktorovitch, "Compact 1.55 µm room-temperature optically pumped VCSEL using photonic crystal mirror," *Electronics Letters,* vol. 43, p. 282, 2007.

[127]   M. C. Huang, Y. Zhou, and C. J. Chang-Hasnain, "A surface-emitting laser incorporating a high-index-contrast subwavelength grating," *Nature Photonics,* vol. 1, pp. 119-122, 2007.

[128]   Y. Ding and R. Magnusson, "Resonant leaky-mode spectral-band engineering and device applications," *Optics Express,* vol. 12, pp. 5661-5674, 2004.

[129]   R. Magnusson and M. Shokooh-Saremi, "Physical basis for wideband resonant reflectors," *Optics Express,* vol. 16, pp. 3456-3462, 2008.

[130]   V. Lousse, W. Suh, O. Kilic, S. Kim, O. Solgaard, and S. Fan, "Angular and polarization properties of a photonic crystal slab mirror," *Optics Express,* vol. 12, pp. 1575-1582, 2004.

[131]   S. Boutami, B. B. Bakir, H. Hattori, X. Letartre, J. L. Leclercq, P. Rojo-Romeo, M. Garrigues, C. Seassal, and P. Viktorovitch, "Broadband and compact 2-D photonic crystal reflectors with controllable polarization dependence," *Photonics Technology Letters, IEEE,* vol. 18, pp. 835-837, 2006.

[132]   C. Sciancalepore, B. B. Bakir, X. Letartre, J. Harduin, N. Olivier, C. Seassal, J. Fedeli, and P. Viktorovitch, "CMOS-compatible ultra-compact 1.55- um emitting VCSELs using double photonic crystal mirrors," *IEEE Photonics Technology Letters,* vol. 24, pp. 455-457, 2012.

[133]   H. Yang, S. Chuwongin, Z. Qiang, L. Chen, H. Pang, Z. Ma, and W. Zhou, "Resonance control of membrane reflectors with effective index engineering," *Applied Physics Letters,* vol. 95, p. 023110, 2009.

[134]   H. Yang, D. Zhao, J. Seo, S. Kim, J. Rogers, Z. Ma, and W. Zhou, "Broadband Membrane Reflectors on Glass," *IEEE Photonics Technology Letters,* vol. 24, pp. 476-8, 2012.

[135]   H. Yang, D. Zhao, S. Chuwongin, J. H. Seo, W. Yang, Y. Shuai, J. Berggren, M. Hammar, Z. Ma, and W. Zhou, "Transfer-printed stacked nanomembrane lasers on silicon," *Nature Photonics,* vol. 6, pp. 617-622, 2012.

[136]   D. Zhao, H. Yang, S. Chuwongin, J. H. Seo, Z. Ma, and W. Zhou, "Design of photonic crystal membrane reflector based VCSELs," *IEEE Photonics Journal,* vol. 4, pp. 2169-75, 2012.

[137]   C. J. Chang-Hasnain, "High-contrast gratings as a new platform for integrated optoelectronics," *Semiconductor Science and Technology,* vol. 26, p. 014043, 2011.

[138]   H. Wu, W. Mo, J. Hou, D. Gao, R. Hao, H. Jiang, R. Guo, W. Wu, and Z. Zhou, "A high performance polarization independent reflector based on a multilayered configuration grating structure," *Journal of Optics,* vol. 12, p. 045703, 2010.

[139]   M. Shokooh-Saremi and R. Magnusson, "Leaky-mode resonant reflectors with extreme bandwidths," *Opt. Lett.,* vol. 35, pp. 1121-1123, 2010.

[140]   M. Kumar, C. Chase, V. Karagodsky, T. Sakaguchi, F. Koyama, and C. J. Chang-Hasnain, "Low Birefringence and 2-D Optical Confinement of Hollow Waveguide With Distributed Bragg Reflector and High-Index-Contrast Grating," *Photonics Journal, IEEE,* vol. 1, pp. 135-143, 2009.

[141]   R. Magnusson and M. Shokooh-Saremi, "Physical basis for wideband resonant reflectors," *Opt. Express,* vol. 16, pp. 3456-3462, 2008.

[142]   Z. Qiang, H. Yang, L. Chen, H. Pang, Z. Ma, and W. Zhou, "Fano filters based on transferred silicon nanomembranes on plastic substrates," *Applied Physics Letters,* vol. 93, pp. 061106-061106-3, 2008.

[143]   K. Sakoda, *Optical Properties of Photonic Crystals*: Springer, 2005.

[144]   I. Avrutsky, A. Svakhin, and V. Sychugov, "Interference phenomena in waveguides with two corrugated boundaries," *Journal of Modern Optics,* vol. 36, pp. 1303-1320, 1989.

Biographical Information

Arvinder Singh Chadha was born on January 10, 1985 in the city of Mumbai, India. He received the Bachelor of Engineering degree with a focus in VLSI in 2006 from University of Mumbai, India. In December 2008, he was received the Masters of Science at University of Colorado at Boulder with a focus in Nanostructures and Devices. During his Master's program he was involved in research related to photonic crystals and metamaterials.

Arvinder joined Professor Weidong Zhou's NanoPhotonics group in the Electrical Engineering Department at University of Texas at Arlington in Fall 2009 as a PhD candidate. He worked on research projects related to optical interconnects for integrated silicon photonics, near perfect absorption for efficiency enhanced photodetectors and solar cells and near perfect reflectors and antireflection coatings. He is also a member of IEEE and Eta Kappa Nu honor society.

Arvinder's research interests include integrated photonics and optoelectronics devices. He plans to pursue a career in process and (or) product development of novel integrated electronic and photonic devices.